Central North Atlantic (IODP Site U1313) paleoceanography based on a high-resolution dinoflagellate cyst record across the Early–Middle Pleistocene boundary (Marine Isotope Stages 20–18, ~810 –741 ka)

Walid Mohammed Abomriga

Department of Earth Sciences

A thesis submitted in partial fulfillment of the degree of

M.Sc. in Earth Sciences

Faculty of Mathematics and Science, Brock University

St. Catharines, Ontario, Canada

Abstract

A dinoflagellate cyst (dinocyst) study of 102 samples from Integrated Ocean Drilling Program Site U1313 in the central North Atlantic Ocean represents the most detailed dinocyst record yet available for Marine Isotope Stage (MIS) 19, which spans the Lower–Middle Pleistocene boundary. A published ultra-high-resolution $\delta^{18}O$ record constrains the study. The following paleoenvironmental indicators were among those used: *Operculodinium centrocarpum* sensu Wall & Dale (North Atlantic Current [NAC]), *Nematosphaeropsis labyrinthus* (sub-polar water masses), total *Impagidinium* spp. (subtropical gyre), and total protoperidiniacean cysts and total cyst concentrations (productivity indicators). Cooling just prior to Termination IX suggests a Younger-Dryas type event. An early arrival of the North Atlantic Current at ~797 ka and then warm subtropical gyre waters at 793.58 ka, presage the arrival of oligotrophic waters at 790.5 ka. The onset of peak interglacial conditions at 790.5 ka is delayed relative to the benthic $\delta^{18}O$ signal, which has a midpoint age for Termination IX at ~793 ka, and presumably reflects the persistence of ice sheets to the north. Peak interglacial conditions terminated at 784 ka with a duration of ~6500 years. This is shorter than the 10.5–12.5 kyr extent of full interglacial conditions recorded elsewhere and based on different criteria. Dinocyst transfer functions give August sea-surface temperatures of ~20°C for peak interglacial conditions, a few degrees cooler than at present. Subpolar water masses occupied Site U1313 in late MIS 19, but at 750.89 ka (early MIS 18) a return of the North Atlantic Current was followed by further warming, with an August sea-surface temperature of 20 °C for the highest sample at 741.41 ka.

ACKNOWLEDGMENTS

I am grateful to my supervisor Prof. Martin J. Head for his guidance throughout the project and for his support in sharing his treasured knowledge. My appreciation also goes to Dr. Patrizia Ferretti who provided us with the samples and whose raw data and information on foraminifera and stable isotopes were indispensable. Also I would like to thank Prof. Uwe Brand and Prof. Francine McCarthy for their assistance in reviewing this thesis, and Prof. Elisabeth Levac for her thoughtful comments on the submitted version.

Last but not least, I deeply thank and dedicate this work to my parents and siblings for their love and support from afar, and to all my friends.

TABLE OF CONTENTS

Abstract i

Acknowledgements.....ii

Table of Contents..... iii

List of Tables.....vi

List of Figures vii

List of Plates.....ix

List of Abbreviations…….....x

Chapter 1 – Introduction……..……...1

Chapter 2 – Study Area – Site U1313……..…….4

2.1. Introduction…….4

2.2. Lithostratigraphy……5

2.3. Modern oceanographic setting ……6

2.4. Paleoceanographic setting……..8

2.5. MIS 19…….…10

Chapter 3 – Materials and methods……..……..20

3.1. Composite Section……..…….20

3.2. Age model……..……...21

3.3. Palynological processing……..……23

3.4. Statistical analysis…….……..……30

Chapter 4 – Results……40

4.1 Dinoflagellate cyst concentrations…….40

4.2 The Dinoflagellate cyst assemblages at IODP Site U1313……..…42

4.3 Constrained Cluster Analysis……..……..……44

4.4 Canonical Correspondence Analysis (CCA) ……..……48

Chapter 5 – interpretation……..…..50

5.1. Modern Analogue Technique…….……..50

5.2 Dinoflagellate cyst assemblages at IODP Site U1313 and their ecological distribution……57

5.2.1 North Atlantic Current indicator…….……..…...59

5.2.2 Open Marine Species……..…….……..…….60

5.2.3 Species associated with cooler waters……...……63

5.2.4 Protoperidiniacean species…….64

Chapter 6 – Discussion……68

6.1 Comparison of palynological data with high-resolution oxygen isotope, nannofossil, and alkenone SST records of MIS 19…….……68

1. Assemblage biozone 1……..…...73

2. Assemblage biozone 2……..……..……73

3. Assemblage biozone 3……..……..……74

4. Assemblage biozone 4……..……..……75

5. Assemblage biozone 5……..……..……78

6. Assemblage biozone 6……..……..……81

7. Assemblage biozone 7……..……..……82

8. Assemblage biozone 8……..……..……82

Chapter 7– Summary and Conclusions……..……...85

Chapter 7– References……..……..……91

APPENDIX 1: Plates……..…..…..……100

APPENDIX 2: Full counts of the dinoflagellate cysts, acritarchs and reworked palynomorphs……..110

LIST OF TABLES

Table 1: Age (ka) of three discrete peaks during MIS 19 at three different sites……..15

Table 2: Detailed information on each sample used in the present study from Site U1313, including weight of each dried filtrate processed for palynology, duration of ultrasound treatment, and the number of tablets of *Lycopodium clavatum* spores added……..…….26

Table 3: The 19 samples for which a “no analogue” (N/A) result was returned before *P. stellatum* was excluded before final MAT reconstructions……..…33

Table 4: Dinocyst taxa used in the MAT analysis ((*) *Protoperidinium stellatum* was ultimately excluded; see text) including abbreviations of their names. Groupings used in the MAT analysis are shown. The abbreviations were also used in Canonical Correspondence Analysis (CCA)……..……..34

Table 5: The 16 samples that returned a “no analogue” (NA) result when running MAT on the U1313 dataset against the modern North Atlantic dataset (*n*=677)……..……..…….37

Table 6: List of dinoflagellate cyst taxa in the studied interval…….…..42

Table 7. Number of specimens of reworked dinoflagellate cysts and acritarchs with the samples in which they were found……..……..43

LIST OF FIGURES

Figure 1. Sites U1312 and U1313 at locations of Site 607 and 608……..…5

Figure 2. Summarized lithologic units and lithologies at Site U1313……..……7

Figure 3. Modern North Atlantic Ocean surface circulation illustrate North Atlantic Current (NAC) and the Gulf Stream positions…….……..9

Figure 4. Suggested position of the North Atlantic Current (NAC), and Arctic Front.....11

Figure 5. Foraminiferal oxygen isotopes for IODP Site U1313 ……..…….....14

Figure 6. Paleoclimate records of MIS 19 from different sites……..…17

Figure 7. Modern Surface water circulation of the North Atlantic.....19

Figure 8. Chronology for IODP Site U1313 based on foraminiferal oxygen isotopes……22

Figure 9. Location of surface sediment samples (red dots) in the *n*=1207…….....35

Figure 10. Location of surface sediment samples. Red circles and green squares represent the *n*=677…….38

Figure 11. Dinoflagellate cyst concentrations and planktonic $\delta^{18}O$ VPDB……..…...41

Figure 12. Constrained cluster analysis with assemblage biozones with dinoflagellate cyst concentrations and planktonic oxygen isotopes……..……..…….46

Figure 13. Canonical Correspondence Analysis (CCA) results…….49

Figure 14. Results (sea surface temperature) of validation tests performed with the Modern Analogue Technique on Site U1313 assemblages……..…..…52

Figure 15. Results (sea surface salinity) of validation tests performed with the Modern Analogue Technique on Site U1313 assemblages…….……..……53

Figure 16. Results (sea-ice cover) of validation tests performed with the Modern Analogue Technique on Site U1313 assemblages.....54

Figure 17. Paleoenvironmental reconstructions at Site U1313 using dinoflagellate cyst assemblages and based on the Modern Analog Technique……..…58

Figure 18. The relative abundance of open marine dinoflagellate cyst species at Site U1313……..…61

Figure 19. Relative abundance of dinoflagellate cyst species typically associated with cooler waters at Site U1313……....67

Figure 20. Dinoflagellate cyst assemblage biozones from the constrained cluster analysis with cyst concentrations and planktonic $\delta^{18}O$……..……..72

Figure 21. Palynological (A–G) along with oxygen isotope (K, L) and nannofossil (H–J) data for Site U1313……80

Figure 22. Comparison of palynological data with high-resolution oxygen isotope record……..84

LIST OF PLATES

Plate 1……....101

Plate 2……..…...103

Plate 3……...105

Plate 4……...107

Plate 5…..…109

LIST OF ABBREVIATIONS

AF: Arctic Front

AOM: Amorphous Organic Matter

AZ: Assemblage biozones

CCA: Canonical correspondence analysis

DSDP: Deep Sea Drilling Project

EMPT: Early–Middle Pleistocene Transition

EPICA: European Project for Ice Coring in Antarctica

GSSP: Global boundary-stratotype section and point

HCl: Hydrochloric acid

HF: Hydrofluoric acid

IODP: Integrated Ocean Drilling Program

MAT: Modern Analogue Technique

mbsf: meters below sea floor

MIS: marine isotope stage

NAC: North Atlantic Current

NADW: North Atlantic Deep Water

NATW: North Atlantic Transitional Waters

NCDC: National Climate Data Center

ODP: Ocean Drilling Program

PIC: Peak Interglacial Conditions

rmcd: revised meters composite depth

RO: reverse osmosis

SSS: sea-surface salinity

SST: sea-surface temperature

UQAM: Université du Québec à Montréal

VPDB: Vienna Pee Dee Belemnite

Chapter 1 – Introduction

In recent years, researchers have paid significant attention to Pleistocene interglacials because of their potential to provide analogues for climate stability in the Holocene (Emanuele et al. 2015) and for projected greenhouse-gas-induced global warming. Marine Isotope Stage (MIS) 19, an interglacial stage that occurred between ~790 and ~760 ka near the middle of the Early–Middle Pleistocene Transition (EMPT), represents an interesting case study (Head and Gibbard, 2015a). The orbital configurations of both the current interglacial and MIS 19 are similar and characterized by a minimum in the 400-kyr eccentricity cycle, accordingly subdued amplitude of precessional changes, and hence small amplitude variations in insolation (Berger et al., 1993; Ferretti et al., 2015).

During the EMPT, the Earth experienced a dramatic change in its climatic cyclicity. It shifted from dominantly 41-kyr cyclicity controlled by obliquity to a quasi-100-kyr periodicity thought to be associated with precession and/or obliquity (Hays et al., 1976; Imbrie et al., 1992; Head and Gibbard, 2005; Huybers, 2007). The EMPT has been known as the “mid-Pleistocene revolution” (Berger and Jansen, 1994) or more prosaically the “mid-Pleistocene transition” (Head and Gibbard 2015a).

The approximate midpoint of the EMPT has traditionally been used to place the Early–Middle Pleistocene Subseries boundary. This boundary has not yet been formally defined, although work is in progress to do so (Head and Gibbard, 2015b). The Matuyama–Brunhes paleomagnetic boundary that has been selected as the primary guide for the Early–Middle Pleistocene boundary (Head et al., 2008) falls within MIS 19.

Candidate sections for the Early–Middle Pleistocene boundary are being researched intensively, and one will be selected for the Global boundary Stratotype Section and Point (GSSP) (Head and Gibbard, 2015b). This is likely to happen in 2018. There is consequently an urgent need to understand the climatic structure of MIS 19 and its global expression, as well as the relationship of this internal variation to the position of the Matuyama–Brunhes boundary (Head and Gibbard, 2015b).

The North Atlantic area is characterized by a complex current system, which constitutes the northern part of the Atlantic Meridional Overturning Circulation. Two major currents of the North Atlantic are the warm and saline waters of the wind-driven North Atlantic Current (NAC) (Voelker et al., 2010) and the cold, dense thermohaline North Atlantic Deep Water (NADW) current (Ferretti et al., 2010). The strength and position of the NAC control the location of the Arctic Front and therefore produce considerable changes in sea-surface temperature (SST) and primary productivity over geological time (Naafs et al., 2010). Dinoflagellate cyst assemblages are useful indicators of past surface water masses, and can be studied to assess variability in the NAC. Dinoflagellate cysts have well-known distributions in the North Atlantic today (e.g., de Vernal et al., 2001), and they have been used successfully to reconstruct paleoceanographic conditions in the Quaternary (e.g., Matthiessen, 1995; de Vernal et al., 2005) and Neogene (e.g. De Schepper et al., 2013). In particular, dinoflagellate cysts have been used to infer changes in the position and strength of the NAC in the Pliocene and Pleistocene at suborbital time scales (e.g., De Schepper et al., 2009, 2013; Mantilla Duran, 2013; Hennissen et al., 2014, 2015, 2017).

In order to improve understanding of MIS 19 within the context of the EMPT, the present study addresses the paleoceanography and the response of the climate system to insolation across MIS 20–18 using a high-resolution dinoflagellate cyst record in combination with previously published benthic and planktonic oxygen isotope data from Integrated Ocean Drilling Program (IODP) Site U1313 in the east-central North Atlantic (Ferretti et al., 2015). The oxygen isotope record of Ferretti et al. (2015) represents the highest-resolved marine record available for MIS 19 in the North Atlantic, as does the present study of the dinoflagellate cysts.

Documenting the structure and duration of MIS 19 at high temporal resolution will allow comparison between the North Atlantic and other parts of the world for a time interval of importance to the geological time scale, elucidate the response of the NAC to insolation forcing though a prominent interglacial, and by comparison provide insights into the natural length and stability of the current interglacial, in the absence of anthropogenic forcing.

Chapter 2 – Study Area – Site U1313

2.1. Introduction

Integrated Ocean Drilling Program (IODP) Site U1313, drilled in 2005, is a reoccupation of Deep Sea Drilling Project (DSDP) Site 607, located on the Mid-Atlantic Ridge at the base of its upper western flank in a water depth of 3426 m, ~386 km northwest of the Azores at 41°00’ N, 32°58’ W (Fig. 1) (Expedition 306 Scientists, 2006). Site U1313 presently occurs at the northern margin of the subtropical gyre (Fig. 3, 7) and is therefore sensitive to the position of the NAC. The surface waters at the site are influenced by the diffuse cold-core eddies of the NAC which mostly pass northwest of Site U1313 (Fratantoni, 2001, pl. 6). The ocean floor, at depth of 3426 m, is currently under the influence of NADW. Since the end of the Late Pliocene and the beginning of the Pleistocene, however, the site has been regularly influenced by high-latitude waters, as shown by low SSTs as reconstructed from alkenones and by the presence of ice-rafted debris (Naafs et al., 2011, 2013).

2.2. Lithostratigraphy

At Site U1313, a 308m succession of pelagic sediment extending continuously from Holocene into the Upper Miocene (Messinian) was recovered from four holes A, B, C, and D (Fig. 2). Fairly constant sedimentation rates of between 4.1 and 4.5 cm/ky are recorded throughout (Expedition 306 Scientists, 2006). These holes allowed construction of two linked stratigraphic sections, one complete section built from Holes U1313B and U1313C and a second nearly complete section from Holes U1313A and U1313D (Expedition 306 Scientists, 2006).

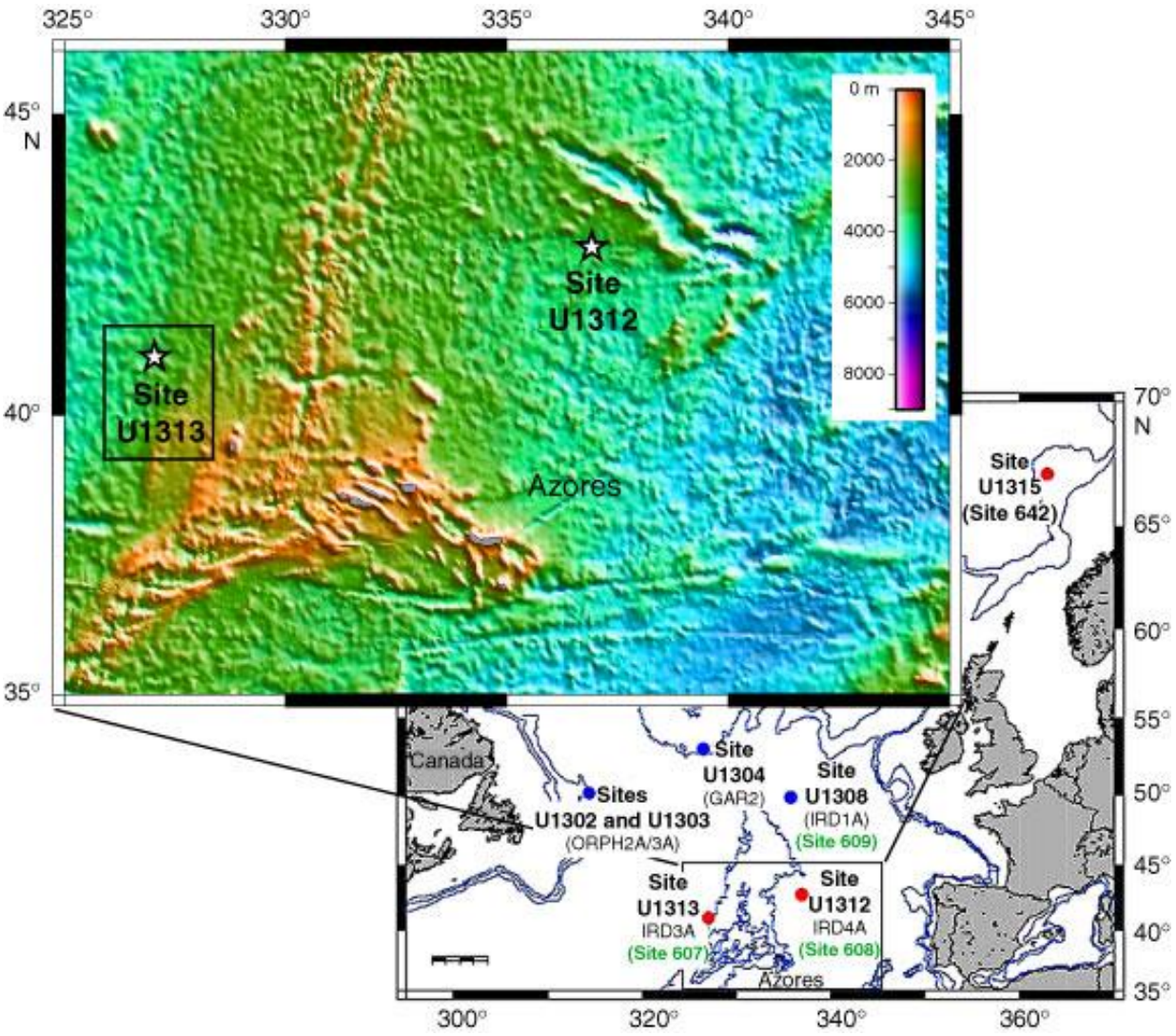

Figure 1: IODP Sites U1312 and U1313 drilled during Expedition 306 at the locations of DSDP Sites 607 and 608. Insert shows detailed bathymetry (in m) of the area with Site U1313 located at the base of the western flank of the Mid-Atlantic Ridge (Expedition 306 Scientists, 2006, fig.1).

The sediment recovered is mainly nannofossil ooze with varying amounts of foraminifers and clay- to silt-sized terrigenous material. Major lithologies range from silty clay nannofossil ooze to nannofossil ooze, with minor foraminifer nannofossil ooze, silty clay nannofossil ooze with diatoms, and nannofossil silty clay. Smear slides indicate that the noncalcareous sediment (consisting of biogenic silica, quartz, and clay) generally

comprises 5%–40% of the sedimentary sequence. Sediments recovered are generally undisturbed (Expedition 306 Scientists, 2006). The sediments analysed for dinoflagellate cysts (hereafter dinocysts) in the present study represents a splice of two cores covering a core length of 296 cm, from 32.18 meters below sea floor (mbsf) to 34.95 mbsf. This interval occurs within Core 4H in both Holes A and D and so is within lithological subunit 1A, which is characterized by around 15–30% clay to silty clay and the remainder mostly nannofossil ooze (Fig. 2).

2.3. Modern oceanographic setting

The surface waters of the North Atlantic Ocean today are influenced by a complex current system that starts with the Gulf Stream and flows north and northeast, branching into the North Atlantic Current (NAC) and the Azores Current. The NAC separates two major water masses: the subtropical gyre which is characterized by warm, saline oligotrophic waters and the subpolar gyre characterized by cold, low salinity and nutrient-rich waters (Emanuele et al., 2015). The NAC therefore creates a transitional area between these two regimes known as North Atlantic Transitional Waters (NATW) bordered by the subtropical gyre in the south and the North Atlantic Current (NAC) in the north. The subpolar front forms the northern border of the NAC (Emanuele et al., 2015).

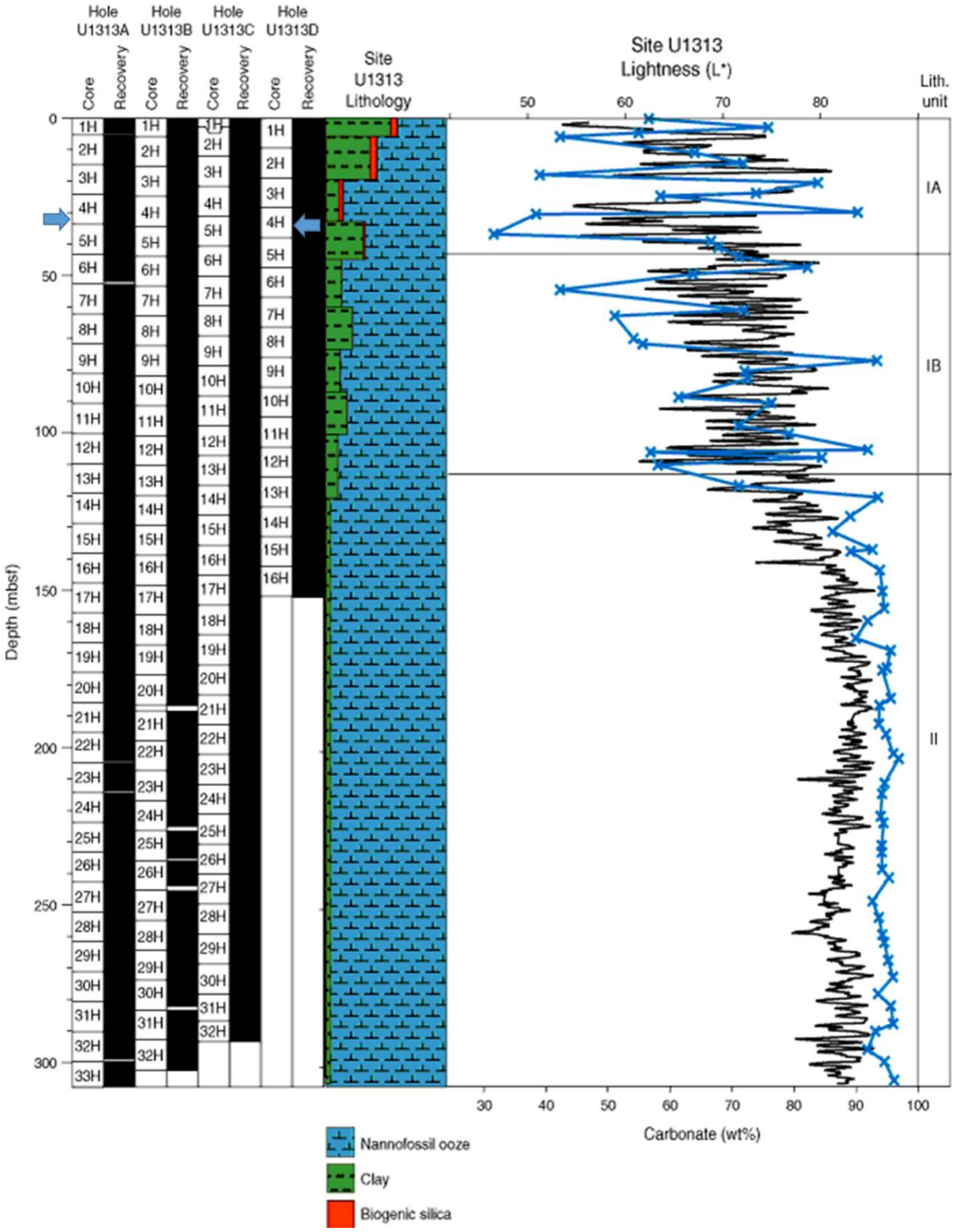

Figure 2: Schematic summary of core recovery at Site U1313. Sediment lightness values were determined from color reflectance data (black) and carbonate values (blue). Blue arrows indicate the positions of sampled intervals in Core 4H, Sections 7 and 6 of Hole U1313A, and Core 4H, Sections 5 and 6 Hole U1313D. (Expedition 306 Scientists, 2006, fig. 7).

IODP Site U1313 is located today at the northern margin of the subtropical gyre very close to the NAC. The surface waters over this site are in fact derived from the NAC. This site is also in the path of the cold, dense North Atlantic Deep Water (NADW) western boundary current (Ferretti et al., 2010). The Arctic Front (AF) is controlled by the location and the strength of NAC which can lead to changes in climate proxies including sea-surface temperature (SST) and primary productivity (Naafs et al., 2010). The modern North Atlantic Transitional Waters (NATW) zone at IODP Site U1313 is characterized by SSTs ranging from 15.2 °C in winter and 22.6 °C in summer with a mean annual SST of 18.3°C. August SST is 22.7°C. The sea-surface salinity (SSS) has a very narrow range between 35.9 psu in winter and 36.2 psu in autumn, with a mean annual SSS of 36.02 psu (Zweng et al., 2013).

2.4. Paleoceanographic setting

IODP Site U1313 is located just southeast of the warm and saline surface waters of the NAC, which drives the modern surface hydrography in the area (Voelker et al., 2010), and is influenced also by the cold NADW current (Ferretti et al., 2010), as noted above. The site was affected by these two oceanic currents also during the Middle Pleistocene (Wright and Flower, 2002; Expedition 306 Scientists, 2006; Naafs et al., 2011).

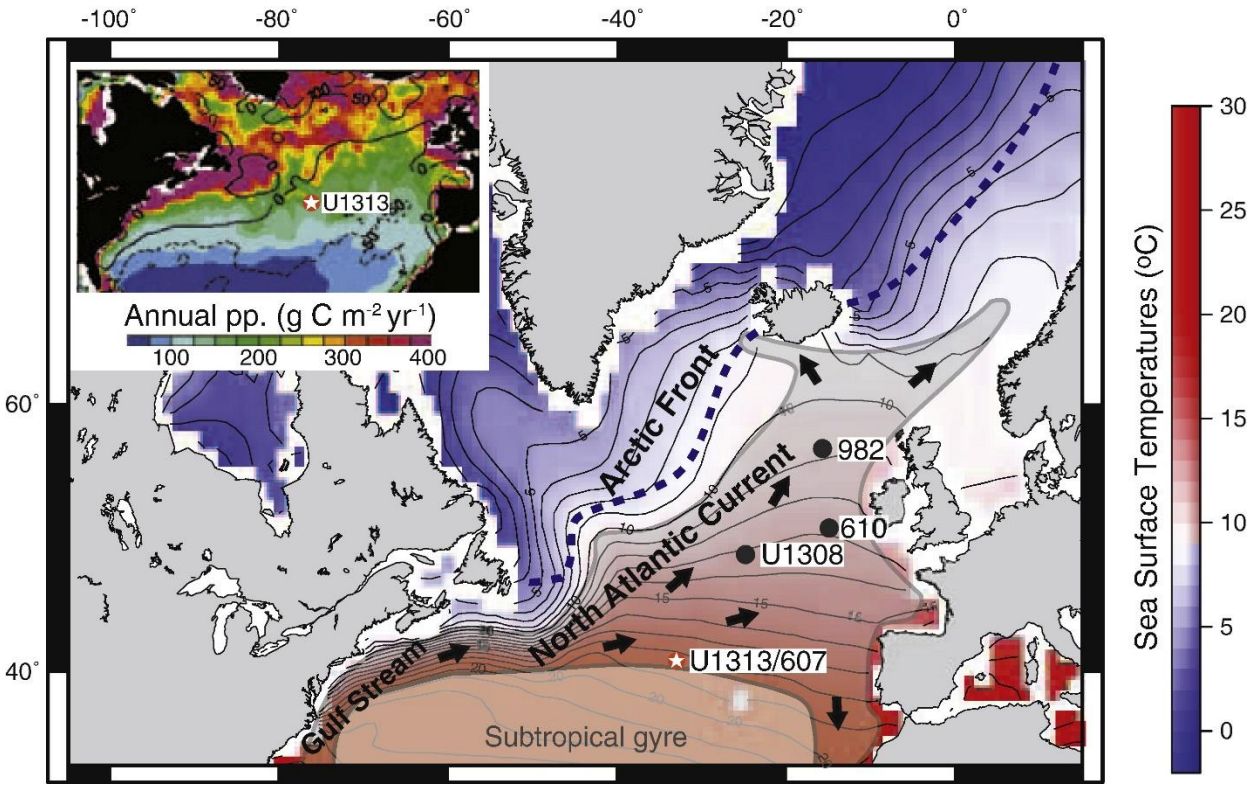

Figure 3. Modern North Atlantic Ocean surface circulation, illustrating the mean current positions of the North Atlantic Current (NAC) and Gulf Stream. Dashed line indicates the mean Arctic Front (AF) position (Pflaumann et al., 2003; Swift, 1986). Isotherms of mean annual sea surface temperatures (SSTs) (Locarnini et al., 2006) are shown and annual primary productivity (pp, grams of carbon fixed per m^2/y) is illustrated in the insert. The star indicates the location of IODP Site U1313 (Naafs et al., 2010 fig.1).

The investigated time interval, MIS 20–18 (~810–741.4 ka) at Site U1313, has been divided into three episodes based on a high-resolution calcareous nannofossil record studied by Emanuele et al. (2015). The first episode, the later part of glacial MIS 20 to the MIS 20/19 boundary at Termination IX (~800 to 790 ka), is marked by the presence of cold surface waters deriving from ice melting at higher latitudes, as recorded by *Coccolithus pelagicus pelagicus*. This episode is marked by the highest paleoceanographic instability recorded throughout the interval examined by Emanuele et

al. (2015). At around Termination IX, between ~793 and ~792 ka, the northward-moving NAC reached Site U1313 (Fig. 4). The second episode is represented by MIS 19c and is characterized by warm interglacial conditions and a reduction in palaeoceanographic variability. This marks the establishment of warmer, nutrient-poor, surface waters of the North Atlantic Transitional Water, reflecting an intensification of the subtropical gyre influence on Site U1313 (Fig. 4c). The third episode marks the transition from MIS 19 to MIS 18, and is characterized by an overall southward shift of the palaeoceanographic system including the subpolar front, and is indicated at Site U1313 by an increase in the cold subspecies *C. pelagicus pelagicus*. It marks a return to instability. The NAC moved south of Site U1313 at this time, and subpolar waters had occupied the site by 767 ka.

2.5. MIS 19

During the Early–Middle Pleistocene transition, of which ~773 ka (MIS 19) represents an approximate mid-point (Fig. 5), climate cycles changed progressively from ~41 ka to ~100 ka periodicity. MIS 19 has astronomically derived boundary ages of 790 and 761 ka according to the LR04 global benthic $\delta^{18}O$ stack of Lisiecki and Raymo (2005; see http://www.lorraine-lisiecki.com/LR04_MISboundaries.txt). The inception of MIS 19 is taken at the midpoint of Termination IX. The MIS 19/18 boundary is drawn at the midpoint between the peak of lightest values of MIS 19 and the first of two troughs of heaviest values that characterize MIS 18. The MIS 19/18 boundary is therefore difficult to recognize consistently, and its positioning will vary depending on the nature of the records used. For Site U1313, Ferretti et al. (2015, see Chapter 3) established boundary ages of 761 and 790 ka for MIS 19. The age model of Ferretti et al. (2015) is used throughout this thesis.

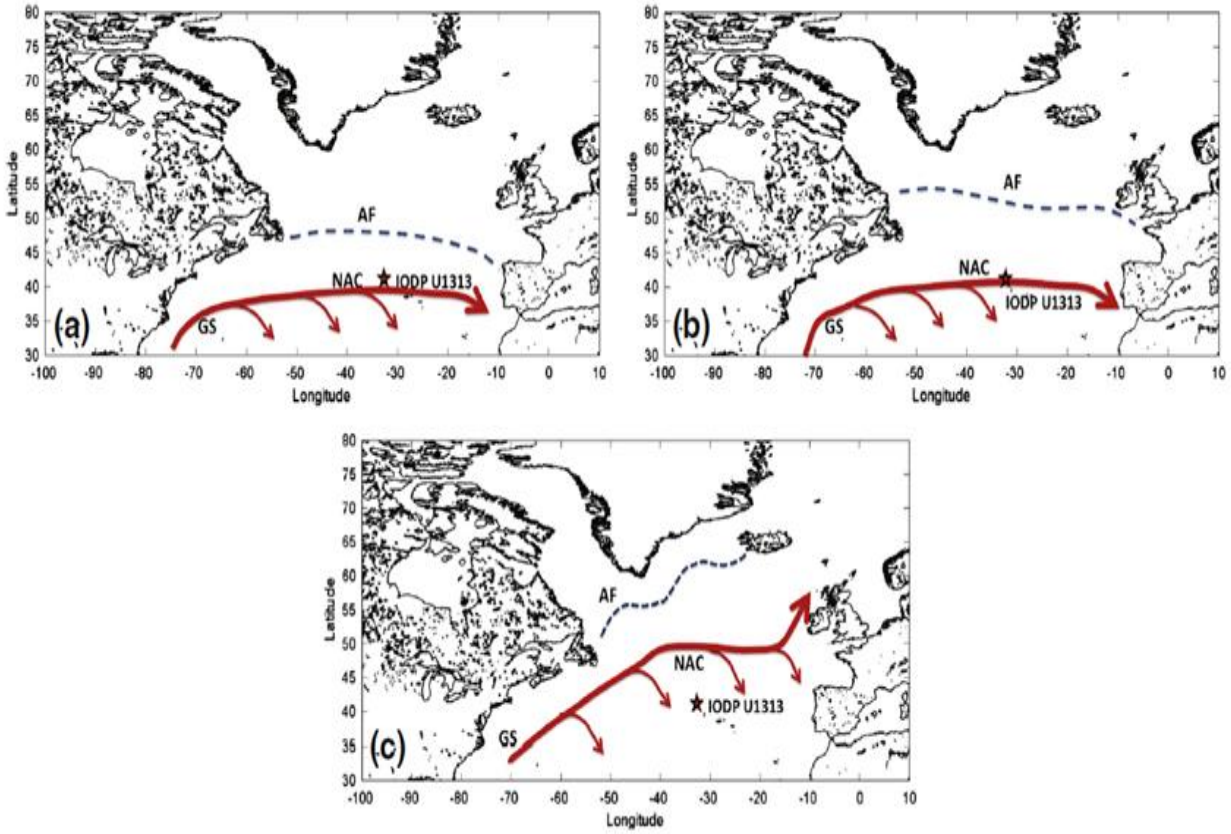

Figure 4. Schematic representation of the suggested position of the North Atlantic Current (NAC), and Arctic Front (AF) during a) MIS 20, b) Termination IX, and c) MIS 19c (after Emanuele et al., 2015, fig. 7).

Using geochemical proxies and the sedimentary response to environmental change, it has been possible to subdivide the 28 marine oxygen isotope stages of the last 1.0 million years into discrete and theoretically global substages (Railsback et al., 2015). Marine isotope stages before this time are too short to warrant subdivision (Railsback et al., 2015). MIS 19 has been subdivided into three substages, MIS 19a, b, and c, with MIS 19c being the oldest and including the lightest $\delta^{18}O$ values (Railsback et al., 2015; Ferretti et al., 2015). This substage terminology is used in the present study. During MIS 19, a

high frequency signal is documented in the benthic and planktonic foraminiferal $\delta^{18}O$ isotopes, although its amplitude is strongly reduced in MIS 19c, suggesting an interval of relative stability.

During the MIS 19–18 transition, fluctuations in amplitude increase. Early in MIS 19, ice-rafted debris decreased rapidly in North Atlantic deep-sea cores as deglaciation progressed (Wright and Flower, 2002). Nonetheless, the ultra-high-resolution benthic and planktonic $\delta^{18}O$ record of Ferretti et al. (2015) for Site U1313 shows an early rise to lighter values both in the benthic and planktonic at 800 ka (MIS 20) followed by a drop and then final rise representing Termination IX and the start of MIS 19 at 790 ka. This incipient warming and then return to cold conditions just prior to the final deglaciation is reminiscent of the Younger Dryas cooling event that interrupted the last deglaciation in the Late Pleistocene. As noted by Head and Gibbard (2015), this Younger Dryas-like cooling event just prior to MIS 19 has been recognized from various parts of the world including northern North Atlantic IODP Site U1308 (Hodell et al., 2008, as MIS 20b), Montalbano Jonico in Basilicata, southern Italy (Simon et al., 2017), Lake Baikal in Russia (Prokopenko et al., 2006), and southwest Pacific ODP Site 1123 (Elderfield et al., 2012).

The rise to lightest isotopic values and warmest temperatures occurs at slightly different times in different records, and with different proxies. The LR04 benthic $\delta^{18}O$ stack (Lisiecki and Raymo, 2005) shows a late peak to lightest values at 780 ka (Head and Gibbard, 2015) whereas an earlier benthic $\delta^{18}O$ peak (at 787 ka) is recorded at Site U1313 (Fig. 5; Ferretti et al., 2015). The δD (a paleotemperature proxy), CO^2, and CH^4 records for the EPICA Dome C Antarctic ice core all illustrate an early peak warming at 787 ka (Tzedakis et al., 2012).

Regarding the structure of MIS 19, three discrete peaks in atmospheric CH_4, δD values and CO_2 have been recorded in the EPICA Dome C ice core beginning at the onset of the MIS 19c–b boundary. These peaks match but significantly are out of phase with peaks in ice-rafted debris and planktonic $\delta^{18}O$ recorded at ODP Site 983 on the Gardar Drift in the North Atlantic. Moreover, the benthic $\delta^{18}O$ signal leads the planktonic $\delta^{18}O$ signal at Site 983. A bipolar seesaw mechanism between the northern and southern hemispheres, caused by ice sheet growth and subsequent instability, seems to explain these features (Fig. 6; Tzedakis et al., 2012). This variability began at around 774.5–772.5 ka in both the EPICA Dome C and ODP Site 983 records (Fig. 6), which coincides with the timing of the Matuyama–Brunhes boundary (Head and Gibbard, 2015). Although the Matuyama–Brunhes boundary was recorded at Site U1313 during shipboard investigations (Expedition 306 Scientists, 2006), its position dated at 787±4 ka (Ferretti et al., 2015) is anomalously old (Head and Gibbard, 2015a) and apparently has not been confirmed by follow-up shore-based studies. However, the three peaks identified by Tzedakis et al. (2012) are possibly identified in the planktonic record at U1313 (Ferretti et al., 2015).

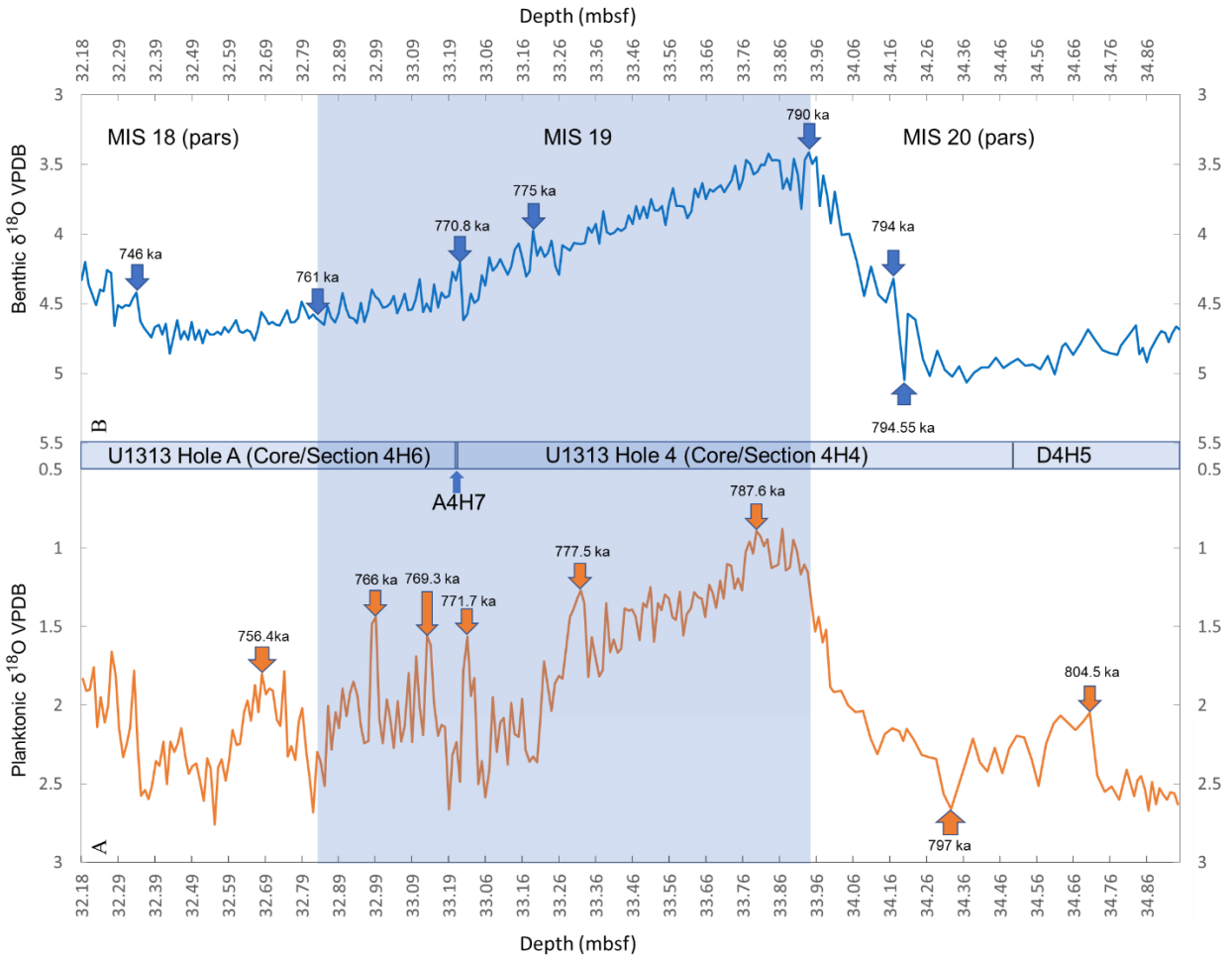

Figure 5: Foraminiferal oxygen isotopes for IODP Site U1313 plotted against depth (mbsf) for Site U1313. A. (orange line) planktonic $\delta^{18}O$ record; B (blue line) benthic $\delta^{18}O$ record. Data supplied by P. Ferretti (upon which Ferretti et al., 2015 is based). Arrows (orange and blue) indicate ages (in ka) of specific peaks and troughs based on the age model of Ferretti et al. (2015, fig. 3; see Chapter 3). The interval 34.95–33.00 mbsf is from U1313 Hole D (Core/Section 4H-5 and 4H-4), and 33.22–32.18 mbsf is from U1313 Hole A (Core/Section 4H-7 and 4H-6). The upper and lower boundaries of MIS 19 are based on the age model of LR04. Mbsf = meters below sea floor.

Planktonic $\delta^{18}O$ records at Site U1313 show three peaks (Table 1, Fig. 6), the first at 771.7 ka (Ferretti et al., 2015) which may correspond to the peak at 771 ka in atmospheric CH_4 concentration in EPICA Dome C and 772.1 ka in planktonic $\delta^{18}O$ signal at Site 983 (Tzedakis et al., 2012). The second peak starts at 769.3 ka (Ferretti et al.,

2015) and matches the peak in atmospheric CH_4 concentration in EPICA Dome C at 764 ka and at 769.4 ka in the planktonic $\delta^{18}O$ signal at Site 983 (Tzedakis et al., 2012). The third peak, at 766 ka, seems to correspond to the peak at 758 ka in atmospheric CH_4 concentration in EPICA Dome C and at 766 ka in the planktonic $\delta^{18}O$ signal at Site 983 (Tzedakis et al., 2012).

Table 1: Age (ka) of three discrete peaks during MIS 19 at three different sites. Site U1313 (Ferretti et al., 2015) and Site 983 (Tzedakis et al., 2012) are both based on planktonic $\delta^{18}O$ records, and the EPICA Dome C ice core (Tzedakis et al., 2012) is based on atmospheric CH_4.

Site	Age of peak 1	Age of peak 2	Age of peak 3
Site U1313 North Atlantic	771.7 ka	769.3 ka	766 ka
Site 983 North Atlantic	772.1 ka	769.4 ka	766 ka
EPICA Dome C (Antarctica)	771 ka	764 ka	758 ka

If these correlations are correct, it can be seen that for the first peak the planktonic $\delta^{18}O$ signal at Site 983 slightly leads planktonic $\delta^{18}O$ records at Site U1313, and that both North Atlantic sites 983 and U1313 were leading atmospheric CH_4 concentrations in the EPICA Dome C core. For the second peak the lag/ lead disappears between the two North Atlantic sites but the lag in atmospheric CH_4 at EPICA Dome C increases from 1 ka to 5 ka. For the last peak, planktonic $\delta^{18}O$ records in the North Atlantic sites are again synchronous and lead the atmospheric CH_4 concentration in EPICA Dome C by 8 ka. This seems to match expectations that both North Atlantic sites ODP 983 and IODP U1313 were controlled by synchronous environmental conditions, and that that the onset of these conditions was delayed at the Antarctic EPICA Dome C site. Full interglacial

conditions during MIS 19 are proposed to have ended near the summer insolation minimum at 777 ka, based on comparisons with the last glacial inception when sea-level started falling about 3 ky before the onset of major bipolar seesaw variability (Tzedakis et al., 2012). MIS 19 has been proposed as the closest analogue of the present interglacial with respect to its astronomical and paleoclimatic characteristics (Tzedakis et al., 2009, 2010, 2012). Although minor differences do exist in this regard (Emanuele et al., 2015), it may be noted that Emanuele et al. (2015) in their study of the nannofossils at Site U1313 found that during MIS 19c conditions were never significantly warmer than they are today. The low amplitude of the eccentricity cycle during both MIS 19 and MIS 1, through its modulation of the precessional cycle, results in a major drop in the summer insolation maximum (Tzedakis et al., 2012, fig. 1). The phasing between orbital forcing (obliquity and precession) appears to be analogous during MIS 19 and MIS 1. Although there is a more rapid increase in obliquity at the onset of MIS 1 than for MIS 19, there are smaller peak values for MIS 1 indicated from the LR04 global benthic $\delta^{18}O$ stack of Lisiecki and Raymo (2005) (Tzedakis, 2010, figs. 6 and 7; Head and Gibbard, 2015).

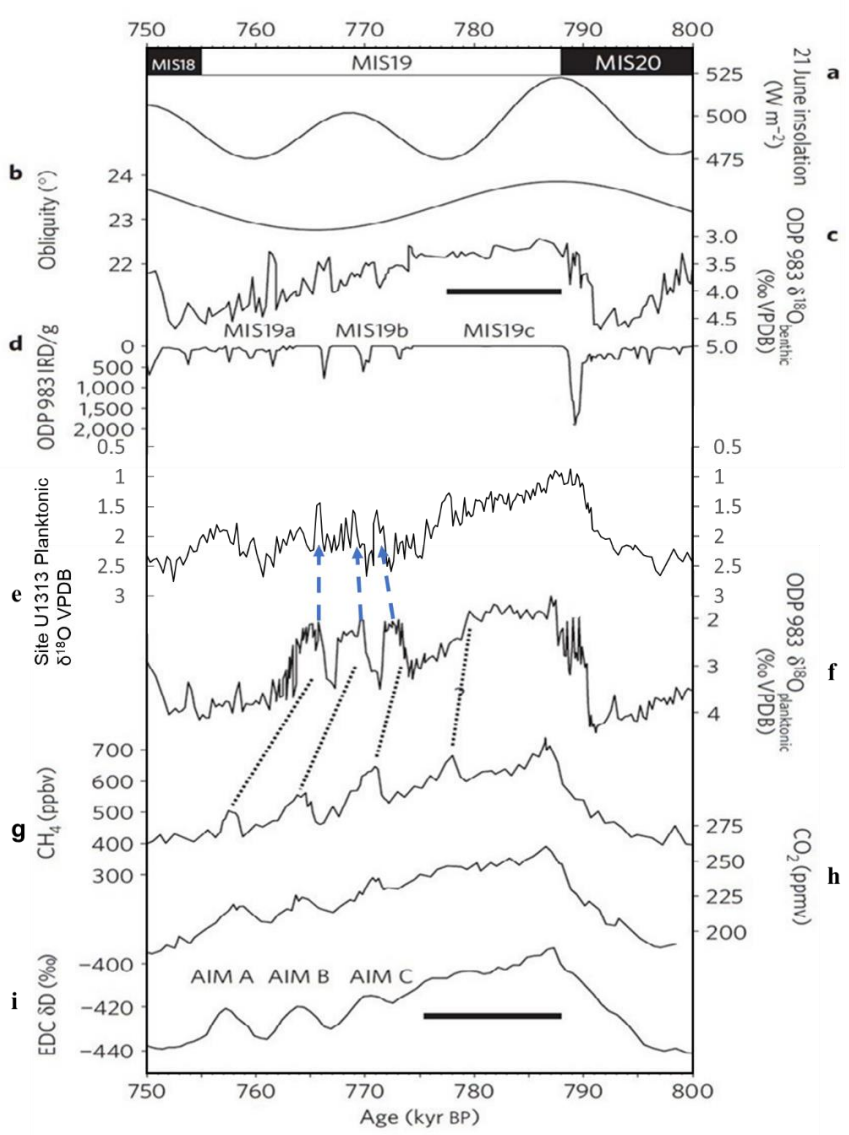

Figure 6: Paleoclimate records of MIS 19 from ODP Site 983 (Gardar Drift, North Atlantic) and EPICA Dome C (EDC) ice core (Antarctica)**; a**, 21 June insolation at 65˚N; **b** obliquity; **c**, ODP 983 $\delta^{18}O$ benthic record; **d**, ODP 983 ice-rafted detritus (IRD); **e**, IODP Site U1313 planktonic $\delta^{18}O$ record (data supplied by P. Ferretti, based on Ferretti et al., 2015); **f**, ODP 983 $\delta^{18}O$ planktonic record; **g**, atmospheric CH^4 concentration in the EPICA Dome C (EDC) ice core; **h**, atmospheric CO_2 concentration in the EDC ice core; **i**, δD composition of ice in the EDC ice core (AIM = Antarctic Isotope Maximum). Dotted lines represent correlation between ODP 983 and EDC indicating the three peaks where the ODP 983 $\delta^{18}O$ planktonic record is leading in all peaks. Blue dashed lines represent proposed correlation of peaks between Site U1313 and Site 983 (present study). Duration of full interglacial conditions is indicated by the horizontal bars. (Modified from Tzedakis et al., 2012, fig. 4).

At Site U1313, interglacial conditions started at ~791–790 ka, corresponding to the onset of MIS 19, with a rapid warming of sea surface temperatures as reconstructed from planktonic foraminiferal $\delta^{18}O$ (Ferretti et al., 2015) and nannofossil assemblages (Emanuele et al., 2015), these two proxies showing simultaneous warming. Full interglacial conditions are indeed considered to have extended from ~791–790 ka to 779 ka at Site U1313, representing an interval of ~11–12 ky, based on nannofossil (Emanuele et al., 2015) and organic geochemical (Ferretti et al., 2015) evidence. This duration does not seem to differ significantly from estimated durations from other sites. One such important site is Montalbano Jonico, a candidate GSSP section in southern Italy (Marino et al., 2015; Head and Gibbard, 2015b). At this site, full interglacial conditions during MIS 19 lasted for about 14–20 ky, the uncertainty resulting from the spacing between samples (Head and Gibbard, 2015a). From lacustrine deposits of the Sulmona Basin in central Italy, which are tightly constrained by an $^{40}Ar/^{39}Ar$ model, $CaCO_3$ percentages suggest that full interglacial conditions lasted 10.8 ± 3.7 ky during MIS 19c (Giaccio et al., 2015). The two Italian GSSP candidate sites at Valle di Manche and Montalbano Jonico are astrochronologically constrained, and both yield full interglacial durations of ~12.5 ky during MIS 19c (Tzedakis et al., 2012).

The phasing between the high-resolution records of planktonic and benthic foraminiferal $\delta^{18}O$ and benthic $\delta^{13}C$ at North Atlantic Site U1313 indicate slight but significant differences, with the benthic $\delta^{18}O$ record leading the planktonic $\delta^{18}O$ record by ~1080 years and benthic $\delta^{13}C$ by ~1300 years (Head and Gibbard, 2015a). The lag in the planktonic signal reflects cold surface waters that were affected by a late shift of the Arctic

Front towards the north due to the slow deglaciation of ice sheets in the northern hemisphere (Ferretti et al., 2015). Such lags generally happen when some elements of the climate system respond earlier or later than other elements to orbital forcing (Head and Gibbard, 2015a).

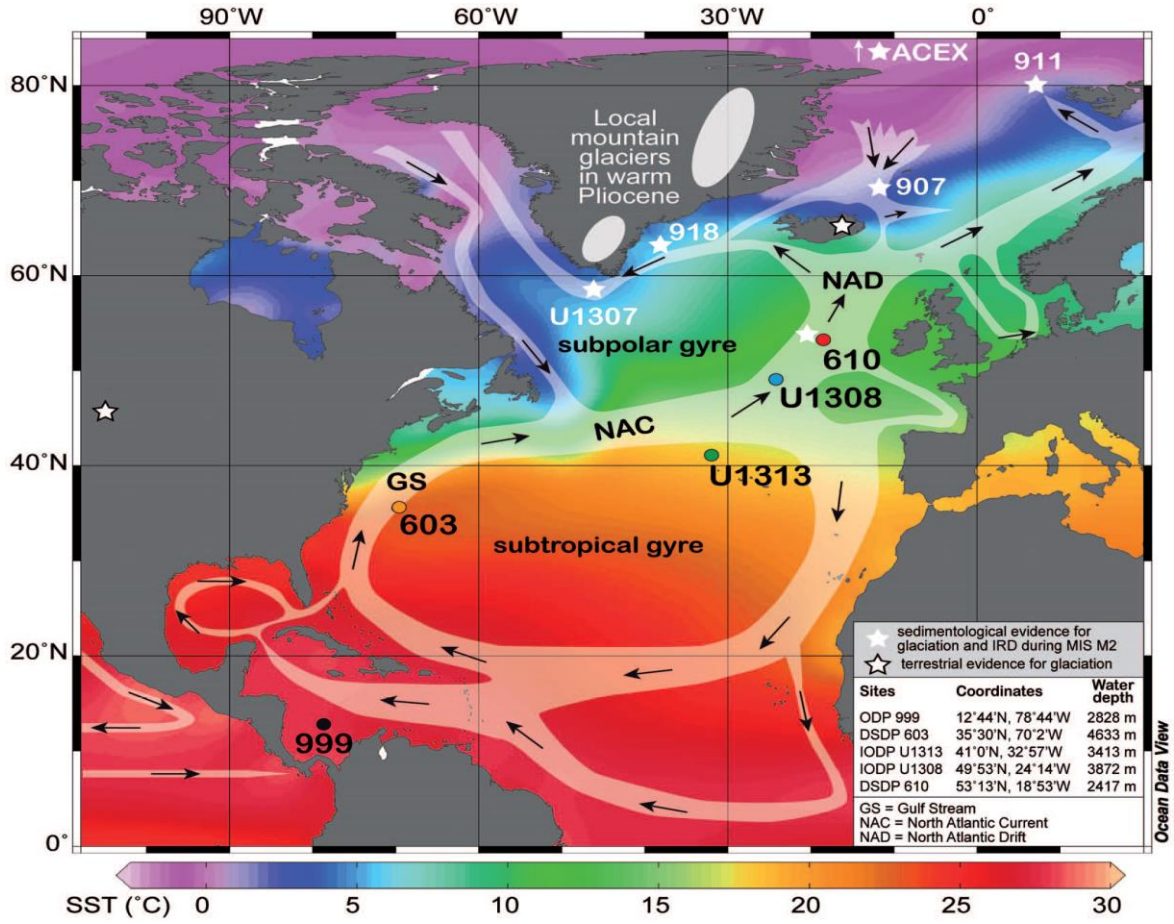

Figure 7: Modern surface water circulation of the North Atlantic and the location of Site U1313 located at the northern margin of the subtropical gyre (after De Schepper et al. 2013, fig. 2).

Chapter 3 – Materials and methods

For the present study, 102 samples from IODP Expedition 306, Site U1313 Holes A and D were processed for palynological analysis with the intention of assessing the dinocyst signal throughout MIS 19 and its transition to bounding glacials. Samples represent the dried 63-µm filtrate from a published study of the foraminiferal stable isotopes (Ferretti et al., 2015). Samples used in the present study are numbered sequentially from base to top, sample 1 representing 809.957 ka and sample 102 representing 741.414 ka on the time scale of Ferretti et al. (2015). The sample spacing for this stable isotope study is 1 cm for most of the analyzed interval, but samples used in the present study have an average separation of 3 cm, representing 672 years on average between samples. The stable isotope study, and the present research on the dinocysts, represent the most detailed investigation of MIS 19 yet undertaken for the marine realm.

3.1. Composite Section

In acquiring a deep-sea sediment record for paleoenvironmental analysis, it is routine practice to drill multiple holes at a particular site, each hole depth-offset relative to the others. Accordingly, any missing sediment between successive piston cores in one hole can be patched by splicing with an adjacent depth-offset core from an adjacent hole. The result of this splicing is a composite section for the site based on two or more closely spaced holes. This was done for Site U1313. The composite section for Site U1313 was sampled at a constant 1-cm spacing following the shipboard secondary splice, the samples used in the present study having a range of 39.35–35.94 m composite depth (mcd). To provide more accurate correlation points, the combined stratigraphic section

was refined postcruise using shipboard magnetostratigraphy, lightness, and magnetic susceptibility measurements. The interval sampled in the present study represents between 39.41 and 36.30 revised meters composite depth (rmcd) (Naafs et al., 2012), based on Holes D and A. Hole D samples are from Core 4, Sections 5 and 4; and Hole A samples are from Core 4, Sections 7 and 6. The sampling interval in Hole D represents 39.41–37.37 rmcd (34.95–33.02 mbsf) corresponding to 809.96–771.38–ka, which includes the MIS 20/19 transition and full interglacial conditions of MIS 19. The sampling interval in Hole A represents 37.34–36.30 rmcd (33.22–32.18 mbsf) corresponding to 770.80–741.41 ka, which includes the MIS 19/18 transition. Full details of the samples used in the present study are presented in Table 2.

3.2. Age model

Ferretti et al. (2015) attempted various strategies to develop a geological time scale based on the cyclicity observed at Site U1313, and the best technique they found was to develop an age model within the framework of the stacked global benthic $\delta^{18}O$ record of Lisiecki and Raymo (2005) (hereafter LR04). Initially, they developed a chronology derived by correlating the Site U1313 benthic $\delta^{18}O$ signal to LR04, because this had proved an effective and well-documented target for an earlier study of an interval lower in the sequence of U1313 (MIS 21; Ferretti et al., 2010). In order to obtain a sequence long enough for statistical analyses, the new results from MIS 19 were combined with the previously published foraminiferal stable isotope records for MIS 22–20 from this site (Ferretti et al., 2010). The approach was to identify in this sequence the trace of a particular component of the orbital forcing, and to then assess the presence of higher frequency orbital parameters. The initial LR04 chronology showed a concentration

of power at the precession band in all the isotope records reconstructed from Site U1313, and this component was strongest in the planktonic $\delta^{18}O$ record (Ferretti et al., 2015). The planktonic $\delta^{18}O$ record was therefore used to construct the age model in the Ferretti et al. (2015) study. The present study adopts the age model and MIS boundaries (761 and 790 ka) postulated by Ferretti et al. (2015).

Figure 8: Chronology for IODP Site U1313 based on foraminiferal oxygen isotopes; A. (orange line) planktonic $\delta^{18}O$ record; B (blue line) benthic $\delta^{18}O$ record. Data supplied by P. Ferretti using the age model of Ferretti et al. (2015). The MIS 20/19 and MIS 19/18 boundaries follow Ferretti et al. (2015).

3.3. Palynological processing

The procedure for palynological sample processing was modified from methods already used at Brock University to suit the requirements of deep-ocean sediment.

The sediment samples used were dried filtrates received from the Godwin Laboratory at the University of Cambridge, UK, with the cooperation of Dr. Patrizia Ferretii, where they had been saved from a previous study of the foraminiferal isotopes (Ferretii et al., 2015). The original sediment samples had been disaggregated in reverse osmosis (RO) water using an orbital shaker, and then washed through a 63 µm sieve in order to retain the sand size fraction including the foraminifera which were subsequently picked for isotopic analysis. The <63 µm filtrate, which contained dinoflagellate cysts, was allowed to settle overnight. It was subsequently dried and saved. This procedure was performed under the direction of Dr. Patrizia Ferretti who allowed the dried sediment to be used for the present study.

Palynological processing of the dried filtrate sample was conducted at Brock University. Each sample was weighed and then transferred to a plastic 400 ml beaker, and sealed with Parafilm to avoid airborne contamination prior to and during processing. Up to about 150 ml of cold HCl (diluted to 20% of conc.) was added to each beaker to dissolve carbonates. The HCl was added in small increments to avoid any possibility of bubbling over, given the carbonate-rich composition of the samples. After the reaction had stopped, each beaker was then swirled several times to suspend the sediment, and allowed to stand overnight to fully dissolve the carbonates. Following this, distilled water was added vigorously up to about 500 ml, and the beakers then allowed to stand for about 9 hours. Samples were then washed with distilled water several times until they reached

a pH of about 6 (i.e. the pH of distilled water which is slightly acidic from dissolved CO_2). During this washing procedure, the supernatant was siphoned off using a glass pipette connected by a hose to a Venturi pump attached to a water tap. After the samples had been neutralized and the supernatant removed, 48% conc. cold HF was added up to 150 ml to remove the silicate fraction. Each sample was then swirled in its beaker at least once a day for 3 days, and decanted. New 48% conc. cold HF was added and the previous step repeated. The remaining organic residue was then washed with distilled water once a day for several days, by decanting, until reaching a pH of about 6. After the residue was neutralized once more, residues were briefly treated again with cold HCl (diluted to 20% of conc.) to remove any fluorosilicates. At this point, 1 tablet containing 20848 ± 3457 of *Lycopodium clavatum* spores (Batch 1031) was added to each residue to enable the estimation of palynomorph abundances (Stockmarr, 1971). A small number of residues rich in amorphous organic matter (AOM) were given special treatment with Calgon followed by 30–60 seconds of ultrasonic treatment. Table 2 details the treatment applied to these residues. An aqueous solution of Calgon (3% wt.) was added to each of the selected residues, which were then heated to just below boiling point for 40 mins. These residues were then sonicated for 30–60 seconds. The Calgon and ultrasound treatments were together effective in breaking down the amorphous organic matter before the residue was then sieved through a 10-µm nylon mesh. This step was used only for samples where the amorphous organic matter dominated the residue and prevented counting (Table 2). One drop of safranin o stain was then added to each sieved residue. Ten drops of residue were transferred onto a cover slip (40 X 24 mm) that had been covered with a mix of melted glycerine jelly (2 drops) and distilled water (6 drops). The

cover slip was allowed to dry on a covered slide warmer, typically for about 1 hour, and mounted onto microscope slides using additional melted glycerine jelly, following Evitt (1984). After the glycerine jelly had solidified, the slides were then ready for palynological analysis. The entire process for one sample took around 6 weeks, and 20 samples were processed as one batch. These slides were used for counting palynomorphs, for the morphological analysis of selected dinoflagellate cysts, and photographing important species (Plates 1–5). Only for six samples was all the residue used. In all other samples, surplus unsieved residue was stored in 5 ml glass vials filled with distilled water and couple drops of liquefied phenol to prevent microbial growth. Each sample/residue was given a consecutive laboratory identification number ordered by the age of the sample, the oldest sample being labeled 1 and the youngest 102 (Table 2). Accordingly, 102 samples were processed in total. The sample numbers therefore do not specifically record depth. Details of each sample are given in Table 2.

Table 2: Detailed information on each sample used in the present study from Site U1313, including weight of each dried filtrate processed for palynology, duration of ultrasound treatment, and the number of tablets of *Lycopodium clavatum* spores added.

Lab ID#	Sample details										Age (ka) Ferretti et al. (2015)	*L. clavatum* tablets	Total dry weight(g)	Hot Calgon Treatment (mins)	Ultrasound Treatment (secs)
	Hole	Core	Type	Section	Half	Top (cm)	Bot (cm)	Depth mcd)	Depth (rmcd)	Depth (mbsf)					
102	A	4	H	6	W	49	50	35.94	36.30	32.18	741.414	1	15.2	N/A	N/A
101	A	4	H	6	W	53	54	35.98	36.35	32.23	742.637	1	15.9	N/A	N/A
100	A	4	H	6	W	56	57	36.01	36.38	32.26	743.554	1	14.6	N/A	N/A
99	A	4	H	6	W	59	60	36.04	36.41	32.29	744.471	1	14.5	N/A	N/A
98	A	4	H	6	W	62	63	36.07	36.44	32.32	745.389	1	14.7	40	30
97	A	4	H	6	W	65	66	36.1	36.48	32.35	746.306	1	13.6	N/A	N/A
96	A	4	H	6	W	68	69	36.13	36.51	32.38	747.223	1	14.4	N/A	N/A
95	A	4	H	6	W	71	72	36.16	36.54	32.41	748.140	1	8.2	N/A	N/A
94	A	4	H	6	W	74	75	36.19	36.57	32.44	749.057	1	11	N/A	N/A
93	A	4	H	6	W	77	78	36.22	36.61	32.47	749.975	1	12.7	N/A	N/A
92	A	4	H	6	W	80	81	36.25	36.64	32.5	750.892	1	10	N/A	N/A
91	A	4	H	6	W	83	84	36.28	36.67	32.53	751.809	1	10.8	N/A	N/A
90	A	4	H	6	W	86	87	36.31	36.70	32.56	752.726	1	12.4	N/A	N/A
89	A	4	H	6	W	89	90	36.34	36.74	32.59	753.643	1	12.4	N/A	N/A
88	A	4	H	6	W	92	93	36.37	36.77	32.62	754.560	1	11.6	N/A	N/A
87	A	4	H	6	W	95	96	36.4	36.80	32.65	755.478	1	13.2	N/A	N/A
86	A	4	H	6	W	98	99	36.43	36.83	32.68	756.395	1	12.9	N/A	N/A
85	A	4	H	6	W	101	102	36.46	36.87	32.71	757.312	1	14.4	N/A	N/A
84	A	4	H	6	W	104	105	36.49	36.90	32.74	758.229	1	13.2	N/A	N/A
83	A	4	H	6	W	107	108	36.52	36.93	32.77	759.146	1	13.2	N/A	N/A
82	A	4	H	6	W	110	111	36.55	36.96	32.8	760.064	1	11.4	N/A	N/A

81	A	4	H	6	W	113	114	36.58	37.00	32.83	760.981	1	12.4	N/A	N/A
80	A	4	H	6	W	116	117	36.61	37.03	32.86	761.898	1	12.1	N/A	N/A
79	A	4	H	6	W	119	120	36.64	37.06	32.89	762.815	1	10.7	N/A	N/A
78	A	4	H	6	W	122	123	36.67	37.09	32.92	763.732	1	10.2	N/A	N/A
77	A	4	H	6	W	125	126	36.7	37.13	32.95	764.650	1	15.9	N/A	N/A
76	A	4	H	6	W	128	129	36.73	37.16	32.98	765.567	1	16	N/A	N/A
75	A	4	H	6	W	131	132	36.76	37.19	33.01	766.301	1	13	N/A	N/A
74	A	4	H	6	W	134	135	36.79	37.21	33.04	766.943	1	13.4	N/A	N/A
73	A	4	H	6	W	137	138	36.82	37.23	33.07	767.585	1	13.7	N/A	N/A
72	A	4	H	6	W	140	141	36.85	37.25	33.1	768.228	1	11.4	N/A	N/A
71	A	4	H	6	W	143	144	36.88	37.28	33.13	768.870	1	13.5	N/A	N/A
70	A	4	H	6	W	146	147	36.91	37.30	33.16	769.512	1	10	N/A	N/A
69	A	4	H	6	W	149	150	36.94	37.32	33.19	770.155	1	5.1	N/A	N/A
68	A	4	H	7	W	2	3	36.97	37.34	33.22	770.797	1	8.9	N/A	N/A
67	D	4	H	4	W	2	3	37.42	37.37	33.02	771.381	1	8.2	40	30
66	D	4	H	4	W	5	6	37.45	37.40	33.05	772.203	1	9.2	N/A	N/A
65	D	4	H	4	W	8	9	37.48	37.43	33.08	772.811	1	8.66	N/A	N/A
64	D	4	H	4	W	11	12	37.51	37.46	33.11	773.419	1	10.4	N/A	N/A
63	D	4	H	4	W	14	15	37.54	37.50	33.14	774.027	1	9.6	40	30
62	D	4	H	4	W	17	18	37.57	37.53	33.17	774.635	1	8.9	N/A	N/A
61	D	4	H	4	W	20	21	37.6	37.56	33.2	775.243	1	9.5	N/A	N/A
60	D	4	H	4	W	23	24	37.63	37.60	33.23	775.852	1	10.9	40	30
59	D	4	H	4	W	26	27	37.66	37.63	33.26	776.460	1	9.7	40	40
58	D	4	H	4	W	29	30	37.69	37.66	33.29	777.068	1	7.68	40	40
57	D	4	H	4	W	32	33	37.72	37.69	33.32	777.676	1	10.3	40	40
56	D	4	H	4	W	35	36	37.75	37.73	33.35	778.284	1	9	40	40
55	D	4	H	4	W	38	39	37.78	37.76	33.38	778.892	1	10.8	40	40
54	D	4	H	4	W	41	42	37.81	37.79	33.41	779.500	1	10.6	40	40

53	D	4	H	4	W	44	45	37.84	37.83	33.44	780.109	1	10.4	N/A	N/A
52	D	4	H	4	W	47	48	37.87	37.86	33.47	780.717	1	10.5	N/A	N/A
51	D	4	H	4	W	50	51	37.9	37.89	33.5	781.325	1	11	40	40
50	D	4	H	4	W	53	54	37.93	37.92	33.53	781.933	1	9.8	40	60
49	D	4	H	4	W	56	57	37.96	37.96	33.56	782.541	1	10	N/A	N/A
48	D	4	H	4	W	59	60	37.99	37.99	33.59	783.149	1	11.3	40	40
47	D	4	H	4	W	62	63	38.02	38.02	33.62	783.757	1	11.1	40	40
46	D	4	H	4	W	65	66	38.05	38.06	33.65	784.366	1	9.3	N/A	N/A
45	D	4	H	4	W	68	69	38.08	38.09	33.68	784.974	1	9.4	40	30
44	D	4	H	4	W	71	72	38.11	38.12	33.71	785.582	1	10.4	N/A	N/A
43	D	4	H	4	W	74	75	38.14	38.16	33.74	786.190	1	13.7	N/A	N/A
42	D	4	H	4	W	77	78	38.17	38.19	33.77	786.798	1	10.4	40	30
41	D	4	H	4	W	80	81	38.2	38.22	33.8	787.406	1	12	40	40
40	D	4	H	4	W	83	84	38.23	38.25	33.83	788.014	1	12.2	N/A	N/A
39	D	4	H	4	W	86	87	38.26	38.29	33.86	788.623	1	11.8	40	30
38	D	4	H	4	W	89	90	38.29	38.32	33.89	789.231	1	11.4	N/A	N/A
37	D	4	H	4	W	92	93	38.32	38.35	33.92	789.728	1	11.2	40	40
36	D	4	H	4	W	95	96	38.35	38.37	33.95	790.152	1	11.5	40	40
35	D	4	H	4	W	98	99	38.38	38.39	33.98	790.576	1	9.7	40	40
34	D	4	H	4	W	101	102	38.41	38.42	34.01	791.000	1	10.8	40	40
33	D	4	H	4	W	103	104	38.43	38.43	34.03	791.293	1	9.8	40	40
32	D	4	H	4	W	107	108	38.47	38.47	34.07	792.029	1	8.6	40	40
31	D	4	H	4	W	111	112	38.51	38.51	34.11	792.803	1	8.77	40	40
30	D	4	H	4	W	115	116	38.55	38.55	34.15	793.577	1	8.7	40	40
29	D	4	H	4	W	119	120	38.59	38.59	34.19	794.351	1	8.5	N/A	N/A
28	D	4	H	4	W	121	122	38.61	38.61	34.21	794.738	1	7.97	40	30
27	D	4	H	4	W	125	126	38.65	38.65	34.25	795.512	1	8.6	N/A	N/A
26	D	4	H	4	W	129	130	38.69	38.69	34.29	796.286	1	8.2	N/A	N/A

25	D	4	H	4	W	133	134	38.73	38.73	34.33	797.059	1	7.3	N/A	N/A
24	D	4	H	4	W	137	138	38.77	38.77	34.37	797.871	1	7.2	N/A	N/A
23	D	4	H	4	W	139	140	38.79	38.80	34.39	798.287	1	8.55	40	30
22	D	4	H	4	W	141	142	38.81	38.82	34.41	798.704	1	10.1	N/A	N/A
21	D	4	H	4	W	143	144	38.83	38.84	34.43	799.121	1	7.6	N/A	N/A
20	D	4	H	4	W	145	146	38.85	38.86	34.45	799.538	1	7.5	N/A	N/A
19	D	4	H	4	W	147	148	38.87	38.88	34.47	799.954	1	7.3	N/A	N/A
18	D	4	H	4	W	149	150	38.89	38.90	34.49	800.371	1	7.4	N/A	N/A
17	D	4	H	5	W	1	2	38.91	38.93	34.51	800.788	1	9.5	N/A	N/A
16	D	4	H	5	W	3	4	38.93	38.95	34.53	801.205	1	6.4	N/A	N/A
15	D	4	H	5	W	5	6	38.95	38.97	34.55	801.622	1	7.1	N/A	N/A
14	D	4	H	5	W	7	8	38.97	38.99	34.57	802.038	1	8.1	N/A	N/A
13	D	4	H	5	W	9	10	38.99	39.01	34.59	802.455	1	9.2	N/A	N/A
12	D	4	H	5	W	11	12	39.01	39.04	34.61	802.872	1	7.7	N/A	N/A
11	D	4	H	5	W	13	14	39.03	39.06	34.63	803.289	1	10.3	N/A	N/A
10	D	4	H	5	W	15	16	39.05	39.08	34.65	803.705	1	7.1	N/A	N/A
9	D	4	H	5	W	17	18	39.07	39.10	34.67	804.122	1	8.3	N/A	N/A
8	D	4	H	5	W	21	22	39.11	39.14	34.71	804.956	1	8.3	N/A	N/A
7	D	4	H	5	W	25	26	39.15	39.19	34.75	805.789	1	8.05	N/A	N/A
6	D	4	H	5	W	29	30	39.19	39.23	34.79	806.623	1	7.8	N/A	N/A
5	D	4	H	5	W	33	34	39.23	39.27	34.83	807.456	1	8.3	N/A	N/A
4	D	4	H	5	W	36	37	39.26	39.31	34.86	808.081	1	9.3	N/A	N/A
3	D	4	H	5	W	39	40	39.29	39.34	34.89	808.707	1	9.3	N/A	N/A
2	D	4	H	5	W	42	43	39.32	39.37	34.92	809.332	1	9.7	N/A	N/A
1	D	4	H	5	W	45	46	39.35	39.41	34.95	809.957	1	9.6	N/A	N/A

3.4 Statistical analysis

3.4.1 Constrained Cluster Analysis

In order to subdivide the record of dinoflagellate cyst assemblages into groups of similar species composition, constrained cluster analysis was performed based on the presence or absence of each species. Constrained Cluster Analysis was preformed using “R” studio software by using only in-situ dinocyst assemblages. Acritarchs were excluded because they had low concentrations or were absent from most samples. Pollen, spores and reworked palynomorphs were excluded because they also had low concentrations and do not provide a paleoecological signal in this study.

3.4.2 Modern Analogue Technique (MAT)

The Modern Analogue Technique (MAT; Rochon et al., 1999; de Vernal et al., 2001) was performed in order to numerically reconstruct water mass parameters (sea surface temperature, sea surface salinity, sea ice cover, and primary productivity) during MIS 19 based on dinocyst assemblages in this study. The method uses a measure of assemblage difference to compare down-core samples to each reference sample in a modern database. The modern database consists of sea-floor surface sediment samples for which modern dinoflagellate cysts have been documented. Each surface sediment sample, and its contained assemblage of modern dinoflagellate cysts, is linked to modern environmental parameters for the surface waters immediately above that sample. These environmental parameters are taken from the (World Ocean Atlas, 2013, v. 2), which has data for a large range of environmental parameters including sea-surface temperature, salinity, and ice cover for each month of the year. The method assumes that the depositional environmental conditions and taphonomic processes of the fossil dinocyst

assemblages are similar to those of the modern dinocyst database. The method can theoretically reconstruct environmental parameters for each of 12 months of the year, although the plausibility of each reconstruction must be assessed individually. In particular, it must be noted that for higher northern latitudes, many cyst-producing dinoflagellates will be encysted during the winter months (Dale, 1996). The cysts are metabolically dormant and their distributions are therefore not directly controlled by winter environmental factors.

"R" studio software was chosen to run transfer functions using two modern databases (reference set), one covering the Northern Hemisphere (*n*=1207) and the other restricted to the North Atlantic and Arctic (*n*=677) against the dinocyst assemblages in this study (U1313).

For both modern databases, reconstructions are given for August and February, representing summer and winter conditions. The modern databases, including both modern dinocyst assemblage data and associated environmental parameters are taken from the UQAM website, from GEOTOP at http://www.geotop.uqam.ca/en/bases-de-donnees/dinokystes.html.

3.4.2.1 Modern Analogue Technique based on modern Northern Hemisphere dataset (*n*=1207)

This modern database contains assemblage information on 1207 seafloor surface samples located across the Northern Hemisphere. Figure 9 shows the locations of the samples used in the dataset, as reported in de Vernal et al. (2013a, b), which is an update of the databases published by de Vernal et al. (1997, 2001, 2005), Rochon et al. (1999), Radi and de Vernal (2008), and Bonnet et al. (2010).

In order to yield the most accurate result using this method, every species in the fossil assemblages must occur in the modern database. However, the extinct species *Impagidinium cantabrigiense, "Pyxidinopsis striatoconulus"* and *Corrudinium*? *labradori* had to be removed from the U1313 dataset, inevitably somewhat reducing the reliability of reconstructions. We did not include reworked dinoflagellate cysts as they represent a taphonomic signal, not an ecological one. Also the reworked dinocysts and acritarchs had no significant abundance as only 18 specimens were recorded in total belonging to six taxa comprising the dinocysts: *Glaphyrocysta* sp. (6 specimens)*, Hystrichodinium* cf. *pulchrum* (2 specimens)*, Oligosphaeridium complex* (2 specimens)*,* and *Spinidinium* sp. (3 specimens); and the acritarchs *Veryhachium* spp. (3 specimens), and *Micrhystridium*? sp. (2 specimens).

All specimens of the genus *Brigantedinium* were grouped together as *Brigantedinium* spp. because preservational difficulties made it impossible to routinely distinguish *Brigantedinium simplex* and *Brigantedinium cariacoense*, even though both are documented in this study. Finally, it was decided to remove *Protoperidinium stellatum* because running MAT with this species gave a "no analogue" (N/A) result for 19 samples (Table 3) whereas removing *P. stellatum* gave a full analogue for all samples. The problem with *P. stellatum* was discovered after many attempts involving the exclusion of species one by one, starting with species having no or low abundance in these 19 samples. When comparing the MAT results before and after removal of *P. stellatum* there was no appreciable difference in reconstruction between samples before and after the removal of *P. stellatum*, with exception that these 19 samples now had reconstructed values. The modern North Atlantic dataset (see below) is a subset of the Northern

Hemisphere dataset and does not contain *P. stellatum*, which may explain the no-analogue problems. The species used to complete MAT analysis are listed in Table 4.

Table 3: The 19 samples for which a "no analogue" (N/A) result was returned before *P. stellatum* was excluded before final MAT reconstructions.

lab ID#	Age (ka)	Depth (mbsf)	MAT results	MIS
86	756.3948901	32.68	NA	MIS 18
85	757.3120863	32.71	NA	MIS 18
84	758.2292825	32.74	NA	MIS 18
74	766.9431174	33.04	NA	MIS 19
69	770.1547174	33.19	NA	MIS 19
66	772.2027151	33.05	NA	MIS 19
65	772.8108603	33.08	NA	MIS 19
19	799.9544705	34.47	NA	MIS 20
17	800.7880045	34.51	NA	MIS 20
16	801.2047715	34.53	NA	MIS 20
15	801.6215385	34.55	NA	MIS 20
14	802.0383055	34.57	NA	MIS 20
13	802.4550725	34.59	NA	MIS 20
12	802.8718395	34.61	NA	MIS 20
11	803.2886065	34.63	NA	MIS 20
10	803.7053735	34.65	NA	MIS 20
9	804.1221405	34.67	NA	MIS 20
7	805.7892085	34.75	NA	MIS 20
6	806.6227425	34.79	NA	MIS 20

Table 4: Dinocyst taxa used in the MAT analysis ((*) *Protoperidinium stellatum* was ultimately excluded; see text) including abbreviations of their names. Groupings used in the MAT analysis are shown. The abbreviations were also used in Canonical Correspondence Analysis (CCA).

Taxa name	Abbreviation	Notes
Achomosphaera andalousiensis	ACHO	
Ataxiodinium choane?	ATAX	
Bitectatodinium tepikiense	BTEP	
Brigantedinium cariacoense	BSPP	Grouped together
Brigantedinium simplex	BSPP	
Brigantedinium spp.	BSPP	
Impagidinium aculeatum	IACU	
Impagidinium pallidum	IPAL	
Impagidinium paradoxum	IPAR	
Impagidinium patulum	IPAT	
Impagidinium plicatum	IPLI	
Impagidinium sphaericum	ISPH	
Impagidinium strialatum	ISTR	
Nematosphaeropsis labyrinthus	NLAB	
Operculodinium centrocarpum sensu Wall & Dale 1966	OCEN	Grouped together
Operculodinium centrocarpum sensu Wall & Dale 1966 – short processes	OCEN	
Operculodinium centrocarpum – Arctic morphotype	OCEN	
Protoperidinium stellatum[*]	PSTE	
Pyxidinopsis reticulata	PRET	
Selenopemphix nephroides	SNEP	
Selenopemphix quanta	SQUA	
Spiniferites belerius	SBEL	
Spiniferites spp.	SSPP	Grouped together
Spiniferites coniconcavus	SSPP	
Spiniferites elongatus	SELO	
Spiniferites hyperacanthus	SMIR	Grouped together
Spiniferites mirabilis	SMIR	

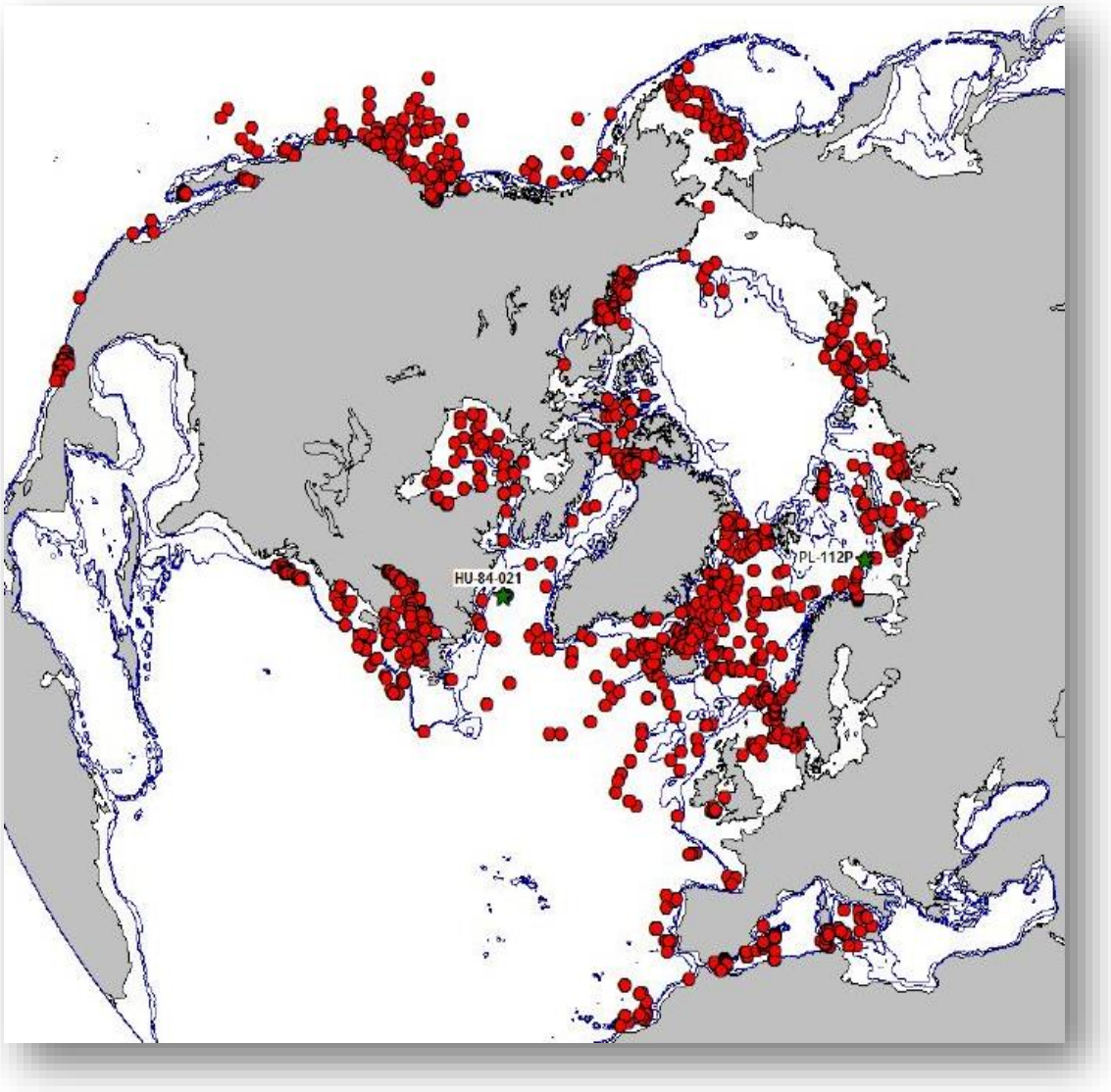

Figure 9: Location of surface sediment samples (red dots) in the *n*=1207 modern reference dataset (Radi and de Vernal, 2008; Bonnet et al., 2010) (from Bonnet et al., 2010, fig. 5a).

3.4.2.2 Modern Analogue Technique of MIS 19 based on modern North Atlantic dataset (*n*=677)

This database contains modern assemblage information on 677 seafloor surface samples located across the North Atlantic. Figure 10 shows the locations of the samples used in the dataset that was published by de Vernal et al. (2001, 2005). This database was used

for the Northern Hemisphere database except that the North Atlantic dataset contains only 30 taxa, requiring removal from the U1313 dataset of not only the extinct species *Impagidinium cantabrigiense, "Pyxidinopsis striatoconulus"* and *Corrudinium*? *labradori*, but also the following extant species that do not occur in the North Atlantic modern database: *Achomosphaera andalousiensis*, *Selenopemphix nephroides*, *Spiniferites* spp., *Impagidinium plicatum* and *Protoperidinium stellatum.* In addition, reworked dinoflagellate cysts were not included, as previously mentioned. Also *Brigantedinium simplex* and *Brigantedinium cariacoense* were grouped together as *Brigantedinium* spp. because of inadequate preservation.

After running MAT on the U1313 dataset against the modern North Atlantic dataset, "no analogue" (NA) result were obtained for 16 samples (Table 5). There are no obvious reasons for these "no analogue" results other than that there are presumably insufficient locations in the modern dataset with similar environmental conditions to these U1313 samples.

Table (5): The 16 samples that returned a “no analogue” (NA) result when running MAT on the U1313 dataset against the modern North Atlantic dataset (*n*=677)

lab ID#	Age (ka)	Depth (mbsf)	MAT results	MIS
86	756.39	36.83	NA	MIS 18
85	757.31	36.87	NA	MIS 18
83	759.15	36.93	NA	MIS 18
79	762.82	37.06	NA	MIS 19
37	789.73	38.35	NA	MIS 19
36	790.15	38.37	NA	MIS 19
35	790.58	38.39	NA	MIS 19
34	791.00	38.42	NA	MIS 19
32	792.03	38.47	NA	MIS 19
31	792.80	38.51	NA	MIS 20
29	794.35	38.59	NA	MIS 20
20	799.54	38.86	NA	MIS 20
17	800.79	38.93	NA	MIS 20
12	802.87	39.04	NA	MIS 20
11	803.29	39.06	NA	MIS 20
8	804.96	39.14	NA	MIS 20

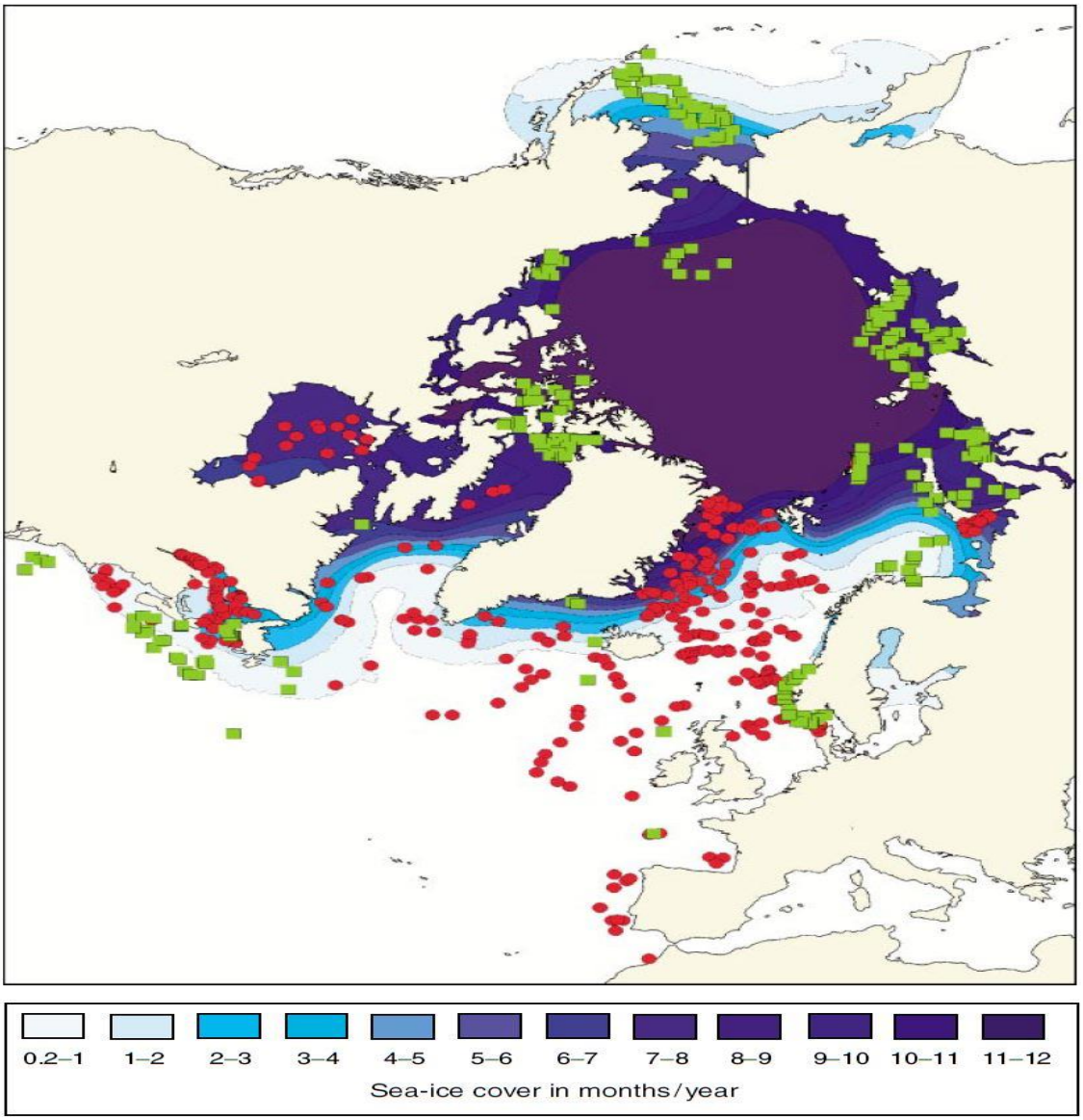

Figure 10: Location of surface sediment samples. Red circles and green squares represent the *n*=677 modern reference dataset as published by de Vernal et al. (1997), Rochon et al. (1999), and de Vernal et al. (2001). The modern sea-ice cover data sets is from the National Climate Data Center (NCDC) in Boulder, Colorado, which covers the years 1953 to 1990 (from de Vernal et al., 2001, plate 1).

In total, 20 groups of taxa (Table 4, minus *Protoperidinium stellatum*) were used when running the U1313 dataset against the Northern Hemisphere dataset (*n*=1207), and 15 groups of taxa (Table 4, minus *Achomosphaera andalousiensis*, *Selenopemphix*

nephroides, *Spiniferites* spp., *Impagidinium plicatum* and *Protoperidinium stellatum*) were used when running the U1313 dataset against the North Atlantic dataset (*n*=677). This analysis was performed using “R” studio software with the Bioindic package, a freeware program for the “R” platform developed by Joël Guiot and Yves Gally (CEREGE, CNRS). The Bioindic package is designed to perform many statistical analyses including transfer functions based on different methods, including the modern analogue technique. The Bioindic package used in the present study was obtained from GEOTOP at the Université Québec à Montréal (http://www.geotop.uqam.ca). This package contains a dataframe that adapted the dataset of the present study by expressing taxa abundances as per mil to match abundances in the modern dataset. The modern dataset was obtained from GEOTOP at http://www.geotop.uqam.ca.

3.4.3 Canonical Correspondence Analysis (CCA)

One of the most important statistical methods in paleoecology is multivariate analysis, and Canonical Correspondence Analysis (CCA) was used in the present study to elucidate the interactions between species in the dinocyst assemblages and available paleoenvironmental parameters. In this study, CCA was used to explore the relationships between the dinoflagellate cyst assemblages and their paleoenvironmental parameters based on foraminiferal isotope geochemistry, namely benthic $\delta^{13}C$, benthic $\delta^{18}O$, planktonic $\delta^{13}C$, and planktonic $\delta^{18}O$ (all expressed as VPDB). The validity of these relationships is enhanced by the fact that the dinocyst assemblages and the foraminifera providing the environmental parameters were obtained from the same samples.

Chapter 4 – Results

In this study 102 samples were processed, of which about 15 were found to have poor preservation or low concentrations that prevented the counting of 300 dinoflagellate cysts. In these samples, counts of between 104 and 298 dinoflagellate cysts were reached. All samples were included in the statistical analyses. A total of 31 dinocyst, five acritarchs and six reworked dinoflagellate cyst taxa were found in the present study. The raw counts of all taxa recorded are given in Appendix 2

4.1 Dinoflagellate cyst concentrations

Dinoflagellate cyst concentrations (Fig. 11) vary between 18.3 and 5074 cysts/g. High but variable concentrations occur in MIS 20, with a maximum value of 4698 cysts/g at 803.71 ka. Concentrations decline towards the top of MIS 20, reaching a minimum value of 18.3 cysts/g at 791.0 ka. These low concentrations continue steadily through the top of MIS 20 and into the fully interglacial part of MIS 19. At 779.50 ka, values abruptly rise to 1402 cysts/g and continue to increase with significant fluctuations reaching 4972 cysts/g through the middle and upper MIS 19. The fluctuating rise in concentrations continues into MIS 18 where a peak value of 5073 cysts/g is reached at 754.56 ka. Thereafter, concentrations decline fairly steadily through MIS 18 where they register a lowest value of 501 cysts/g in the highest sample analyzed at 741.41 ka.

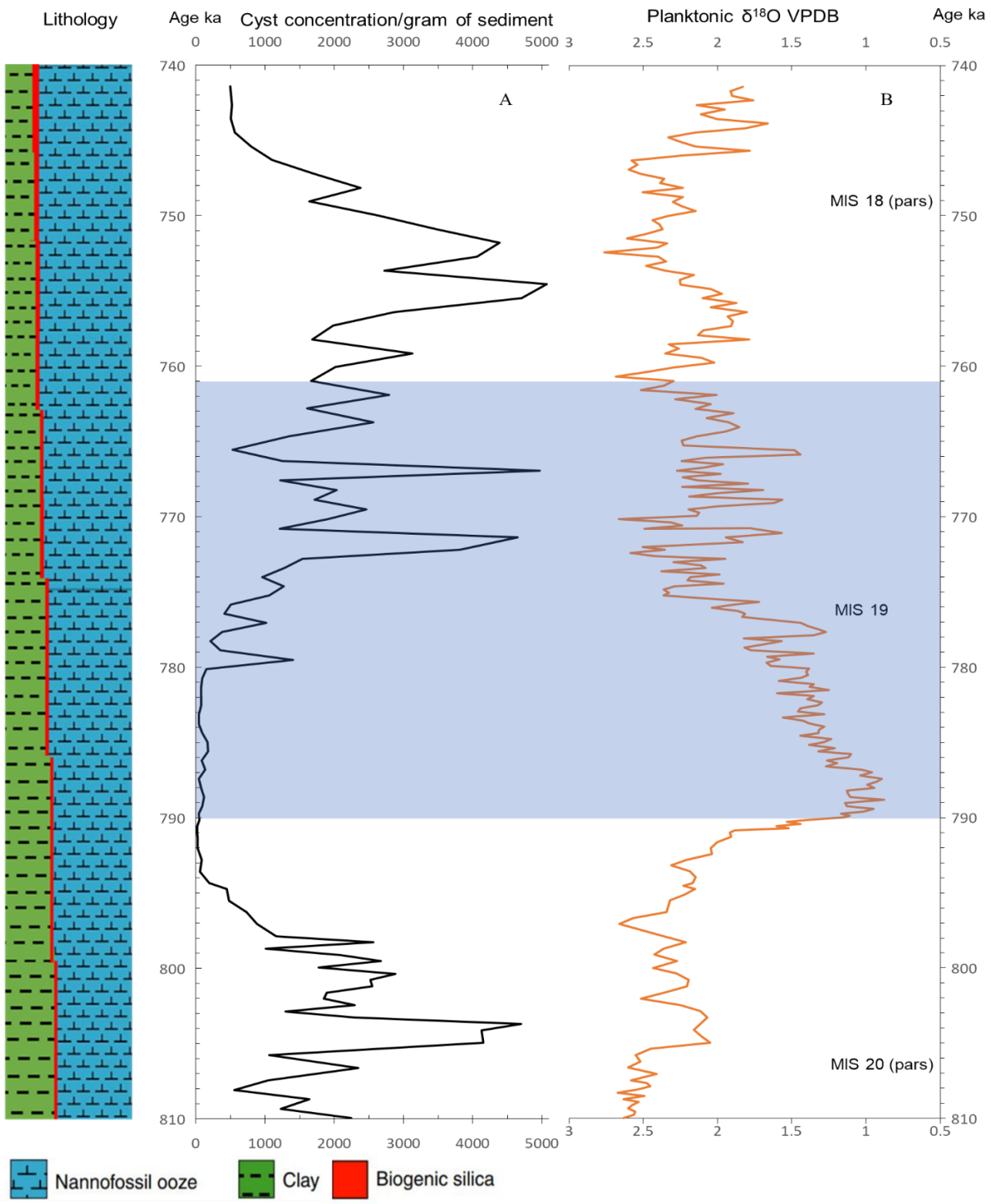

Figure 11: A, dinoflagellate cyst concentrations per gram of the total weight of the dried sample without the >63 µm foraminiferal fraction at Site U1313 (this study). Shaded area indicates MIS 19. B, planktonic $\delta^{18}O$ VPDB (foraminiferal data from Ferretti et al., 2015). Note the broadly inverse relationship between cyst concentrations and planktonic $\delta^{18}O$ values lithology adapted from (Expedition 306 Scientists, 2006, fig. 7).

4.2 Dinoflagellate Cyst Assemblages at IODP Site U1313

Dinoflagellate cyst assemblage compositions add detail to the paleoceanographic reconstructions for MIS 19, with major variations occurring in most of the 31 dinoflagellate cyst taxa enumerated.

The number of taxa per sample ranges between 6 and 21. The highest number of taxa (21) (Table 6) is recorded during MIS 18 and the lowest number (6) is recorded during MIS 19c. In only a few samples were reworked dinoflagellate cysts identified (Table 7). Assemblages comprise mainly *N. labyrinthus* and *O. centrocarpum* sensu Wall and Dale (1966). Several species of the genus *Impagidinium,* notably *I. aculeatum, I. cantabrigiense I. paradoxum*, *I. patulum, I. plicatum, I pallidum*, *I. sphaericum* and *I. strialatum,* are distributed through the entire investigated time interval.

Table 6: List of dinoflagellate cyst taxa in the studied interval.

Dinocyst taxa	**Figures**
Achomosphaera andalousiensis	Not figured
Ataxiodinium choane	Not figured
Bitectatodinium tepikiense	Plate 1, figs. 4–6
Brigantedinium spp. indet.	Plate 1, figs. 1–3
Impagidinium aculeatum	Plate 1, figs. 7–9
Impagidinium cantabrigiense	Plate 1, figs. 10–12
Impagidinium pallidum	Plate 1, figs. 13–15
Impagidinium paradoxum	Plate 2, figs. 1–3
Impagidinium patulum	Plate 2, figs. 4–6
Impagidinium plicatum	Plate 2, figs. 7–9
Impagidinium sphaericum	Plate 2, figs. 10–12
Impagidinium strialatum	Plate 2, figs. 13–15

Nematosphaeropsis labyrinthus	Plate 3, figs. 1–3
Operculodinium centrocarpum sensu W & D 1966	Plate 3, figs. 4–6
Protoperidinium stellatum	Plate 3, figs. 7–9
Pyxidinopsis reticulata	Plate 3, figs. 10–12
"Pyxidinopsis striatoconulus"	Plate 3, figs. 13–15
Selenopemphix nephroides	Plate 4, figs. 11,12
Selenopemphix quanta	Plate 4, figs. 13–15
Spiniferites elongatus	Plate 4, figs. 1–3
Spiniferites hyperacanthus	Plate 4, figs. 4–6
Spiniferites mirabilis	Plate 4, figs. 7–10
Spiniferites spp. indet.	Not figured

Table 7. Number of specimens of reworked dinoflagellate cysts and acritarchs with the samples in which they were found.

Taxa	Number of specimens	Sample #ID	Age of reworking
Glaphyrocysta sp.	6	51,31,28	Paleogene–Neogene
Hystrichodinium cf. *pulchrum*	2	30	Cretaceous?
Oligosphaeridium complex	2	15	Cretaceous
Spinidinium sp.	3	32,60,98	Cretaceous?
Micrhystridium? sp.	2	39,98	Paleozoic–modern
Veryhachium spp.	3	43,93,96	Ordovician–Neogene

4.3 Constrained Cluster Analysis

In order to subdivide the record of dinoflagellate cyst assemblages into groups of similar species composition, constrained cluster analysis was performed based on the presence or absence of each species. This resulted in the generation of eight assemblage zones, grouped by similarity as seen on the created dendrogram (Figure 12). These assemblage zones are as follows:

1. Assemblage biozone 1 (34.95–34.83 mbsf; 809.96–807.46 ka)

This biozone is characterized by the constant high relative abundance of *Nematosphaeropsis labyrinthus* with a gradual drop towards the end of this zone. *Operculodinium centrocarpum* and *Impagidinium aculeatum* on the other hand show an increase towards the end of this biozone with rather lower relative abundances *Impagidinium cantabrigiense* is also important in this zone. *Brigantedinium* spp is also documented in this biozone.

2. Assemblage biozone 2 (34.79–34.41 mbsf; 806.62–798.70 ka)

Although *N. labyrinthus* and *I. aculeatum* slightly increase, this biozone is characterized by the sudden increase of *Protoperidinium stellatum* which becomes one of the dominant species for this assemblage biozone, together with *Brigantedinium* spp. In addition, O. *centrocarpum* has its lowest occurrence for the studied interval in this zone. *Selenopemphix quanta* and *Selenopemphix nephroides also* have their highest abundances of the studied interval here.

3. Assemblage biozone 3 (34.39–34.29 mbsf; 798.29–796.29 ka)

In this biozone, *N. labyrinthus* and *O*. *centrocarpum* are the dominant species. Also, *I. aculeatum* is consistently abundant. The absence of *S. quanta, S. nephroides*, and *P. stellatum* contrasts with their strong abundance in the subjacent biozone.

4. Assemblage biozone 4 (34.25–33.71 mbsf; 795.51–785.58 ka)

This biozone is characterized by the presence of all *Impagidinium* species, led by *I. aculeatum* and *I. patulum* which have the highest abundances through the entire studied interval. *I. plicatum, I. sphaericum, I. pallidum I. paradoxum* and *I. strialatum* share similar abundances. As a result, *N. labyrinthus* and *O*. *centrocarpum* abundances decrease towards the top of this biozone. In addition, *Bitectatodinium tepikiense* has an important presence, although with relatively low abundances.

5. Assemblage biozone 5 (33.68–33.32 mbsf; 784.97–777.68 ka)

The presence of all species of the genus *Impagidinium* continues into this biozone although with lower abundances. *I. aculeatum* still dominates and *I. plicatum, I. sphaericum, I. pallidum I. paradoxum* and *I. strialatum* occur with low to moderate abundances. *N. labyrinthus* follows the same pattern as in biozone 4 by decreasing towards the top of this biozone. It has some fluctuations in the middle of this interval. On the other hand, *O*. *centrocarpum* increases through this biozone. The presence of *B. tepikiense* with low abundance is also recorded.

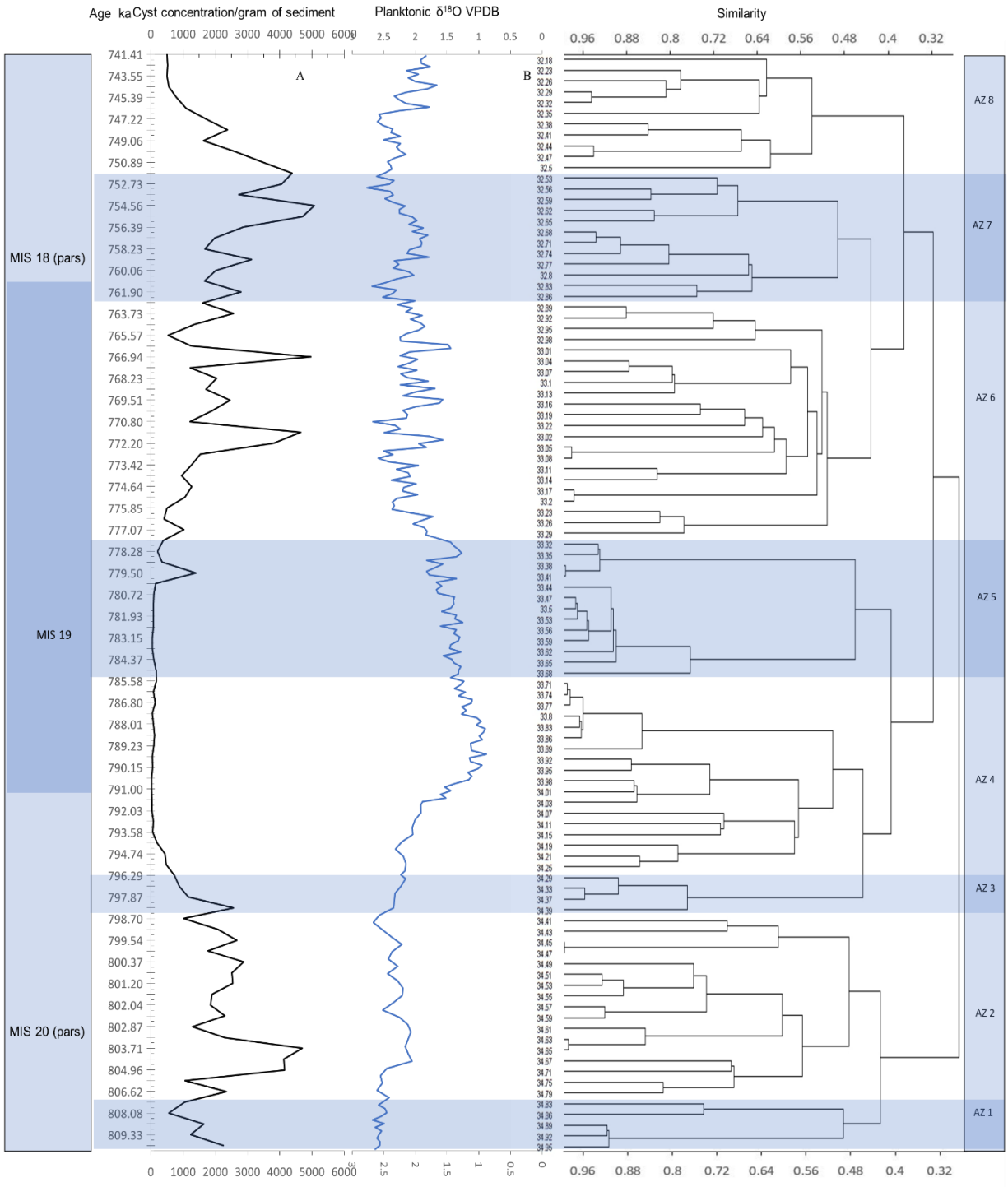

Figure 12: Constrained cluster analysis with assemblage biozones. A) Dinoflagellate cyst concentrations. B) Planktonic oxygen isotope (Planktonic data from Ferretti et al., 2015). Marine Isotope Stages 18, 19, and 20 are shown. AZ = Assemblage biozones (1–8).

6. Assemblage biozone 6 (33.29–32.89 mbsf; 777.07–762.82 ka)

In this biozone, *N. labyrinthus* and *O*. *centrocarpum* continue to be dominant. Also *P. stellatum* has a high abundance. Although *I. aculeatum* abundance appears to decrease in this zone, other *Impagidinium* species, *I. cantabrigiense*, *I. strialatum*, *I. sphaericum*, and I. *patulum*, slightly increase. *Brigantedinium* spp. is also recorded in this biozone.

7. Assemblage biozone 7 (32.86–32.53 mbsf; 761.90–751.81 ka)

This biozone features a substantial drop in all species of *Impagidinium*. The abundance of *I. aculeatum* continues to decrease in this zone. In addition, *I. cantabrigiense*, *P. stellatum* becomes one of the dominant species, and both *N. labyrinthus* and *O*. *centrocarpum* continue with high abundances. Important slight increases in *Spiniferites elongatus* and *Spiniferites hyperacanthus,* are documented. The highest occurrence of *B. tepikiense,* is also recorded.

8. Assemblage biozone 8 (32.5–32.18 mbsf; 750.89–741.41 ka)

This biozone is characterized by a sudden increase in *S. hyperacanthus* and *S. mirabilis* (which were grouped together) to become among the dominant taxon. Also, *I. aculeatum* increases in this biozone. Both *N. labyrinthus* and *O*. *centrocarpum* have high abundances, decreasing towards the end of this biozone. *B. tepikiense* and *I. cantabrigiense* are present with low abundances.

4.4 Canonical Correspondence Analysis (CCA)

Running Canonical Correspondence Analysis (CCA) plots distributions of species in controlled linear combinations of environmental variables. In this case we used carbon and oxygen isotopes represented by benthic $\delta^{13}C$ VPDB, benthic $\delta^{18}O$ VPDB, planktonic $\delta^{13}C$ VPDB, planktonic $\delta^{18}O$ VPDB. (Fig. 13).

Canonical Correspondence Analysis allows subdivision of the dincyst species into four quadrants defined by Axis 1 and 2, reflecting the sensitivity of these species to $\delta^{18}O$ and $\delta^{13}C$ values.

1. First Quadrant

The first quadrant contains dinoflagellate cysts for which abundances correspond to reduced benthic and planktonic $\delta^{13}C$ VPDB values. The species in this quadrant include: *I. aculeatum, I. strialatum* and *I. patulum.*

2. Second Quadrant

The second quadrant contains dinoflagellate cysts for which high abundances correspond to elevated benthic and planktonic $\delta^{13}C$ VPDB values. The species in this quadrant include: *S. membranaceus, S. coniconcavus B. tepikiense*, *I. plicatum, I. sphaericum, S. mirabilis+hyperacanthus*, and *I. paradoxum.*

3. Third Quadrant

This quadrant contains dinoflagellate cysts for which high abundances correspond to reduced benthic and planktonic $\delta^{18}O$ VPDB values. The species in this quadrant include: *O. centrocarpum* sensu Wall & Dale 1966, *Achomosphaera* spp. *Ataxiodinium choane, Pyxidiniopsis reticulata, Spiniferites* spp. *I. cantabrigiense*, and *"P. striatoconulus".*

4. Fourth Quadrant

The fourth quadrant contains dinoflagellate cysts for which high abundances correspond to heavier benthic and planktonic $\delta^{18}O$ VPDB values. The species in this quadrant include: *S. elongatus, S. nephroides, S. quanta, I. pallidum, Brigantedinium* spp., *N. labyrinthus,* and *P. stellatum.*

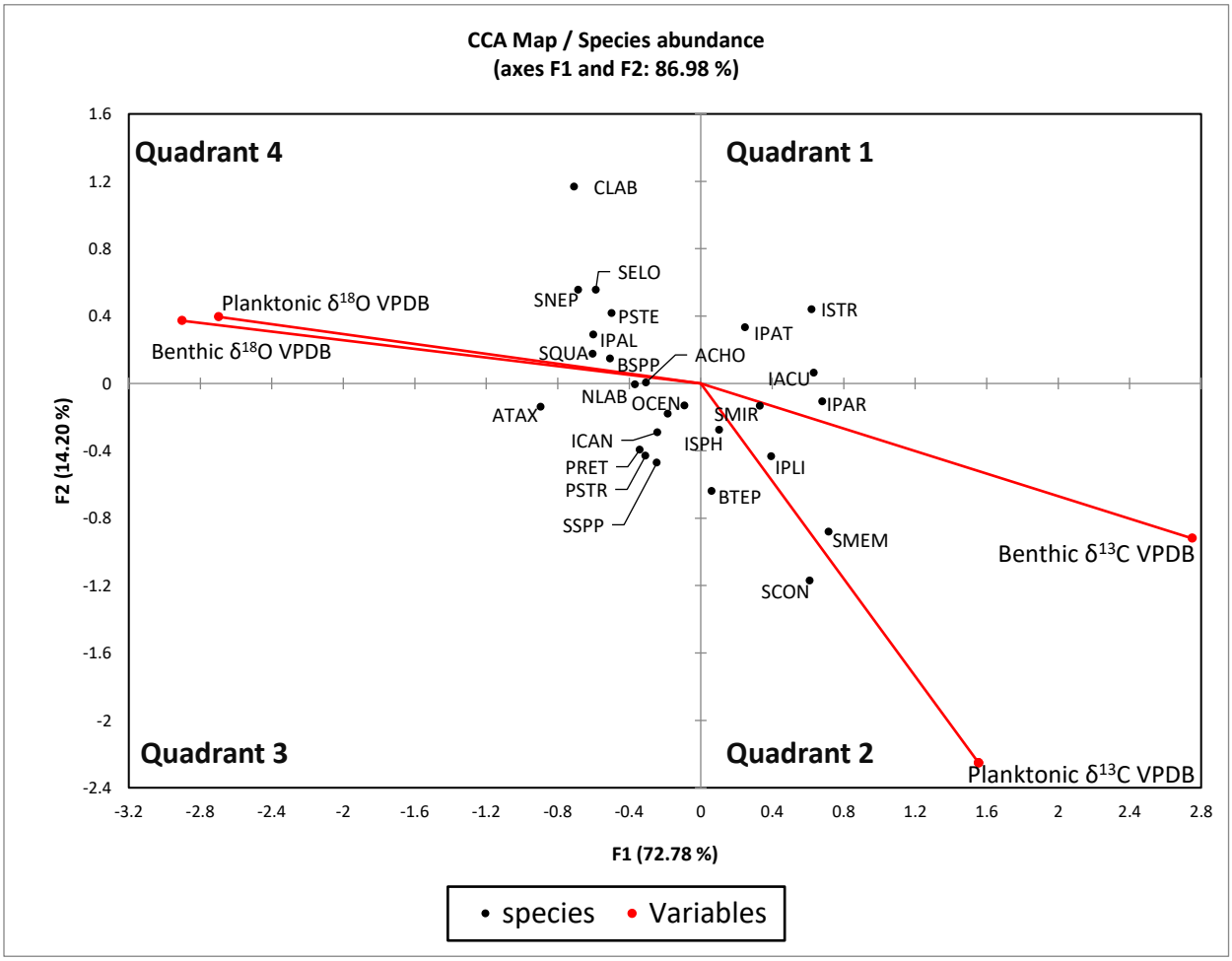

Figure 13: Canonical Correspondence Analysis (CCA) results shows distributions of species (Black dots with labels) in controlled linear combinations (variables) of benthic $\delta^{18}O$ VPDB (Ferretti et al., 2015), benthic $\delta^{13}C$ VPDB (Ferretti et al., 2015), planktonic $\delta^{18}O$ VPDB (Ferretti et al., 2015), planktonic $\delta^{13}C$ VPDB (Ferretti et al., 2015). Abbreviations (see Chapter 3 – Materials and methods, Table 4.

Chapter 5 – interpretation

5.1. Modern Analogue Technique

The Modern Analogue Technique (MAT) determines whether the compositions of assemblages recorded are strongly related to presently existing environmental conditions. In order to ensure the accuracy and reliability of dinoflagellate cyst transfer functions for the reconstruction of paleoenvironments from Site U1313 (MIS 20–18) assemblages, I performed validation tests with MAT on these assemblages against the Northern Hemisphere modern database (*n*=1207 sites) (de Vernal et al. 2013a, b). The validation tests were performed separately using the North Atlantic (*n* = 1207) and Arctic modern database (*n*=677 sites) (de Vernal et al. 2001).

5.1.1. Results of validation tests on the Site U1313 assemblages based on the North Atlantic–Arctic modern database (*n*=677)

The reconstructed environmental conditions include February and August sea-surface temperature (SSTF, SSTA) and February and August sea-surface salinity (SSSF, SSSA) based on the North Atlantic–Arctic modern database previously published by de Vernal et al. (2001, 2005). Results of the validation tests are shown in Fig. 14 A, C. The reconstructed February and August SSTs give a $R^2 > 0.89$ and Root Mean Square Error (RMSE) >1.8 °C. The salinity data show that salinity seems to be arranged around two values in February: 32 and 34.8 psu. A similar pattern in August is balanced around 32.5 and 35 psu (Fig 15 A, C). There is a scattered distribution below 31 psu in February and 30 psu in August. In addition, validation tests with MAT (Fig. 16A) indicate scattered distributions in sea-ice cover (ice mean, months/year).

5.1.2. Results of validation tests on the Site U1313 assemblages based on the Northern Hemisphere modern database (*n*=1207)

The reconstructed environmental conditions are February and August sea-surface temperature (SST_F, SST_A), and February and August sea-surface salinity (SSS_F, SSS_A). The database is an update and consilodation of the databases published by de Vernal et al. (1997, 2001, 2005), Rochon et al. (1999), Radi and de Vernal (2008), and Bonnet et al. (2010). Results from Site U1313 are illustrated in (Fig. 14 B, D) and show that the best reconstructions are obtained for February and August SSTs with a $R^2 > 0.95$ and RMSE >1.6 °C. Although the salinity data indicate a scattered distribution below 30 psu in February and 28 psu in August, most U1313 reconstructions are centered around 33.5 psu in February and around 33 during August (Fig 15 B, D), and this could be due to the lack of a freshwater influence from rivers and melting sea-ice. In addition, validation tests with MAT (Fig. 16 B) indicate that scattered distributions of sea-ice cover (I_COVER) (months/year) reveal interannual inconsistency.

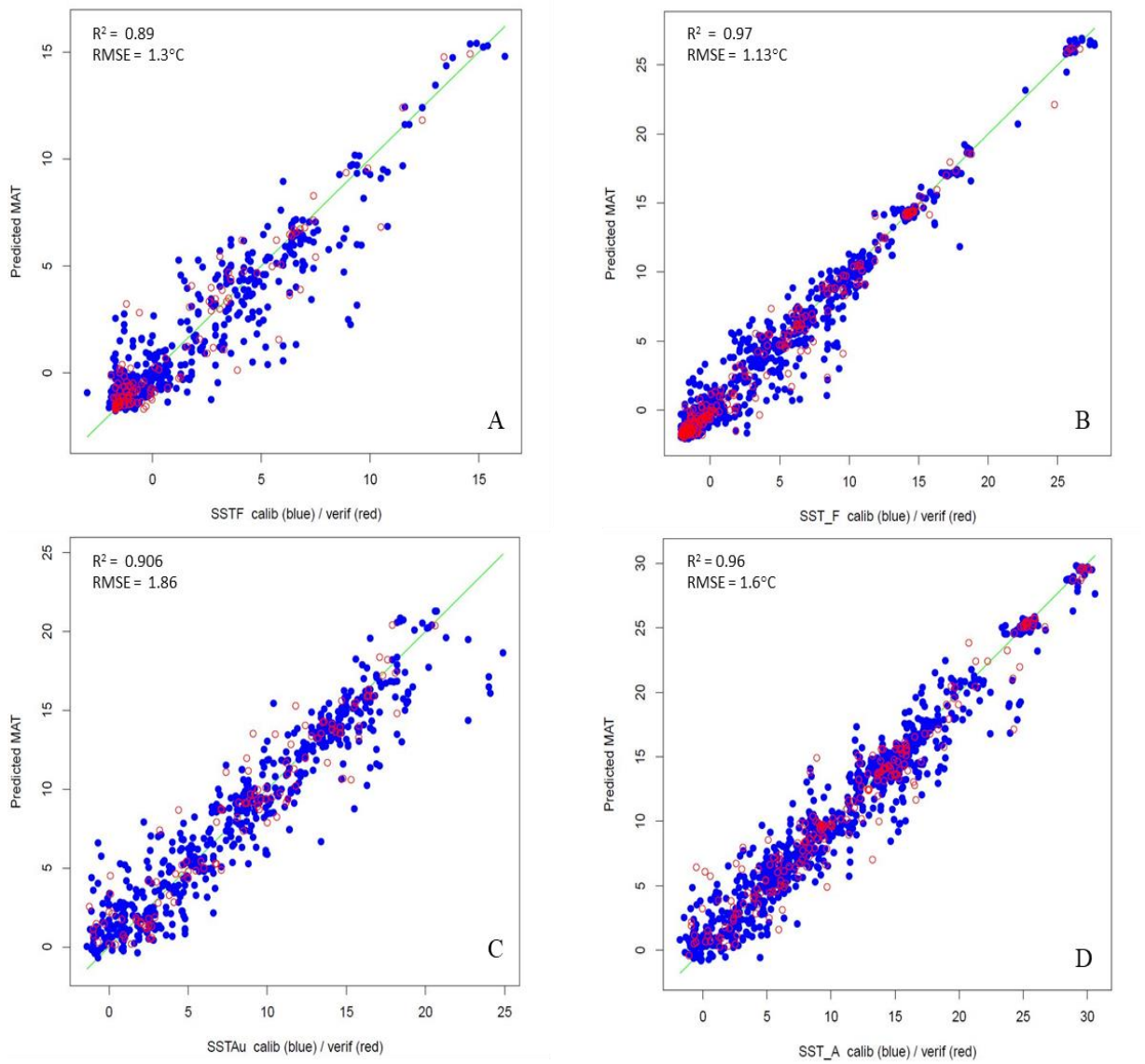

Figure 14: Results of validation tests performed with MAT on Site U1313 assemblages (this study) for: A, February sea surface temperature (SSTF) based on the North Atlantic–Arctic database; C, August sea surface temperature (SSTAu) based on the North Atlantic–Arctic database; B, February sea surface temperature (SST_F) based on the Northern Hemisphere database; D, August sea surface temperature (SST_A) based on the Northern Hemisphere database. Calibration (modern) datasets (blue dots) and validation (U1313) dataset (red circles).

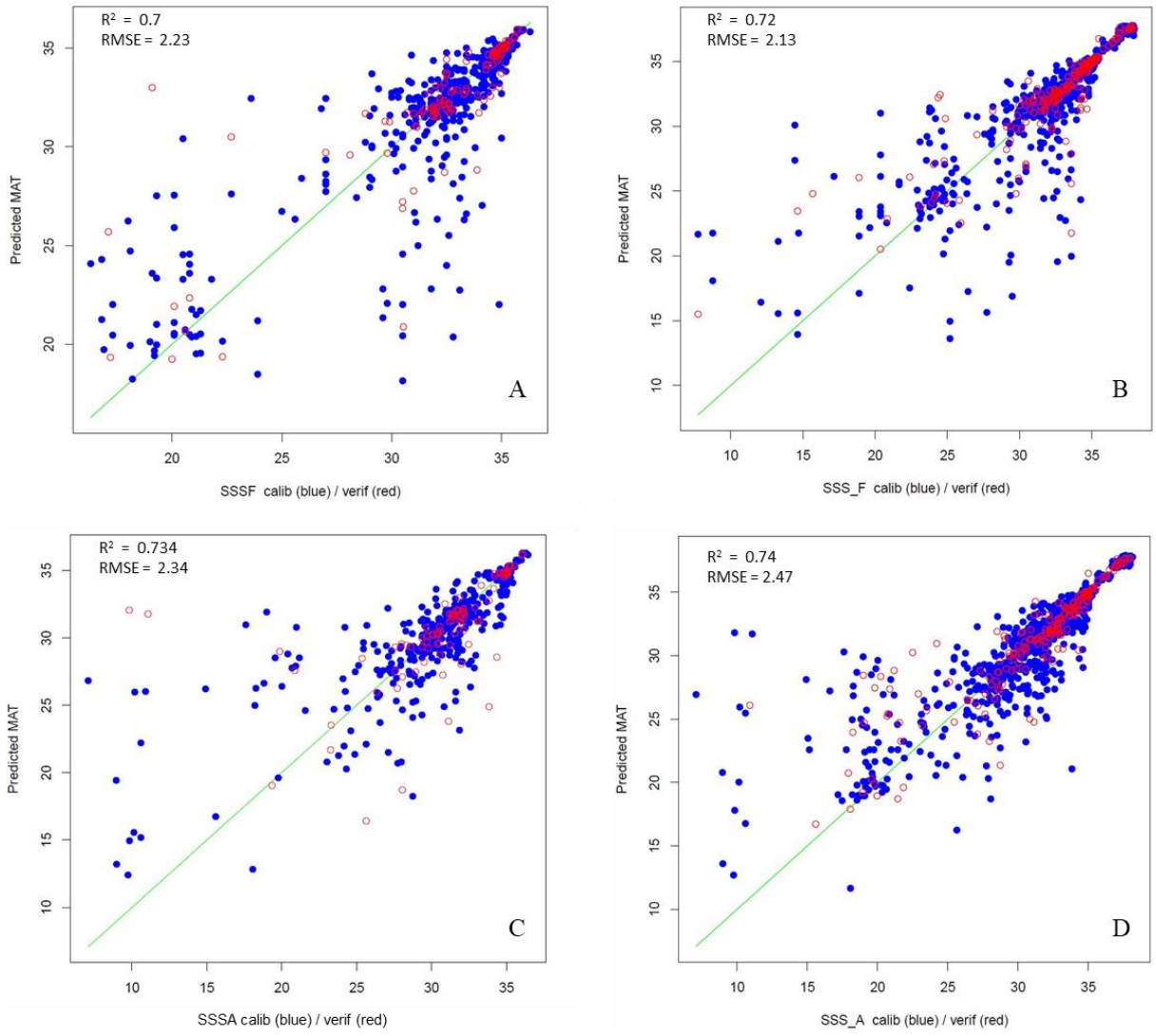

Figure 15: Results of validation tests performed with MAT on Site U1313 assemblages (this study) for: A, February sea surface salinity (SSSF) based on the North Atlantic–Arctic database; C, August sea surface salinity (SSSA) based on the North Atlantic–Arctic database; B, February sea surface salinity (SSS_F) based on the Northern Hemisphere database; D, August sea surface salinity (SSS_A) based on the Northern Hemisphere database. Calibration (modern) datasets (blue dots) and validation (U1313) dataset (red circles).

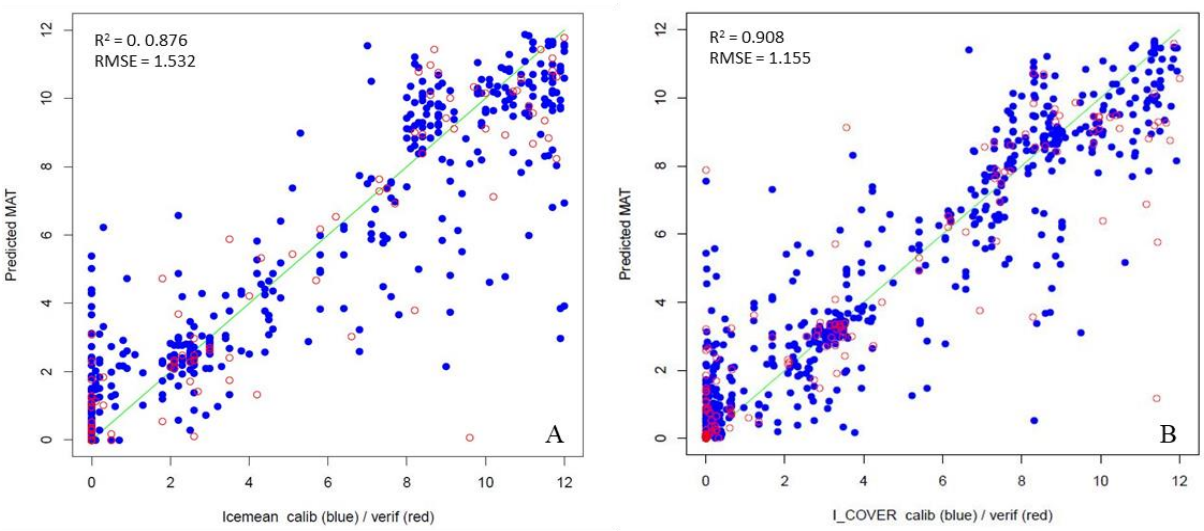

Figure 16: Results of validation tests performed with MAT on Site U1313 assemblages (this study) for: A, sea-ice cover (ice mean; months/year) based on the North Atlantic–Arctic database; B, sea-ice cover (I_COVER; months/year) based on the Northern Hemisphere database. Calibration (modern) datasets (blue dots) and validation (U1313) dataset (red circles).

5.1.3. Reconstructed environmental conditions

Using the Modern Analogue Technique to reconstruct environmental conditions for Site U1313, February and August sea-surface environmental conditions were chosen to represent winter and summer respectively.

5.1.4. Reconstructed August environmental conditions

The validation tests with MAT on the Site U1313 assemblages point to a strong response from the dinoflagellate cyst assemblages both at the scale of the North Atlantic and Arctic oceans and of the Northern Hemisphere in general. After running MAT based on the Northern Hemisphere database (*n*=1207), the reconstructed environmental parameters from the Site U1313 fossil assemblages are: summer and winter (in addition to February and August) sea surface temperatures (°C) (SST), summer and winter (in

addition to February and August) sea surface salinities (SSS), sea ice cover (months/year) (I_COVER), sea ice concentration (I_CON) and annual primary productivity (gC m^{-2} yr^{-1}) (PP). Some of these paleoenvironmental reconstructions are plotted on Fig 17. When running MAT based on North Atlantic–Arctic database, reconstructed environmental parameters for Site U1313 are: February and August sea surface temperature (°C) (SST), February and August sea surface salinity (SSS) and sea ice cover (ice mean, months/year).

5.1.4.1 Reconstructed August sea-surface temperature

Reconstructed August SSTs based on the Northern Hemisphere database (Fig. 17 B) show five major cooling peaks. The first is in MIS 20 at 804.12 ka with a temperature of 9°C, and the second is in MIS 20 at 799.95 ka with the lowest reconstructed SST of 6°C, the third is in MIS 19 at around 9°C at 772.2 ka, and the last one is in the beginning of MIS 18 which shows a major decrease in SST to 10°C at 752.73 ka. At the beginning of the reconstructed SSTs, there are steep fluctuations from high to low starting from 809.96 ka until at about 799.54 ka where the SST rises to 13°C and becomes relatively steady. This pattern continues until a sudden drop to 7.15°C at 772.20 ka, after which temperatures gradually rise to the highest reconstructed SST of 23.50°C at 756.39 ka and then decline to 11.82°C at 752.73 ka

Reconstructed August SSTs based on the North Atlantic–Arctic database (Fig. 17 A) show a similar pattern of cooling but with smoother fluctuations. At the beginning of the reconstructed interval, within MIS 20, fluctuations start from 809.96 ka until at about 799.95 ka when the SST drops to 6.6°C. SSTs start to rise from 799.12 ka and then become relatively steady, with a slight and stable increase to 18°C at 788.01 ka in MIS

19. A drop to around 9°C then occurs at 752.73 ka in MIS 18 when temperatures then start to gradually rise to about 18.5°C at 743.55 ka. Overall, the reconstructed August SST based on the North Atlantic–Arctic database is approximately up to 3 °C lower than that based on the Northern Hemisphere database.

5.1.4.2. Reconstructed August sea-surface salinity

Reconstructions using the Northern Hemisphere database (Fig. 17C) indicate an overall increase in SSS values towards the end of MIS 20 between 809.96 ka and 797.87 ka despite several drops of 32.1 psu at 805 ka and 32.6 psu twice at 803.7 ka and 802.5 ka. During the termination of MIS 20, SSSs start increasing to their highest value of 35.7 psu in the beginning of MIS 19 at 785.79 ka, fluctuating but remaining fairly high towards the end of MIS 19c at around 780.72 ka, after which there is a major decrease to 32.5 psu at 780.11 ka. SSSs then remain around 33±0.6 psu, with the exception of fluctuations when SSSs slightly increase to 34.5 towards the end of MIS 19 at 772.20 ka. Also during MIS 18, SSSs increase to 34.2, 34.3 and 34.7 psu at, 754.56 ka, 752.73 ka and 745.39 ka, respectively.

Reconstructed August SSSs based on the North Atlantic–Arctic database (Fig. 17 D) give the lowest salinity at 33.8 psu at 799.95 ka in MIS 20 and the highest at 35.6 psu at 741.41 ka during MIS 18. SSS reconstructions based on the North Atlantic–Arctic database do not closely match the reconstructed SSS using the Northern Hemisphere database, but they do fall within the range Root Mean Square Error.

5.1.4.3. Reconstructed sea ice cover (months/year) (I_COVER)

Fig. 17 E, F indicates that the reconstructed sea ice cover matches using both the Northern Hemisphere and North Atlantic–Arctic databases, and gives reconstructions of

at least 0.5 month/year sea ice cover from 806.62 ka to 799.12 ka in MIS 20, with two peaks during which sea ice cover lasted for about three months at 804.96 ka and 799.95 ka. During MIS 19, ice cover is registered in two consecutive samples, representing 0.5 month/year at 772.81 ka and 0.8 month/year at 772.20 ka. At the beginning of MIS 18, based on the samples covered in this study, sea ice cover occurred for 0.5 month/year at 752.73 ka.

5.2 Dinoflagellate cyst assemblages at IODP Site U1313 and their ecological distribution

This section explains the response of the dinoflagellate cysts and their ecological distribution based on the relative abundances of dinocyst taxa and the results of statistical analysis including constrained cluster analysis, canonical correspondence analysis and MAT at Site U1313.

The dinoflagellate cyst assemblages can be placed into several groups based on their sensitivity to such environmental factors as temperature and salinity or nutritional strategy. The most abundant and paleoecologically important species identified in this study are grouped in the following sections.

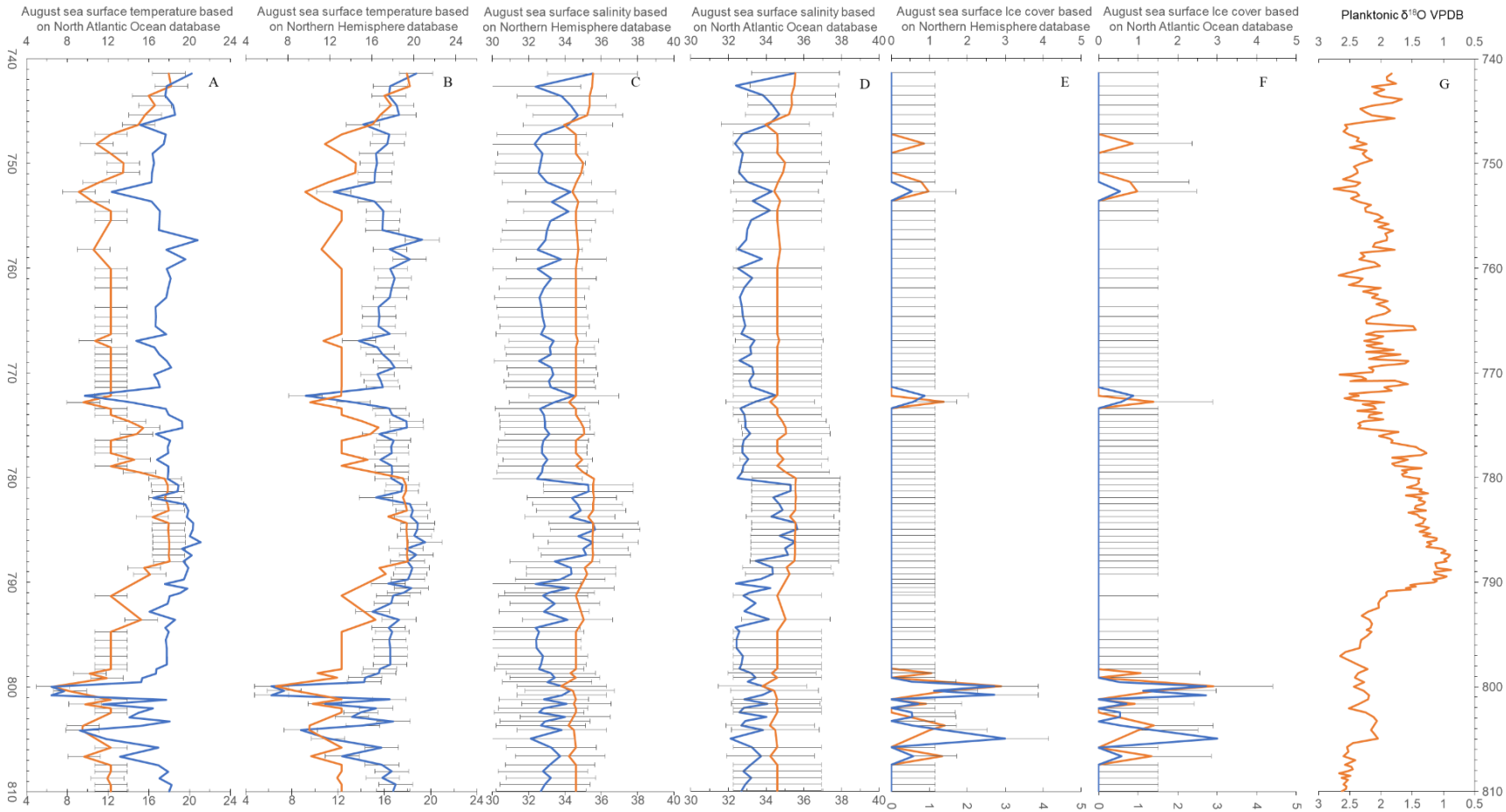

Figure 17: Paleoenvironmental reconstructions at Site U1313 using dinoflagellate cyst assemblages and based on the Modern Analog Technique. A, August sea surface temperature based on the North Atlantic–Arctic database; B, August sea surface temperature based on the Northern Hemisphere database; C, sea surface salinity based on the Northern Hemisphere database; D, August sea surface salinity based on the North Atlantic–Arctic database; E, sea surface ice cover months/year based on the Northern Hemisphere database; F, August sea surface ice cover months/year based on based on the North Atlantic–Arctic database; G, Planktonic $\delta^{18}O$ VPDB (Planktonic data from Ferretti et al., 2015). Error bars= root mean square error (RMSE).

5.2.1 North Atlantic Current indicator

Operculodinium centrocarpum sensu Wall and Dale (1966)

This is the cyst of *Protoceratium reticulatum* (Paez-Reyes and Head, 2013). It is a cosmopolitan species but has been used as an indicator of the North Atlantic Current (De Schepper et al., 2009, 2013; Hennissen et al., 2014, 2015). *O. centrocarpum* sensu Wall and Dale 1966 is associated with cold to moderate and mesotrophic to eutrophic environments with wide range from polar to subtropical water masses (Bonnet et al., 2012; Zonneveld et al., 2013). In the present study, *O. centrocarpum* has an average relative abundance of 15% at the end of MIS 20 (Fig. 18), declining near the transition between MIS 20 and MIS 19 dropping to 3% at the very beginning of MIS 19 at 790.6 ka, after which it continues with very low abundances during the MIS 19c–19b transition at ~784 ka. It then rises in relative abundance during MIS 19b and continues rising with two abundance peaks of 54.6% and 58.5% at 779 ka and 746.3 ka respectively. Although *O. centrocarpum* is ubiquitous throughout the studied samples, its abundance seems correlated to MAT-reconstructed environmental proxies, especially salinity. High abundance corresponds to high salinity influenced by low to moderate August SST. When *O. centrocarpum* comprises 25% or more of the total dinocyst assemblage it occurs during 12–21°C for August SSTs, 32.4–35.2 psu for August SSSs, and 194–356 (gC m^{-2} yr^{-1}) for primary productivity. The drop in abundance at the termination of MIS 20 reflects changes in the environmental conditions which is best explained by a northward shift in the NAC away from Site U1313 resulting in a replacement of the NAC by oligotrophic waters of the subtropical gyre at this site. *O. centrocarpum* increases significantly starting around 783.56 ka caused by melting water during the

summer season that caused a reduction in salinities and surface waters are replaced by cold, nutrient-rich water.

5.2.2 Open Marine Species

5.2.2.1 *Nematosphaeropsis labyrinthus*

An outer neritic to oceanic species tolerant of fluctuating conditions (Hennissen et al., 2014). *N. labyrinthus* can be found in coastal sites where low salinity is recorded as a result of river discharge such as in the White Sea (Golovnina and Polyakova, 2004; Novichkova and Polyakova, 2007). *N. labyrinthus* is also linked to cold and mesotrophic conditions of the subpolar gyre (Bonnet et al., 2012; Zonneveld et al., 2013), and is considered a sub-polar species in the North Atlantic (Hennissen et al., 2017). In this study, its relative abundance begins high with a value of 50% (Fig. 18), then drops to 10% at 800.4 ka before rising again at the end of MIS 20 with a peak of 66% at 798.3 ka. It drops significantly at the boundary between MIS 20 and MIS 19 to 3% and it remains low until 779.5 ka where it starts rising with fluctuations through the remainder of MIS 19 and the beginning of MIS 18. When *N. labyrinthus* is represented by 25% or more of the total dinocyst assemblage, it occurs within an August SST range of 6–21 °C, August SSS range of 32–35 psu and primary productivity range of 141–356 (gC m^{-2} yr^{-1}). At Site U1313, the main drop in *N. labyrinthus* abundance is associated with high salinity and relatively high August temperature as a result of the northern shift of subtropical waters. In addition, *N. labyrinthus* seems to have a high abundance at the MIS 20/19 and MIS 19/18 transitions which makes it a reliable indicator of transitional environments.

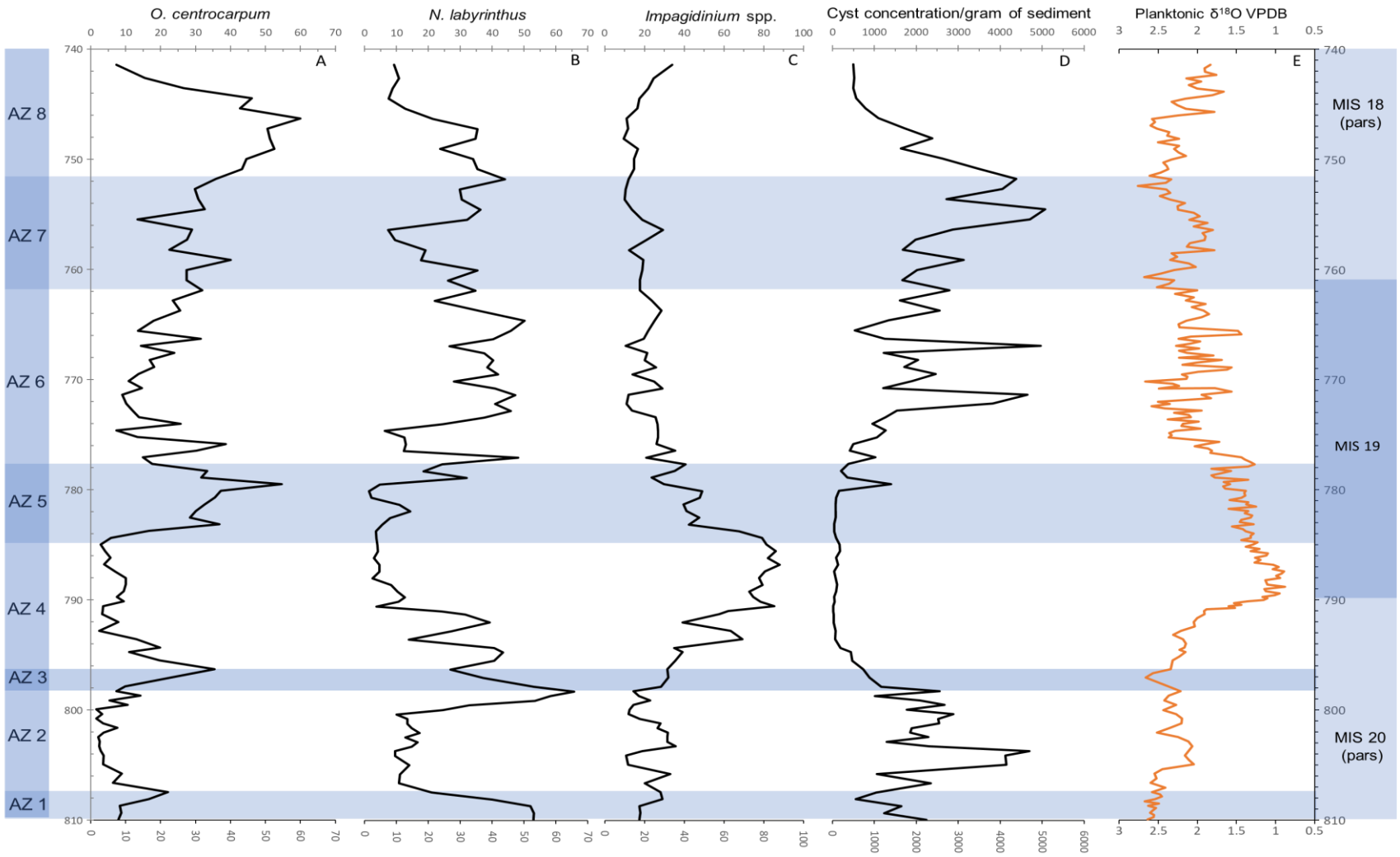

Figure 18: The relative abundance of open marine dinoflagellate cyst species at Site U1313. A) The North Atlantic Current indicator *Operculodinium centrocarpum*. B) *Nematosphaeropsis labyrinthus*. C) *Impagidinium* spp. D) Dinoflagellate cyst concentration. E) Planktonic foraminiferal oxygen isotope data (from Ferretti et al., 2015). Heavily shaded area indicates MIS 19.

5.2.2.2 *Impagidinium* spp.

Impagidinium spp. comprises the extant *I. aculeatum, I. pallidum, I. paradoxum, I. patulum, I. plicatum*, *I. sphaericum*, and *I. strialatum*, and the extinct *I. cantabrigiense*. It collectively represents the oceanic signal. *Impagidinium* is one of the most dominant genera in this study, represented mainly by autotrophic taxa including *I. aculeatum* which is the main species associated with the warm and nutrient-poor waters of the subtropical gyre (Bonnet et al., 2012; Zonneveld et al., 2013). Other *Impagidinium* species occur with similar distribution patterns throughout the studied interval but with lower abundances. Of these, *I. patulum I. sphaericum* and *I. paradoxum* occur in oligotrophic–mesotrophic environments today (Zonneveld et al., 2013). *Impagidinium pallidum* differs from the other *Impagidinium* species in being linked to colder and more nutrient-rich water masses of the subpolar gyre (Zonneveld et al., 2013), and its absence at the beginning of MIS 19 is linked to the dominance of subtropical waters at the Site U1313 (this study) at this time. The relative abundance average of *Impagidinium* spp. is 33% through MIS 20 and this then rises at the transition between MIS 20 and MIS 19 to a peak of 93% at 790.58 ka and remains relatively high at the beginning of MIS 19 with relative abundance of 85% at 783.76 ka. Abundances then drop to between 12 and 51% for the remainder of the sampled interval.

When *Impagidinium* species comprise 25% or more of the total dinocyst assemblage, they occur within an August SST range of 11–21 °C, August SSS range of 32.4–35.5 psu, and primary productivity range of 176–356 (gC m^{-2} yr^{-1}). The high abundance of *I. aculeatum* and *I. patulum* during the onset of MIS 19 indicates that the northern margin of the subpolar gyre had expanded northwards to cover Site U1313. In

addition, the major drop of *I. aculeatum* and *I. paradoxum* at the end of MIS 19 starting at 778.89 ka signals the demise of oligotophic and/or subtropical conditions.

5.2.3 Species associated with cooler waters

Modern cyst distributions (e.g. Rochon et al., 1999; Zonneveld et al., 2014) all link the following species to cooler waters.

5.2.3.1 *Bitectadodinium tepikiense*

This is a cool-water species abundant today in the area between the subtropical and arctic front (Zonneveld et al., 2013), and may indeed be characteristic of the arctic front (Dale, 1985; Bakken and Dale, 1986). It occurs in both oligotrophic and eutrophic waters. Despite its low abundance and occurrence in a wide range of temperatures and salinities, it is associated in the present study with cool to moderate water masses where high primary productivity and salinity are recorded. This species is not present until the boundary between MIS 20 and MIS 19, where it enters the record with values below 5%, and maintains low values until the boundary between MIS 19 and MIS 18. Here, it shows an important rise in relative abundance to 9% and then drops to an average of 2%. The sudden increase of *B. tepikiense* at the onset of MIS 18 indicates a southward shift of the subpolar–temperate boundary over Site U1313 at this time, its maximum abundance occurring at 759.15 ka.

5.2.3.2 *Spiniferites elongatus*

Spiniferites elongatus is characteristic of open-marine conditions with seasonally reduced salinities (Zonneveld et al., 2013). It is a temperate to polar autotrophic species associated with cold temperature and low salinity caused by melting ice (Bonnet et al.,

2012; Zonneveld et al., 2013). At Site U1313, the relative abundance is less than 3%, with specimens recorded mainly during the two glacial stages, MIS 20 and MIS 18. It is almost absent from the interglacial MIS 19. Its highest abundances, recorded in both glacial stages MIS 20 and MIS 18, shows that it is indicative of subpolar waters covering Site U1313. *S. elongatus* is not recorded during the MIS 20/19 and MIS 19/18 transitional intervals.

5.2.3.3 *Impagidinium pallidum*

This species is associated today with open marine conditions and is found mostly in polar to cool temperate waters (Mudie, 1992; Solignac et al., 2009; Patterson et al., 2011; Zonneveld et al., 2013), although it appears to have had a somewhat wider temperature tolerance in the Pleistocene and Pliocene (De Schepper et al., 2011). The relative abundance in the present study is always less than 3%. This species occurs at the end of MIS 20, then disappears at the beginning of MIS 19, appearing again with low abundances in the middle of MIS 19 where it continues with variability into MIS 18.

5.2.4 Protoperidiniacean species

Protoperidiniacean species are heterotrophic and hence primarily represent a productivity signal, although their susceptibility to degradation by oxidizing bottom waters can introduce a taphonomic component (Reichart and Brinkhuis, 2003). The group comprises *Brigantedinium* spp., *Protoperidinium stellatum, Selenopemphix quanta* and *S. nephroides.* Today in the higher northern latitudes, the distribution of protoperidiniacean species is generally linked to areas adjacent to the polar front as these are characterized by high nutrient/food availability (de Vernal et al., 2005; Radi et al., 2007; Radi and de Vernal, 2008a, b; Zonneveld et al., 2010; Price and Pospelova, 2011;

Bonnet et al., 2012; Zonneveld et al., 2013). *Brigantedinium* spp. is a heterotrophic group of species linked to subpolar mesotrophic–eutrophic conditions (Zonneveld et al., 2013). *Brigantedinium* spp. dominates the protoperidiniacean group, with relative abundances (of the total cyst assemblage) reaching 61% during MIS 20 at 800 ka. It then it disappears throughout the MIS 20/19 transition before suddenly appearing again with relatively high abundances of 48% during MIS 19 at 773.76 ka after which its presence continues with fluctuations of high and low relative abundances throughout MIS 18/19 transition until it disappears during MIS 18 at 752.73 ka. When *Brigantedinium* spp. is represented by 25% or more of the total dinocyst assemblage it occurs within ranges of 6–19°C in August SST, 32.1–34.6 psu August SSS, and 141–230 (gC m^{-2} yr^{-1}) in primary productivity. The high abundances of *Brigantedinium* spp. before the termination of MIS 20 and just before the onset of MIS 18 implies that subpolar waters were covering Site U1313. More importantly, the absence of *Brigantedinium* spp. from the onset of MIS 19 indicates that subtropical waters had moved northwards, extending over Site U1313 several thousand years before the start of MIS 19.

The protoperidiniacean group also comprises cysts of *Protoperidinium stellatum*, a subtropical to temperate species occurring today in mesotrophic and eutrophic waters. Today, the highest abundances (up to 26%) occur in upwelling areas (Bonnet et al., 2012; Zonneveld et al., 2013). It is found in just 34% of the samples examined in this study, but may occur with relatively high abundances. It reaches 33% during MIS 20 at 806.62 ka and then continues with fluctuations of high and low abundances until 799.12 ka where it disappears throughout the MIS 20/19 transition. It then suddenly appears again with low relative abundances of 6% during MIS 19 at 772.20 ka where its present continues with

relatively low abundances throughout MIS 18/19 transition until it disappears during MIS 18 at 752.73 ka. When *P. stellatum* is represented by 25% or more of the total dinocyst assemblage, its occurrence represents cold, low-salinity waters, with August SSTs in the range of 9–17°C, August SSSs in the range of 32.5–34.0 psu, and primary productivity in the range of 190–220 (gC m^{-2} yr^{-1}). During the termination of MIS 19, the high abundances of *P. stellatum* suggest an upwelling caused SSTs to drop resulting in favourable conditions for *P. stellatum* abundance to increase, marking the start of the MIS 19/18 transition.

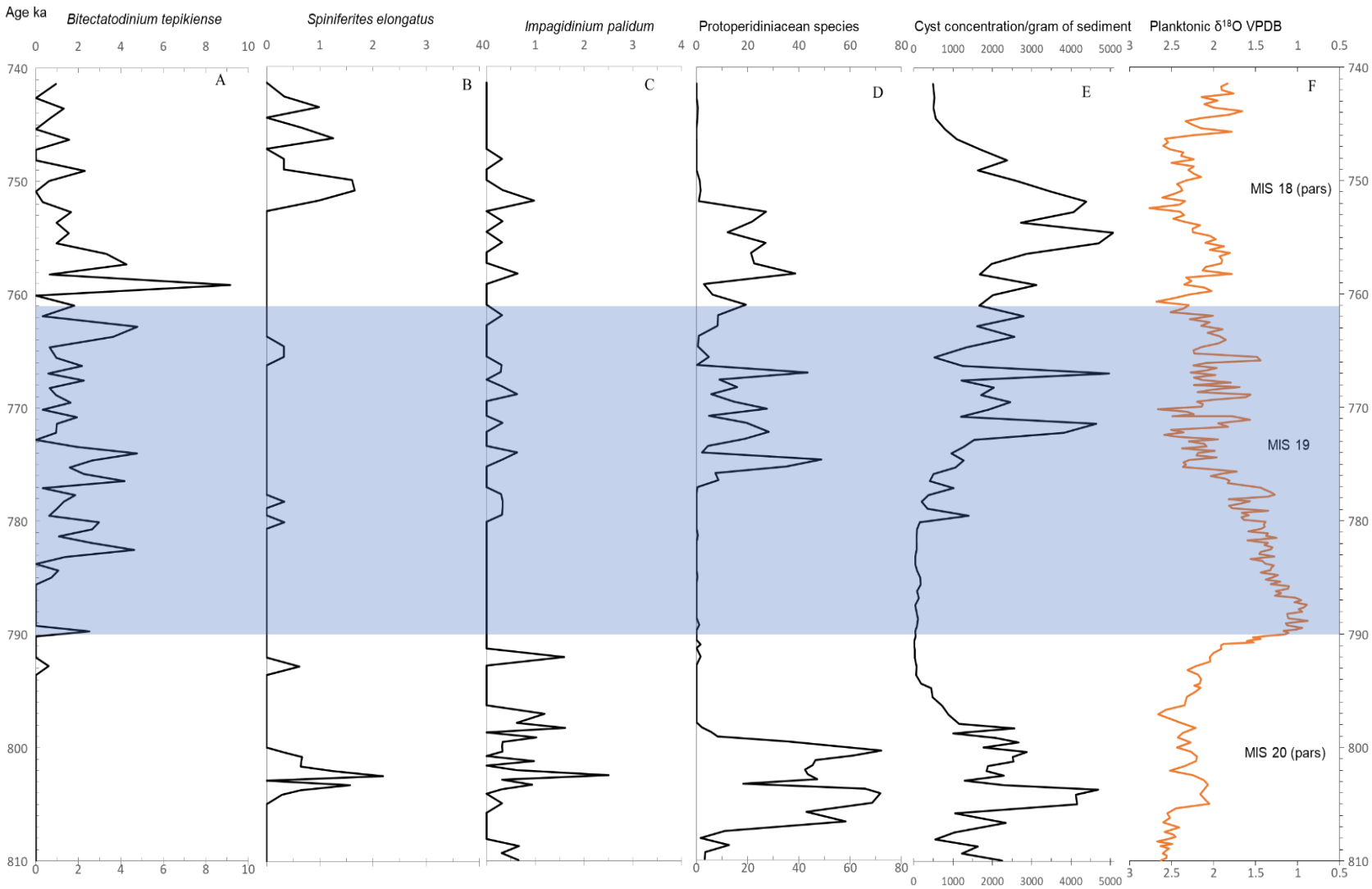

Figure 19: Relative abundance of dinoflagellate cyst species typically associated with cooler waters in Holes U1313A, D. A) *Bitectadodinium tepikiense*. B) *Spiniferites elongatus*. C) *Impagidinium pallidum*. D) Dinoflagellate cyst concentration. E) Planktonic oxygen isotope (Planktonic data from Ferretti et al., 2015). F) Protoperidiniacean species. Shaded area indicates MIS 19.

Chapter 6 – Discussion

6.1 Comparison of palynological data with high-resolution oxygen isotope, nannofossil, and alkenone SST records of MIS 19

The palynological data of the present study are generated from the same samples used for the high-resolution oxygen isotope analysis of Site U1313 (Ferretti et al., 2015). The nannofossil record of Site U1313 (Emanuele et al., 2015) is also from this sample set. An opportunity therefore exists to compare directly these three sets of data (Fig. 21). In addition, a detailed reconstruction of SSTs based on alkenones (relative abundance of the $C_{37:4}$ alkenone) is available for MIS 19 at this site (Naafs et al., 2011; reproduced in Emanuele et al., 2015, fig. 3) and is compared with these other data.

6.1.1 High-resolution oxygen isotope record of MIS 19

The benthic and planktonic foraminiferal $\delta^{18}O$ values obtained from Ferretti et al. (2015) cover the interval from ~810 to 740 ka (Ferretti et al., 2015, p. 98), thus extending beyond the interval sampled in the present study. The Ferretti et al. study is also at higher resolution, with sample spacing representing an average of ~250 years for MIS 19 compared with ~678 years for the present palynological study. The oxygen isotope record provides the age control for this interval of U1313 as well as allowing changes in the paleoceanographic and climatic history to be reconstructed through MIS 19.

6.1.2 High-resolution nannofossil record of MIS 19

The nannofossil record is from Emanuele et al. (2015) and extends from 803 to 759 ka (late MIS 20 – early MIS 18) using the time scale of Ferretti et al. (2015). The sample spacing of 1 cm used in this study represents an average of ~200 years. The purpose of this study was to refine paleoceanographic interpretations for U1313 at orbital, suborbital and millennial time scales. Species of the genus *Gephyrocapsa*, particularly small individuals of the genus, were found to dominate, with *G. margereli* serving as an indicator of cold water. In addition, the record contains important taxa that occur with lower abundances including *Umbilicosphaera sibogae* indicating warm North Atlantic Transitional Waters (NATW), and the subspecies *Coccolithus pelagicus pelagicus* which indicates cold waters. Quantitative analysis allowed Emanuele et al. (2015) to subdivide the record into changing prevailing water masses and environmental influences (Emanuele et al., 2015, fig. 3).

6.1.3 Reconstructions of August SST and SSS and sea-ice duration based on dinoflagellate cysts

Based on two modern dinoflagellate cyst datasets, the North Atlantic–Arctic oceans and the Northern Hemisphere (North Atlantic–Arctic–Pacific oceans), environmental conditions including August sea surface temperature (°C) and salinity (psu), and sea-ice duration (months/year) were reconstructed.

The reconstructed August SST based on the North Atlantic–Arctic database is approximately 3 °C lower than that based on the Northern Hemisphere database. Also, August SSS reconstructions based on the North Atlantic–Arctic database do not closely match those derived from the Northern Hemisphere database where reconstructions may be lower by up to 3 psu. These differences result from the methodology which matches

each fossil assemblage with the most similar five modern assemblages from the chosen dataset. The Northern Hemisphere database represents sites from the Mediterranean and especially from the Pacific as well as those in the North Atlantic–Arctic database. When reconstructing environmental conditions based on the Northern Hemisphere database, the software chose sites mostly located in the Pacific Ocean, which has on average lower salinity than occurs in the North Atlantic. This will have lowered the reconstructed salinity relative to that based on the North Atlantic–Arctic database. On the other hand, when reconstructing August SSTs based on the North Atlantic–Arctic database, the software was choosing sites that are mostly located in high latitudes because the distribution of sites in this database is heavily biased towards higher latitudes. This will have caused the reconstructed temperature to be lower than that based on the Northern Hemisphere database. Similarly, when reconstructing sea ice cover based on both datasets, the software was choosing sites that are mostly located in high latitudes, and the salinity based on the North Atlantic–Arctic database seems to corroborate these results. However, the salinity based on the Northern Hemisphere database seems to be higher than it should. This suggests an issue with the selectivity of the software despite the fact that the results from both datasets indicate the existence of sea ice cover not only in the same intervals but in the same samples.

In general, reconstructions based on the North Atlantic–Arctic database seem to be the more sensitive when compared with the planktonic $\delta^{18}O$ record (Ferretti et al., 2015) and alkenone paleotemperature reconstructions (Emanuele et al., 2015), presumably because the calibration set and Site U1313 are from the same region. A serious limitation even of the North Atlantic–Arctic database is that it does not contain

samples from lower latitudes including the subtropical gyre, and as already mentioned is heavily biased towards higher latitudes. The warmer intervals of the U1313 record are therefore likely to give temperature reconstructions that are too cool, and salinity reconstructions that are too low, although the cooler intervals may be expected to give reliable reconstructions. The presence and duration of sea-ice cover similarly are likely to be fairly reliably reconstructed. Finally, it should be noted that the alkenone-based paleotemperature reconstructions (Naafs et al., 2011; Emanuele et al., 2015) give mean annual paleotemperatures (Naafs et al., 2011) and cannot be compared directly with the monthly paleotemperature reconstructions based on the present study. Site U1313 today has an August SST of 22.7°C, and a mean annual SST of 18.3°C (Locarnini et al., 2013).

Taking these factors into consideration, and incorporating the paleoenvironmental reconstructions based on nannofossils and foraminiferal isotopes, a synthesis of the paleoceanography of Site U1313 is presented in the following section. It follows the dinoflagellate cyst assemblage biozones of the present study and the age model of Ferretti et al. (2015) (Figure 20).

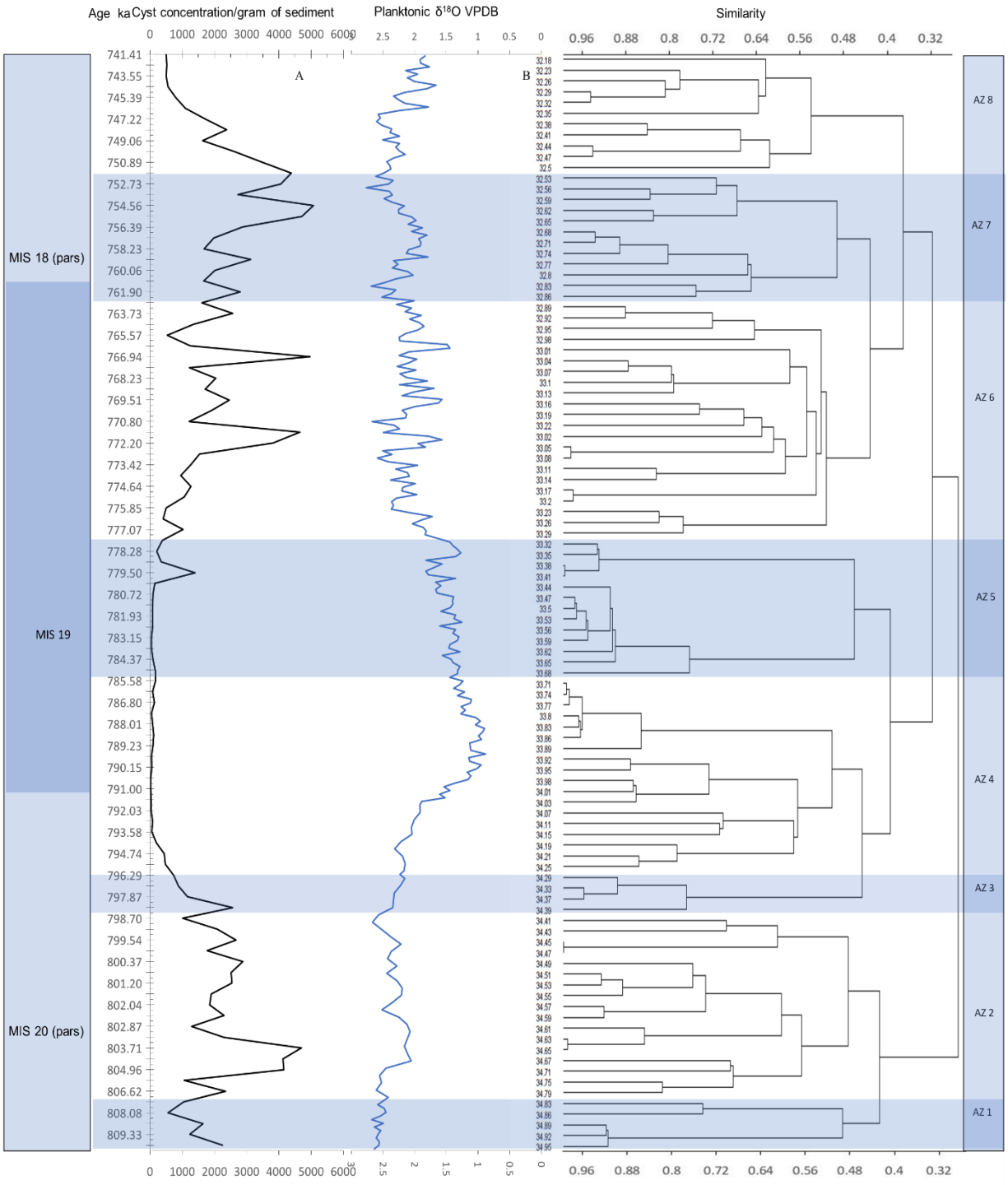

Figure 20: Constrained cluster analysis with dinoflagellate cyst assemblage biozones (this study). A) Dinoflagellate cyst concentrations. B) Planktonic oxygen isotope data (Ferretti et al., 2015). Marine Isotope Stages 18, 19, and 20 are shown. AZ = Assemblage biozones (1–8). The age model of Ferretti et al. (2015) is used.

1. Assemblage biozone 1 (34.95–34.83 mbsf; 809.96–807.46 ka)

This interval represents the heaviest planktonic foraminiferal isotope values of MIS 20, suggesting that the subpolar front was at its most southerly extent, with meltwater from icebergs reducing the salinity at Site U1313. Dominance of *N. labyrinthus*, a sub-polar species in the North Atlantic (Hennissen et al., 2017), and low numbers of *O. centrocarpum* (our NAC indicator) and protoperidiniacean cysts (our productivity indicator), along with moderate cyst concentrations, all corroborate the notion that subarctic water masses were occupying Site U1313 at this time. However, by 808 ka, near the top of biozone 1, conditions had already begun to ameliorate as indicated by a reduction in the abundance of *N. labyrinthus* to 22% and a slight but perceptible increase in lighter planktonic foraminiferal $\delta^{18}O$ values. There is no nannofossil record for this biozone.

2. Assemblage biozone 2 (34.79–34.41 mbsf; 806.62–798.72 ka)

This biozone reflects a lightening of planktonic foraminiferal $\delta^{18}O$ values, elevated cyst concentrations, a drop in the abundance of *N. labyrinthus* to around 10% and an increase in protoperidiniacean cysts to between ~40 and 72%, all indicating an amelioration of the climate and a shift of subarctic water masses northwards away from Site U1313. This warming peaked at ~805–804 ka, judging by lighter isotopic values, and is characterized by peaks in cyst concentrations and protoperidiniacean cysts that suggest increases in productivity. From ~804 ka to the top of biozone 2, a return to somewhat heavier isotopes is accompanied by moderate cyst concentrations, moderate to high protoperidiniacean cysts, and low but rising *N. labyrinthus* values especially

towards the top of the zone, that all reflect a return to subpolar waters especially from ~799 ka. Heavy planktonic $\delta^{18}O$ values can indicated melting sea-ice (Ravello and Hillaire-Marcel, 2007) and nannofossil assemblage data together with alkenone-based SSTs suggest warmer episodes influenced by iceberg melting (~803–801.5 ka, ~797–795 ka) alternating with cooler intervals of anticyclonic eddy activity (~801.5–797 ka, ~795–793 ka) (Emanuele et al., 2015). These oscillations are not clearly indicated in the dinoflagellate cyst record, perhaps in part because of the lower sampling resolution. More significantly, the sharp increase in *N. labyrinthus* near the top of the zone, which is interpreted to mark a brief return to subpolar waters, is not seen in the alkenone or nannofossil records.

August SST dinocyst reconstructions using the North Atlantic–Arctic Ocean database fluctuate between ~6° and 12°C through biozone 2, with an assemblage at 800 ka registering the lowest August temperature for the entire record. Therefore, August SST reconstructions based on dinocysts depict a cooling trend relative to biozone 1 that does not match other reconstructions particularly well. Nonetheless, several peaks of 3-month-duration ice cover are reconstructed for biozone 2 that appear broadly consistent with the interpretation of iceberg-melting waters by Emanuele et al. (2015), although the highest peak, at 800 ka, actually coincides with a cool interval of anticyclonic eddy activity.

3. Assemblage biozone 3 (34.39–34.29 mbsf; 798.28–796.28 ka)

This biozone is comparable to biozone 1 in its dominance of *N. labyrinthus* (continuing from the top of biozone 2) and decline in protoperidiniacean cysts, implying a southward shift of the subpolar front and corresponding brief return of subpolar waters to Site U1313. This seems to have lasted not more than a few thousand years because *N. labyrinthus*

values decline through biozone 3 whereas *O. centrocarpum* increases upwards (7–34%) through this zone. The short-lived return to dominance of *N. labyrinthus* between ~800 and 797 ka coincides with a peak of heavy planktonic $\delta^{18}O$ values that appears to be the culmination of a Younger Dryas-like cooling event immediately preceding Termination IX. Although it is not recorded in the benthic isotopic record, an oceanographic shift is clearly documented by dinocyst indicator species. It has been noted above that the alkenone and nannofossil records do not record this event, and it is not recorded in reconstructions based on dinocyst transfer functions.

By about 797 ka, towards the top of biozone 3, the decline in *N. labyrinthus* and increase in *O. centrocarpum* (to 34%) marks the northward shift of the subpolar front, and a maximum influence of the NAC.

4. Assemblage biozone 4 (34.25–33.71 mbsf; 795.51–785.58 ka)

At 795.51 ka, a gradual lightening of planktonic foraminiferal $\delta^{18}O$ values, and a major drop in both cyst concentrations and the abundance of *N. labyrinthus* along with the absence of protoperidiniacean cysts, all indicate an enhancement of the climate and a shift of subarctic water masses northwards away from Site U1313. In addition, there is a drop in the relative abundance of *O*. *centrocarpum* (0–19%) towards the top of this zone. This shift reflects an expansion of the subtropical gyre, which pushed the NAC north of Site U1313 with the onset of interglacial conditions. The arrival of warm subtropical gyre waters to Site U1313 at 793.58 ka is marked by the sudden increase in total *Impagidinium* species with their highest relative abundance through the entire studied interval of 31–88%, led by *I. aculeatum* and *I. patulum*. This expansion allowed subtropical gyre conditions to progressively influence the site until it was fully covered by

subtropical gyre waters. However, this expansion was interrupted by what seems to be a cooler interval of 1550 years from 793.57 to 792.02 ka, characterized by a drop in *Impagidinium* species from 70 to 39% and simultaneous rise in *N. labyrinthus* from 13.8 to 39.2%. This interruption is recorded by relatively heavy values in the planktonic foraminiferal $\delta^{18}O$ record, although cyst concentrations remain low with a gradual decline.

In contrast, it was suggested by Emanuele et al. (2015) that the NAC reached Site U1313 at 793–792 ka, as seen by an increase in the warm nannofossil species *U. sibogae* and lowest abundance or disappearance of the cold species *C. pelagicus pelagicus* and *G. margereli,* although the relative abundance of *O. centrocarpum* (our NAC indicator) is only 2.48% at 792.80 ka, having previously been 35.82% at 796.28 ka. The dinoflagellate cyst signal for the NAC therefore leads that of the nannofossil record by 3.48 kyr, implying that different water-mass properties are in fact being recorded by these two proxies. When comparing the benthic $\delta^{18}O$ curve (Fig 22C) against declining dinoflagellate cyst concentrations (Fig 22B) for this zone, there is a delay in the attainment of lightest values at ~3.57 kyr relative to the onset of the lowest cyst concentrations, the nutrient-enhanced NAC now fully deflected northwards and away from U1313. Comparing the planktonic $\delta^{18}O$ curve (Fig 22D) against the dinocyst record gives a precise reconstruction of environmental change across the glacial–interglacial transition. The rise to lightest values is abrupt, being steepest at 790.5 ka. It is at this point that *N. labyrinthus* declines to among its lowest levels and total *Impagidinium* species reach their highest abundances, while protoperidiniacean cysts, *O. centrocarpum* and cyst concentrations all remain very low. This continues through biozone 4 and is interpreted to mark, at 790.5 ka, the arrival of oligotrophic waters of the now fully expanded subtropical gyre. The peak of light

planktonic $\delta^{18}O$ values ends at ~787 ka, before the end of biozone 4, but the main dinocyst indicator taxa show no change, nor is change reflected in the nannofossil record (Emanuele et al., 2015). The reconstruction of Emanuele et al. (2015), based on the nannofossil and alkenone records, differs from the interpretation based on dinocysts in that North Atlantic Transitional Waters (rather than subtropical gyre waters) are interpreted as occupying Site U1313 from ~788 ka. Nonetheless, there is broad agreement and synchrony between the nannofossil, dinocyst and planktonic $\delta^{18}O$ values, in marking the onset of peak interglacial conditions at ~790.5 ka. This late onset relative to the benthic $\delta^{18}O$ signal, which has a midpoint age for Termination IX at ~793 ka, presumably relates to the persistence of ice sheets and ice melting to the north, and indeed Emanuele et al. (2015) proposed the persistence of iceberg melting waters at Site U1313 until as late as 793 ka.

Although the drop in protoperidiniacean cysts along with the drop in productivity during peak interglacial conditions can potentially be related to oxidising bottom waters that reduce the preservation of these cysts, in this study during the onset of interglacial conditions, the relative abundance of protoperidiniacean cysts drops sharply indicating a shift of the water mass that was covering Site U1313. Moreover, the protoperidiniacean cysts appear to be well preserved even when the concentrations are low, supporting the contention that reduced productivity rather than reduced preservation is reflected in the signal.

August SST dinocyst reconstructions for peak interglacial conditions between ~790.5 and 784 ka are ~ 20°C for the Northern Hemisphere database and ~17°C for the North Atlantic–Arctic Ocean database, compared with a present August SST of 22.7°C at

Site U1313. The Northern Hemisphere database is more appropriate for these warmer temperatures. Alkenone reconstructions for this interval give a mean annual SST varying between 16° and 17.5°C (Naafs et al., 2011; Emanuele et al., 2015), compared to a present day value of 18.3°C. Taking these reconstructions together, SSTs during peak interglacial conditions were a few degrees cooler at Site U1313 than they are today.

5. Assemblage biozone 5 (33.68–33.32 mbsf; 784.97–777.70 ka)

This biozone includes the termination of peak interglacial conditions at 784 ka, as indicated by an abrupt decline in total *Impagidinium* spp. and corresponding rise in *O. centrocarpum*. This is interpreted to mark the encroachment of North Atlantic Transitional Waters and NAC as the subtropical gyre began to contract. The NAC appears to have fully covered Site U1313 by 779.95 ka judging from a 54% abundance peak of *O. centrocarpum*. Although benthic and planktonic $\delta^{18}O$ (Ferretti et al., 2015) show only a slight steady increase, the steady drop in *Impagidinium* spp. relative abundance towards the top of this biozone from 81% to 23% indicates the progressive southwards move of subtropical waters away from Site U1313. After 779.95 ka, *O. centrocarpum* declines, but *N. labyrinthus* increases from 1% to 32% towards the top of this zone. At the same time, cyst concentrations increase from below 100 to 1400 cysts/g, indicating an increase in productivity. These changes are interpreted to reflect the southward retreat of the NAC and its replacement at Site U1313 by subpolar waters. The nannofossil and alkenone paleotemperature reconstructions of Emanuele et al. (2015) show similar trends to those revealed by dinocyst analysis. The warm-water species *U. sibogae* continues to increase in this zone until ~782 ka when it shows a slight decrease from ~779 ka to the overlying biozone. A noticeable rise in the abundance of *G. margereli* indicates temperate to cold

conditions at Site U1313 during this time. In particular, the interval ~780 to ~778 ka is interpreted to represent the presence of subpolar waters at Site U1313 (Emanuele et al., 2015). This mirrors the interpretation based on the dinocyst record, except that the timing is somewhat later, occurring between 779 and 777 ka, based on the peak abundance of *N. labyrinthus*, and hence extending into the base of biozone 6.

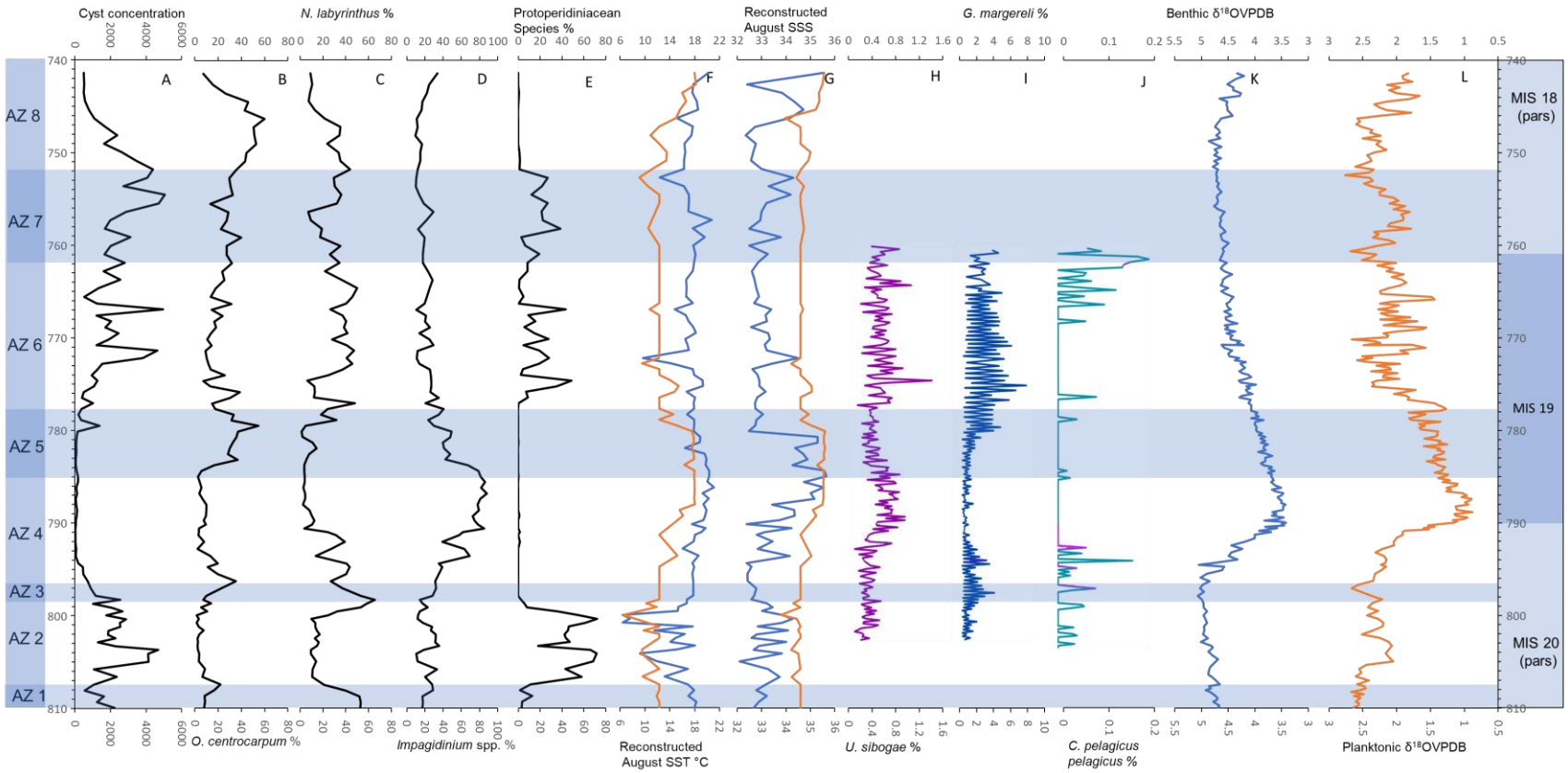

Figure 21: Palynological (A–G) along with oxygen isotope (K, L) and nannofossil (H–J) data for Site U1313. A) Dinoflagellate cyst concentrations. B) The North Atlantic Current indicator *Operculodinium centrocarpum* sensu Wall & Dale. C) Subpolar water indicator *Nematosphaeropsis labyrinthus*. D) Total *Impagidinium* spp. E) Total protoperidiniacean species. F) Reconstructed August sea surface temperature (this study). G) Reconstructed August sea surface salinity (this study). H) *Umbilicosphaera sibogae*. I) *Gephyrocapsa margereli*. J) *Coccolithus pelagicus pelagicus*. K) Benthic $\delta^{18}O$ VPDB. L) Planktonic $\delta^{18}O$ VPDB. Marine Isotope Stages 18, 19, and 20 are shown. AZ = Assemblage biozones (1–8). The nannofossil record is from Emanuelle et al. (2015). Planktonic $\delta^{18}O$ VPDB and benthic $\delta^{18}O$ VPDB data supplied by P. Ferretti (upon which Ferretti et al., 2015 is based). The age model of Ferretti et al. (2015) is used.

6. Assemblage biozone 6 (33.29–32.89 mbsf; 777.07–762.82 ka)

This biozone is characterised by complex oscillations of heavy and light planktonic foraminiferal isotope values indicating cooling excursions starting at 776.30 ka and caused by the arrival of cold water from melting icebergs released from unstable Northern Hemisphere ice sheets (Emanuele et al., 2015). This led from 776.46 ka to an increase in cooler-water dinocyst species including protoperidiniaceans with abundances reaching 49% and led by *P. stellatum* comprising up to 24%. In detail, reconstructions based on alkenone paleotemperatures and nannofossil assemblages show the dominance of cool North Atlantic transitional waters from ~778 to ~769 ka, and from ~769 ka to the top of the biozone, fluctuating conditions between subpolar waters, warmer waters associated with anticyclonic eddies, and warmer waters of the NAC, with NAC and subpolar waters alternating between 766 ka and the top of biozone 6 (Emanuele et al., 2015). The dinocyst record reflects an expansion of the subpolar gyre which continues from biozone 5, and at 766.30 ka the NAC has reduced influence at the site, judging from the sharp decline in protoperidiniacean species. Subpolar waters had occupied the site by 765 ka, based on high abundances (reaching 50%) of the subpolar species *N. labyrinthus*, although moderate values of *O. centrocarpum* exceeding 20% in the upper part of the biozone along with moderate cyst concentrations reveal relatively nutrient rich waters. The nannofossil record of Emanuele et al. (2015) at 767 ka shows an increase in *C. pelagicus pelagicus* abundance that also indicates the influence of cold nutrient-rich waters from the subpolar gyre.

7. Assemblage biozone 7 (32.86–32.53 mbsf; 761.90–751.80 ka)

The MIS 19–18 boundary, at ~761 ka (Emanuele et al., 2015), occurs near the base of this biozone. At the start of this biozone, at 761.90, Site U1313 continues to be occupied by the subpolar gyre, and the influence of cold nutrient-rich waters can be seen in the increase of protoperidiniacean species to 40% led by *P. stellatum* with a relative abundance reaching 31% and *Brigantedinium* spp. with a relative abundance reaching 27%. The southward shift of the subpolar gyre can be seen by the increase of species associated with cooler waters, led by important slight increases in *S. elongatus* with abundances of 0–9% and the highest occurrence of *B. tepikiense,* with abundances of 0–9%. The influence of subpolar gyre waters can be seen in the nannofossil record that shows an increase of cold species *G. margereli* at 760.98 ka (Emanuele et al., 2015) and heavy planktonic $\delta^{18}O$ values at 760.67 ka (Ferretti et al., 2015), although the nannofossil record ends at 759 ka.

8. Assemblage biozone 8 (32.5–32.18 mbsf; 750.89–741.41 ka)

This biozone reflects a lightening of planktonic $\delta^{18}O$ values starting at 750.89 ka, suggesting a weakening of the subpolar gyre influence at Site U1313, and starting at 747.22 ka a stronger impact of the NAC on this site. The sudden drop in protoperidiniacean species, and the drop in all species associated with cooler waters including, *B. tepikiense* (0–2.5%), *I. pallidum* (0–1%), *S. elongatus* (0–1.65%) and *N. labyrinthus* (7–35%), support the suggestion of a weakened influence of cold subpolar gyre waters on Site U1313 starting at 750.89 ka. Moreover, the increased abundance of *O. centrocarpum* from 7.6 to 35.4% provides evidence for an increased influence of the NAC at this site. In addition, starting at 745.38 ka, a sudden increase in *S. mirabilis and*

S. hyperacanthus with abundances of 0.33–38% towards the top of this biozone, to become among the most dominant species, indicates warm waters and elevated nutrients at Site U1313 at this time.

August SST dinocyst transfer functions show a warming trend through biozone 8, with the Northern Hemisphere database giving a reconstructed temperature of 20 °C for the highest sample.

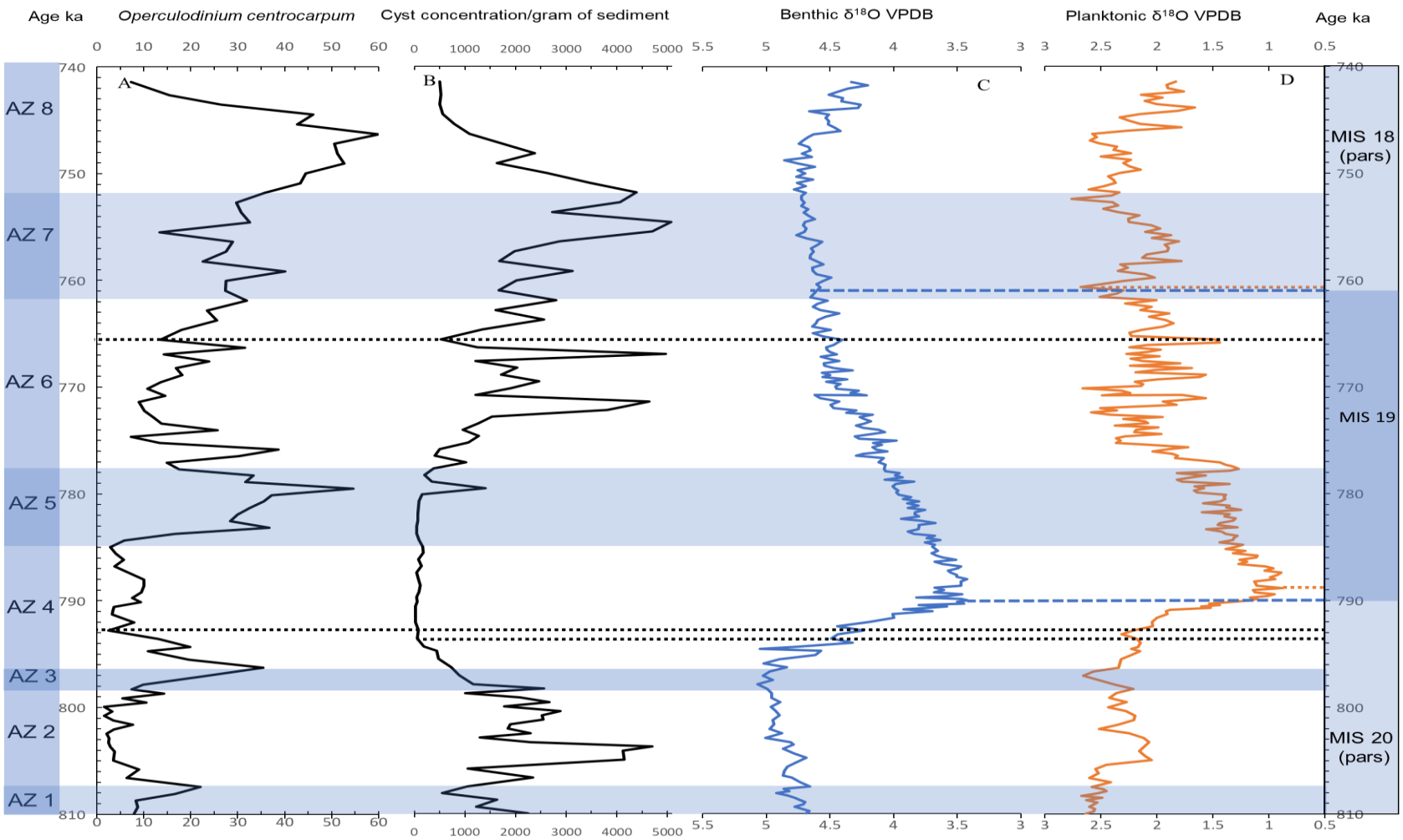

Figure 22: *O. centrocarpum* curve (A) along with dinoflagellate cysts concentrations (B) against benthic δ^{18}O VPDB (C) Planktonic δ^{18}O VPDB (D) curves. Shaded area is MIS 19 arrows indicates interval of the different response between curves. Planktonic δ^{18}O VPDB and Benthic δ^{18}O VPDB Data supplied by P. Ferretti (upon which Ferretti et al., 2015 is based). Marine Isotope Stages 18, 19, and 20 are shown. BZ = Assemblage biozones (1–8).

Chapter 7 – Summary and Conclusions

Palynological analysis of 102 samples from IODP Site U1313 in the central North Atlantic Ocean, ~386 km northwest of the Azores, spanning the interval 809.957–741.414 ka (upper MIS 20–lower MIS 18) on the astronomical time scale of Ferrietti et al. (2015), has allowed the construction of the most detailed record yet available for dinoflagellate cysts through MIS 19, with an average sample spacing of 3 cm and representing 672 years on average between samples. The samples are subsets of those used for an even higher-resolution study of the foraminiferal isotopes (planktonic and benthic) for this site by Ferretti et al. (2015), and from the same core is a high-resolution paleoceanographic reconstruction of MIS 19 based on nannofossil and alkenone paleotemperature records. The present study therefore exists within a well-constrained and detailed framework.

All samples were found to be productive and the cysts moderately to well preserved, with concentrations varying between 18.3 and 5074 cysts per gram dry weight (based on a filtrate from which the >63 µm fraction had been removed). Taxonomic richness for each sample varied between 6 and 21 taxa. Dinoflagellate cysts assemblage data were analysed statistically using various methods.

Constrained cluster analysis, using the presence or absence of species, allowed subdivision into eight assemblage biozones, although the biozone boundaries do not coincide particularly well with paleoenvironmental changes registered by other proxies or with changes interpreted using dinocyst indicator species. This is probably a consequence of a method that does not incorporate relative abundance data.

The Modern Analogue Technique (MAT) was used to generate February and August sea-surface temperatures (SSTF, SSTA) and February and August sea-surface salinities (SSSF, SSSA), and sea-ice cover (ice mean, months/year), using separately the Northern Hemisphere (*n*=1207 sites; de Vernal et al. 2013a, b) and North Atlantic–Arctic Ocean (*n*=677 sites; de Vernal et al. 2001) modern databases. These reconstructions appear less reliable in detail than interpretations based on the abundances of key indicator dinocyst species and of cyst concentrations. However, the reconstructed August SSTs and duration of sea-ice cover provide useful numerical estimates.

Among the taxa found to be most useful for paleoenvironmental reconstructions at Site U1313 are *O. centrocarpum* sensu Wall and Dale (1966) and *N. labyrinthus*. *Operculodinium centrocarpum* sensu Wall and Dale is a cosmopolitan extant species that, in the context of the North Atlantic, seems to thrive in the NAC owing to the slightly elevated nutrient levels found there. *Nematosphaeropsis labyrinthus* is a sub-polar species in the North Atlantic (Hennissen et al., 2017) and seems to serve as a good indicator of the presence of subarctic water masses at Site U1313. Protoperidiniacean cyst relative abundance serves as a productivity indicator (notwithstanding their enhanced susceptibility to oxidation on the ocean flloor) along with total cyst concentrations.

Our record begins with the heaviest planktonic foraminiferal isotope values of MIS 20, and the dominance of *N. labyrinthus* and low numbers of *O. centrocarpum* support the interpretation that subarctic water masses were occupying Site U1313 until 808 ka when conditions began to ameliorate. By ~806 ka, a drop in the abundance of *N.*

labyrinthus and an increase in protoperidiniacean cysts indicate an amelioration of the climate and a shift of subarctic water masses northwards away from Site U1313. This warming peaked at ~805–804 ka, judging by lighter isotopic values, and is characterized by peaks in cyst concentrations and protoperidiniacean cysts that suggest increases in productivity. From ~800 ka, rising *N. labyrinthus* values reflect a return to subpolar waters. August SST dinocyst reconstructions for this time are a little above 6°C, and represent the lowest temperatures in our studied interval. This cooling event was short-lived, occurring between ~800 and 797 ka, and coincides with a peak of heavy planktonic $\delta^{18}O$ values. It appears to be the culmination of a Younger Dryas-like cooling event immediately preceding Termination IX. This event has not been recognized at Site U1313 previously, although has been documented in numerous parts of the world including northern North Atlantic IODP Site U1308 (Hodell et al., 2008, as MIS 20b), Montalbano Jonico in Basilicata, southern Italy (Simon et al., 2017), Lake Baikal in Russia (Prokopenko et al., 2006), and southwest Pacific ODP Site 1123 (Elderfield et al., 2012). Its presence just before Termination IX strenghtens similarities between MIS 1 and MIS 19.

By ~797 ka, a decline in *N. labyrinthus* and increase in *O. centrocarpum* coincides approximately with a lightening of planktonic $\delta^{18}O$ values and marks the northward shift of the subpolar front, and a maximum influence of the NAC. Differing from the interpretation of Emanuele et al. (2015) that the NAC did not reach Site U1313 until ~793 ka, our data suggest an early expansion of the subtropical gyre at the end of MIS 20.

Warm subtropical gyre waters encroached Site U1313 at 793.58 ka, as shown by the sudden increase in total *Impagidinium* species, especially *I. aculeatum* and *I. patulum*,

and concomitant decrease in *N. labyrinthus*. With the respect to the planktonic $\delta^{18}O$ curve, the rise to lightest values is abrupt, being steepest at 790.5 ka, whereupon *N. labyrinthus* declines to very low levels and total *Impagidinium* species reach their highest abundances, while protoperidiniacean cysts, *O. centrocarpum* and cyst concentrations all remain very low. This is interpreted to mark, at 790.5 ka, the arrival of oligotrophic waters of the now fully expanded subtropical gyre, and the onset of peak interglacial conditions. This onset is late relative to the benthic $\delta^{18}O$ signal, which has a midpoint age for Termination IX at ~793 ka, presumably reflecting the persistence of ice sheets and ice melting to the north. Peak interglacial conditions terminated at 784 ka, signaled by an abrupt decline in total *Impagidinium* spp. and corresponding rise in *O. centrocarpum* that are interpreted to mark the return of North Atlantic Transitional Waters and the NAC as the subtropical gyre began to contract. Peak interglacial conditions therefore lasted for around 6500 years. This is similar to the interval from ~789 to 782 ka, with a duration of 7000 years, representing peak expansion of the subtropical gyre (warm NATW at Site U1313) as reconstructed from the nannofossil record (Emanuele et al., 2015). The duration is, however, shorter than that based on peak reconstructed temperatures using alkenones at Site U1313 (Naafs et al., 2010; Emanuele et al., 2015), which extends from 789 to 780 ka, with a duration of 9000 years. It is also shorter than the 10.5–12.5 kyr extent of full interglacial conditions recorded in the EPICA Dome C ice core, Antarctica and from northern North Atlantic ODP Site 983 (Tzedakis et al., 2012). These longer durations of course are based on different criteria.

For this peak interglacial interval, August SST dinocyst reconstructions are ~20°C for the Northern Hemisphere database, compared with a present August SST of 22.7°C

at Site U1313. Given that alkenone reconstructions for this interval give mean annual SSTs of 16°–17.5°C (Naafs et al., 2011; Emanuele et al., 2015), compared to a present day value of 18.3°C, it is probable that SSTs during the peak interglacial conditions of MIS 19 were a few degrees cooler at Site U1313 than today.

Following the encroachment of North Atlantic Transitional Waters at 784 ka, the NAC appears to have fully covered Site U1313 by 779.95 ka based on a 54% abundance peak of *O. centrocarpum*. Thereafter, *O. centrocarpum* declines, but *N. labyrinthus* and cyst concentrations increase, reflecting the arrival of subpolar waters.

From 776.46 ka, an increase in cooler-water dinocyst species including protoperidiniaceans marks an expansion of the subpolar gyre. Subpolar waters had occupied the site by 765 ka, based on abundances of *N. labyrinthus* reaching 50%, although moderate values of *O. centrocarpum* in the upper part of the biozone along with moderate cyst concentrations reflect relatively nutrient rich waters. Across the MIS 19–18 boundary at ~761 ka, and extending to ~751 ka, Site U1313 continued to be occupied by cold nutrient-rich waters of the subpolar gyre.

Starting at 750.89 ka, a sudden drop in protoperidiniacean species and a decline in cold-water species, along with an increased abundance of *O. centrocarpum,* provides evidence for a return to influence of the NAC, and starting at 745.38 ka, a sudden increase in the abundance of *S. hyperacanthus* and *S. mirabilis* with abundances increasing to 38% towards the top of our record indicates warm waters and elevated nutrients at Site U1313 at this time. Dinocyst transfer functions using the Northern Hemisphere database give a reconstructed temperature of 20 °C for the highest sample in MIS 18.

The present study of the dinocysts at Site U1313 shows the sensitivity of this microfossil group for detailed paleoceanographic reconstruction, and demonstrates along with other studies on this core (Ferretti et al., 2010, 2015; Emanuele et al., 2015) that in spite of the pervasive effects of bioturbation on deep ocean sediments, very high resolution records (sample spacing of one or a few cm) may still be obtained.

Chapter 8– References

Bakken, K., and Dale, B., 1986, Dinoflagellate cysts in Upper Quaternary sediments from southwestern Norway and potential correlations with the oceanic record: Boreas, v.15, p. 185-190.

Berger, A., Loutre, M.-F., Tricot, C., 1993. Insolation and Earth's orbital periods. J. Geophys. Res. Atmos. 98, 10341-10362. http://dx.doi.org/10.1029/93JD00222.

Berger, W.H., and Jansen, E., 1994, Mid-Pleistocene climate shift – the Nansen connection. In: Johannessen, O.M., Overland, J.E. (Eds.), The Polar Oceans and Their Role in Shaping the Global Environment: Geophysical Monograph Series, p. 295–311.

Bonnet, S., de Vernal, A., Gersonde, R., and Lembke-Jene, L., 2012, Modern distribution of dinocysts from the North Pacific Ocean (37–64°N, 144°E–148°W) in relation to hydrographic conditions, sea-ice and productivity: Marine Micropaleontology, v. 84–85, p. 87–113, doi: 10.1016/j.marmicro.2011.11.006.

Bonnet, S., de Vernal, A., Hillaire-Marcel, C., Radi, T., Husum, K., 2010. Variability of sea-surface temperature and sea-ice cover in the Fram Strait over the last two millennia. Marine Micropaleontology 74, 59–74.

Dale, B., 1996. Dinoflagellate cyst ecology: modelling and geological applications. In: Jansonius, J., McGregor, D.C., eds. Palynology: Principles and Applications. Volume 3. Dallas (TX): AASP Foundation; p. 1249–1275.

De Schepper, S., Fischer, E., Groeneveld, J., Head, M.J., and Matthiessen, J., 2011. Deciphering the palaeoecology of Late Pliocene and Early Pleistocene dinoflagellate cysts. Palaeogeography, Palaeoclimatology, Palaeoecology, 309: 17–32.

De Schepper, S., Groeneveld, J., Naafs, B.D.A., Van Renterghem, C., Hennissen, J., Head, M.J., Louwye, S., and Fabian, K., 2013. Northern Hemisphere glaciation during the globally warm early Late Pliocene. PLoS ONE 8(12): –81508. doi:10.1371/journal.pone.0081508.

De Schepper, S., Head, M.J., Groeneveld, J. 2009. North Atlantic Current variability through marine isotope stage M2 (circa 3.3 Ma) during the mid-Pliocene. Paleoceanography, 24: DOI: 10.1029/2008PA001725.

de Vernal, A., Eynaud, F., Henry, M., Hillaire-Marcel, C., Londeix, L., Mangin, S., Matthiessen, J., Marret, F., Radi, T., Rochon, A., Solignac, S., Turon, J.L., 2005. Reconstruction of sea-surface conditions at middle to high latitudes of the Northern Hemisphere during the Last Glacial Maximum (LGM) based on dinoflagellate cyst assemblages. Quaternary Science Reviews 24, 897–924.

de Vernal, A., Henry, M., Matthiessen, J., Mudie, P.J., Rochon, A., Boessenkool, K.P., Eynaud, F., Grøsfjeld, K., Guiot, J.L., Hamel, D., Harland, R., Head, M.J., Kunz-Pirrung, M., Levac, E., Loucheur, V., Peyron, O., Pospelova, V., Radi, T., Turon, J.-L., Voronina, E., 2001. Dinoflagellate cyst assemblages as tracers of sea-surface conditions in the northern North Atlantic, Arctic and sub-Arctic seas: the new "*n* = 677" data base and its application for quantitative palaeoceanographic reconstruction. Journal of Quaternary Sciences 16, 681–698

de Vernal, A., Hillaire-Marcel, C., Rochon, A., Fréchette, B., Henry, M., Solignac, S., Bonnet, S., 2013b. Dinocyst-based reconstructions of sea ice cover concentration during the Holocene in the Arctic Ocean, the northern North Atlantic Ocean and its adjacent seas. Quat. Sci. Rev. 79, 111–121.

de Vernal, A., Rochon, A., Fréchette, B., Henry, M., Radi, T., Solignac, S., 2013a. Reconstructing past sea ice cover of the Northern hemisphere from dinocyst assemblages: status of the approach. Quat. Sci. Rev. 79, 122–134.

de Vernal, A., Rochon, A., Turon, J.-L., Matthiessen, J., 1997. Organic-walled dinoflagellate cysts: palynological tracers of sea-surface conditions in middle to high latitude marine environments. Geobios 30 (7), 905–920.

Elderfield, H., Ferretti, P., Greaves, M., Crowhurst, S., McCave, I.N., Hodell, D., Piotrowski, A.M., 2012. Evolution of ocean temperature and ice volume through the mid-Pleistocene climate transition. Science 337, 704–709.

Emanuele, D., Ferretti, P., Palumbo, E., Amore, F.O., 2015. Sea-surface dynamics and palaeoenvironmental changes in the North Atlantic Ocean (IODP Site U1313) during Marine Isotope Stage 19 inferred from coccolithophore assemblages. Palaeogeography, Palaeoclimatology, Palaeoecology 430, 104–117.

Evitt, W.R., 1984. Some techniques for preparing, manipulating and mounting dinoflagellates. Journal of Micropaleontology, 3(2): 11–18.

Expedition 306 Scientists, 2006. Site U1313. *In* Channell, J.E.T., Kanamatsu, T., Sato, T., Stein, R., Alvarez Zarikian, C.A., Malone, M.J., and the Expedition 303/306 Scientists. *Proc. IODP,* 303/ 306: College Station TX. doi:10.2204/iodp.proc.303306.112.2006

Ferretti, P., Crowhurst, S.J., Hall, M.A., Cacho, I., 2010. North Atlantic millennial-scale climate variability 910 to 790 ka and the role of the equatorial insolation forcing. Earth and Planetary Science Letters 293, 28–41.

Ferretti, P., Crowhurst, S.J., Naafs, B.D.A., Barbante, C., 2015. The Marine Isotope Stage 19 in the mid-latitude North Atlantic Ocean: astronomical signature and intra-interglacial variability. Quat. Sci. Rev. 108, 95–110. http://dx.doi.org/10.1016/j.quascirev.2014.10.024.

Fratantoni, D.M., 2001. North Atlantic surface circulation during the 1990's observed with satellite-tracked drifters. J. Geophys. Res. 106, 22067–22093. http://dx.doi.org/10.1029/2000JC000730.

Giaccio, B., Regattieri, E., Zanchetta, G., Nomade, S., Renne, P.R., Sprain, C.R., Drysdale, R.N., Tzedakis, P.C., Messina, P., Scardia, G., Sposato, A., Bassinot, F., 2015. Duration and dynamics of the best orbital analogue to the present interglacial. Geology 43, 603e606. http://dx.doi.org/10.1130/G36677.1.Golovnina, E.A.,

Hays, J.D., Imbrie, J., and Shackleton, N.J., 1976, Variations in the Earth's orbit: pacemaker of the Ice Ages: Science, v. 194, no. 4270, p. 1121–1132.

Head, M.J., Gibbard, P.L., 2005. Early–Middle Pleistocene transitions: an overview and recommendation for the defining boundary. In: Head, M.J., Gibbard, P.L (Eds.), Early Middle Pleistocene Transitions: the Land–ocean Evidence, Special Publications, 247. Geological Society, London, pp. 1–18.

Head, M.J., Gibbard, P.L., 2015a. Formal subdivision of the Quaternary System: past, present, and future. Quaternary International 383, 4–35.

Head, M.J., Gibbard, P.L., 2015b. Early–Middle Pleistocene transitions: linking terrestrial and marine realms. Quaternary International 389, 7–46.

Head, M.J., Gibbard, P.L., van Kolfschoten, T. (Eds.), 2015. The Quaternary System and its Formal Subdivision. Quaternary International, 383, pp. 1–3.

Head, M.J., Pillans, B., Farquhar, S., 2008. The Early–Middle Pleistocene Transition: characterization and proposed guide for the defining boundary. Episodes 31 (2), 255–259.

Hennissen, J.A.I., Head, M.J., De Schepper, S., and Groeneveld, J., 2014. Palynological evidence for a southward shift of the North Atlantic Current at ~2.6 Ma during the intensification of late Cenozoic Northern Hemisphere glaciation. Paleoceanography, 28, doi: 10.1002/ 2013PA002543.

Hennissen, J.A.I., Head, M.J., De Schepper, S., and Groeneveld, J., 2015. Increased seasonality during the intensification of Northern Hemisphere glaciation at the Pliocene–Pleistocene boundary ~2.6 Ma. Quaternary Science Reviews, 129: 321–332.

Hennissen, J.A.I., Head, M.J., De Schepper, S., and Groeneveld, J., 2017. Dinoflagellate cyst paleoecology during the Pliocene–Pleistocene climatic transition in the North Atlantic. Palaeogeography, Palaeoclimatology, Palaeoecology 470: 81–108

Hodell, D.A., Channell, J.E.T., Curtis, J.H., Romero, O.E., Röhl, U., 2008. Onset of "Hudson Strait" Heinrich events in the eastern North Atlantic at the end of the middle Pleistocene transition (~640 ka)? Paleoceanography 23, PA4218. http://dx.doi.org/10.1029/2008PA001591.

Huybers, P., 2007, Glacial variability over the last two million years: an extended depthderived age model, continuous obliquity pacing, and the Pleistocene progression: Quaternary Science Reviews, v. 26, no. 1–2, p. 37–55.

Imbrie, J., Boyle, E.A., Clemens, S.C., Duffy, A., Howard, W.R., Kukla, G., Kutzbach, J., Martinson, D.G., McIntyre, A., Mix, A.C., Molfino, B., Morley, J.J., Peterson, L.C., Pisias, N.G., et al., 1992, On the structure and origin of major glaciation cycles1. Linear responses to Milankovitch forcing: Paleoceanography, v. 7, no. 6, p. 701– 738.

Lisiecki, L.E., Raymo, M.E., 2005. A Pliocene-Pleistocene stack of 57 globally distributed benthic d18O records. Paleoceanography 20, PA1003. http://dx.doi.org/10.1029/2004PA001071

Locarnini, R.A., Mishonov, A.V., Antonov, J.I., Boyer, T.P., Garcia, H.E., 2006. Volume 1: Temperature. In: Levitus, S. (Ed.), World Ocean Atlas 2005. U.S. Government Printing Office, Washington, D.C., p. 182.

Locarnini, R. A., A. V. Mishonov, J. I. Antonov, T. P. Boyer, H. E. Garcia, O. K. Baranova, M. M. Zweng, C. R. Paver, J. R. Reagan, D. R. Johnson, M. Hamilton, and D. Seidov, 2013. World Ocean Atlas 2013, Volume 1: Temperature. S. Levitus, Ed., A. Mishonov Technical Ed.; NOAA Atlas NESDIS 73, 40 pp.

Mantilla Duran, F., 2013. Central North Atlantic paleoceanography during the Middle Pleistocene (ca. 726–603 ka): insights from the dinoflagellate cyst record. Unpublished MSc thesis, Brock University

Marino, M., Bertini, A., Ciaranfi, N., Aiello, G., Barra, D., Gallicchio, S., Girone, A., La Perna, R., Lirer, F., Maiorano, P., Petrosino, P., Toti, F., 2015. Paleoenvironmental and

climatostratigraphic insights for Marine Isotope Stage 19 (Pleistocene) at the Montalbano Jonico succession, South Italy. Quaternary International 383, 104–115.

Matthiessen, J., 1995. Distribution patterns of dinoflagellate cysts and other organic-walled microfossils in recent Norwegian-Greenland Sea sediments. Marine Micropaleontology 24, 307–334.

Mudie, P.J., 1992. Circum-Arctic Quaternary and Neogene marine palynofloras: paleoecology and statistical analysis. In: Head, M.J., Wrenn, J.H. (Eds.), Neogene and Quaternary Dinoflagellate Cysts and Acritarchs, pp. 347–390.

Naafs, B.D.A., Hefter, J., Acton, G., Haug, G.H., Martínez-Garcia, A., Pancost, R., Stein, R., 2012. Strengthening of North American dust sources during the late Pliocene (2.7 Ma). Earth Planet. Sci. Lett. 317–318, 8–19. http://dx.doi.org/10.1016/j.epsl.2011.11.026.

Naafs, B.D.A., Hefter, J., Ferretti, P., Stein, R., and Haug, G.H., 2011, Sea surface temperatures did not control the first occurrence of Hudson Strait Heinrich Events during MIS 16: Paleoceanography, v. 26, no. 4, p. 1–10, doi:10.1029/2011PA002135.

Naafs, B.D.A., Hefter, J., Stein, R., 2013. Millennial-scale ice rafting events and Hudson Strait Heinrich (-like) events during the late Pliocene and Pleistocene: a review. Quat. Sci. Rev. 80, 1–28. http://dx.doi.org/10.1016/j.quascirev.2013.08.014.

Naafs, B.D.A., Stein, R., Hefter, J., Khélifi, N., De Schepper, S., Haug, G.H., 2010. Late Pliocene changes in the North Atlantic Current. Earth Planet. Sci. Lett. 298, 434–442. http://dx.doi.org/10.1016/j.epsl.2010.08.023.

Naafs, Bernhard David A; Stein, Ruediger; Hefter, Jens; Khélifi, Nabil; De Schepper, Stijn; Haug, Gerald H (2010): Sea surface temperature reconstruction for IODP Site 306-U1313. PANGAEA, https://doi.org/10.1594/PANGAEA.744483,

Novichkova, E.A., Polyakova, E.I., 2007. Dinoflagellate cysts in the surface sediments of the White Sea. Oceanology 47 (5), 660–670.

Paez-Reyes, M and Head, M.J., 2013: The Cenozoic gonyaulacacean dinoflagellate genera Operculodinium Wall, 1967 and Protoceratium Bergh, 1881 and their phylogenetic relationships. Journal of Paleontology, v.87, no.5, p.786-803.

Patterson, R.T., Swindles, G.T., Roe, H.M., Kumar, A., Prokoph, A., 2011. Dinoflagellate cyst-based reconstructions of mid to late Holocene winter sea surface temperature and productivity from an anoxic fjord in the NE Pacific Ocean. Quaternary International 235, 13–25.

Pflaumann, U., et al. (2003), Glacial North Atlantic: Sea-surface conditions reconstructed by GLAMAP 2000, Paleoceanography, 18(3), 1065, doi:10.1029/2002PA000774.

Polyakova, E.I., 2004. Dinoflagellate cysts in bottom sediment of the White Sea (western Arctic). Doklady Earth Science 400, 136–139.

Price, A.M., Pospelova, V., 2011. High-resolution sediment trap study of organic-walled dinoflagellate cyst production and biogenic silica flux in Saanich Inlet (BC, Canada).Marine Micropaleontology 80, 18–43.

Prokopenko, A.A., Hinnov, L.A., Williams, D.F., Kuzmin, M.I., 2006. Orbital forcing of continental climate during the Pleistocene: a complete astronomically tuned climatic record from Lake Baikal, SE Siberia. Quaternary Science Reviews 25, 3431e3457.

Radi, T., and de Vernal, A., 2008a, Last Glacial Maximum (LGM) primary productivity in the northern North Atlantic Ocean: Canadian Journal of Earth Sciences, v. 45, p.1299-1316, doi: 10.1139/E08-059.

Radi, T., and de Vernal, A., 2008b, Dinocysts as proxy of primary productivity in mid–high latitudes of the Northern Hemisphere: Marine Micropaleontology, v. 68, p. 84–14,
doi: 10.1016/j.marmicro.2008.01.012.

Railsback, L.B., Gibbard, P.L., Head, M.J., Voarintsoa, N.R.G., Toucanne, S., 2015. An optimized scheme of lettered marine isotope substages for the last 1.0 million years, and the climatostratigraphic nature of isotope stages and substages. Quaternary Science Reviews 111, 94–106.

Reichart, G.-J., and Brinkhuis, H., 2003, Late Quaternary *Protoperidinium* cysts as indicators of paleoproductivity in the northern Arabian Sea: Marine Micropaleontology, v. 937, p. 1–13.

Rochon, A., de Vernal, A., Turon, J., Matthiessen, J., and Head, M.J., 1999, Distribution of recent dinoflagellate cysts in surface sediments from the North Atlantic Ocean and adjacent seas in relation to sea-surface parameters: AASP Contributions Series, no. 35, p. 1–152.

Simon, Q., Bourles, D.L., Bassinot, F., Nomade, S., Marino, M., Ciaranfi, N., Girone, A., Maiorano, P., Thouveny, N., Choy, S., Dewilde, F., Scao, V., Isguder, G., Blamart, D., 2016. Authigenic $^{10}Be/^{9}Be$ ratio signature of the Matuyama–Brunhes boundary in the Montalbano Jonico marine succession. Earth Plan. Sci. Lett. 460, 255-267. http://dx.doi.org/10.1016/j.epsl.2016.11.052.

Solignac, S., Grosfjeld, K., Giraudeau, J., de Vernal, A., 2009. Distribution of recent dinocyst assemblages in the western Barents Sea. Norwegian Journal of Geology 89, 109–119.

Swift, J. H. (1986), The Arctic waters, in The Nordic Seas, edited by B. G. Hurdle, pp. 129–153, Springer, New York.

Tzedakis, P.C., 2010. The MIS 11eMIS 1 analogy, southern European vegetation atmospheric methane and the early anthropogenic hypothesis. Climate of the Past 6, 131–144.

Tzedakis, P.C., Channell, J.E.T., Hodell, D.A., Kleiven, H.F., Skinner, L.C., 2012. Determining the natural length of the current interglacial. Nat. Geosci. 5, 138–141. http://dx.doi.org/10.1038/ngeo1358.

Tzedakis, P.C., Raynaud, D., McManus, J.F., Berger, A., Brovkin, V., Kiefer, T., 2009. Interglacial diversity. Nature Geoscience 2, 751–755.

Voelker, A.H.L., Rodrigues, T., Billups, K., Oppo, D., McManus, J., Stein, R., Hefter, J., and Grimalt, J.O., 2010, Variations in mid-latitude North Atlantic surface water properties during

the mid-Brunhes (MIS 9–14) and their implications for the 98 thermohaline circulation: Climate of the Past, v. 6, no. 4, p. 531–552, http://dx.doi:10.5194/cp-6-531-2010.

Wright, A.K., and Flower, B.P., 2002, Surface and deep ocean circulation in the subpolar North Atlantic during the mid-Pleistocene revolution: Paleoceanography, v. 17, no. 4, p. 1–16, doi: 10.1029/2002PA000782.

Zonneveld, K.A.F., Marret, F., Versteegh, G.J.M., Bogus, K., Bonnet, S., Bouimetarhan, I., Crouch, E., de Vernal, A., Elshanawany, R., Edwards, L., Esper, O., Forke, S., Grøsfjeld, K., Henry, M., Holzwarth, U., Kielt, J.-F., So-Young, K., Ladouceur, S., Ledu, D., Chen, L., Limoges, A., Londeix, L., Lu, S.-H., Mahmoud, M.S., Marino, G., Matsouka[sic], K., Matthiessen, J., Mildenhal[sic], D.C., Mudie, P., Neil, H.L.,99 Pospelova, V., Qi, Y., Radi, T., Richerol, T., Rochon, A., Sangiorgi, F., Solignac, S.,Turon, J.-L., Verleye, T., Wang, Y., Wang, Z., and Young, M., 2013, Atlas of modern dinoflagellate cyst distribution based on 2405 datapoints: Review of Paleobotany and Palynology, v. 191, p. 1–197

Zonneveld, K.A.F., Susek, E., and Fischer, G., 2010, Seasonal variability of the organic-walled dinoflagellate cyst production in the coastal upwelling region off Cape Blanc (Mauritania): a five-year survey: Journal of Phycology, v. 46, p. 202–215.

Zweng, M.M, J.R. Reagan, J.I. Antonov, R.A. Locarnini, A.V. Mishonov, T.P. Boyer, H.E. Garcia, O.K. Baranova, D.R. Johnson, D.Seidov, M.M. Biddle, 2013. World Ocean Atlas 2013, Volume 2: Salinity. S. Levitus, Ed., A. Mishonov Technical Ed.; NOAA Atlas NESDIS 74, 39 pp.

APPENDIX 1: Plates

All illustrated specimens are from the present study, IODP Site U1313. Abbreviations are as follows: UF = upper focus, MF = mid-focus, LF = lower focus, EF = England Finder reference, max. dia. = maximum diameter.

Plate1

1–3: *Brigantedinium* spp. 1: LF, dorsal view; dia. 38 µm; Sample 7, slide 1, EF: H56/0. 2: LF, ventral view showing operculum adhering to the cyst; Sample 12, slide 1, EF: R52/0, dia. 42 µm. 3: MF, ventral view, dia. 42 µm; Sample 12, slide 1 (802.9 ka). EF: W48/0.

4–6: *Bitectatodinium tepikiense*. 4: LF, ventral view showing archeopyle formed by loss of two precingular plates, 3'' and 4''. 5: MF, dia. 50x48 µm, 6: HF, dorsal view. Sample 57, slide 57C (777.7 ka). EF: S44/3.

7–9: *Impagidinium aculeatum*. 7: LF, dorsal view, 8: MF, central body dia. 37 x 26 µm, 9: HF, ventral view. Sample 2, slide 2 (809.3 ka). EF: S55/3.

10–12: *Impagidinium cantabrigiense*. 10: HF, dorsal view, 11: MF, crest height varies from 5 µm at the apex to 10µm at the antapex, central body max. dia. 31 µm, 12: LF, ventral view. Sample 2, slide 2 (809.3 ka). EF: Q43/3.

13–15: *Impagidinium pallidum*. 13: LF, ventral view, 14: MF, dia. including crests 50 µm. 15: LF dorsal view. Sample 13, slide 1 (802.5 ka). EF: T31/0.

Plate 1

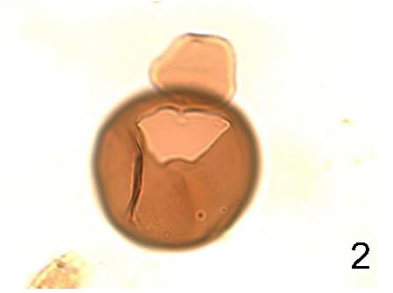

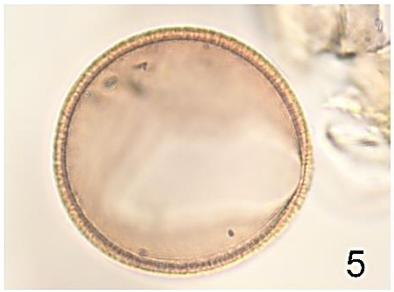

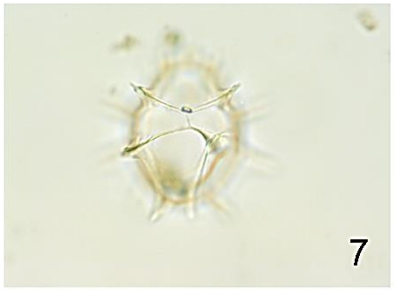

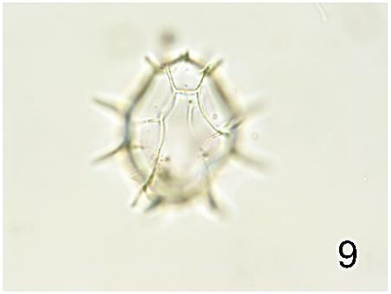

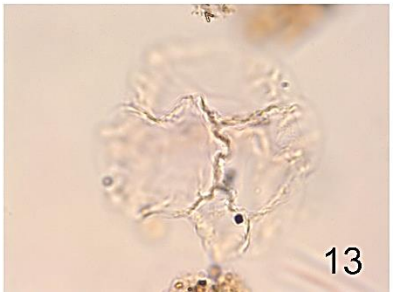

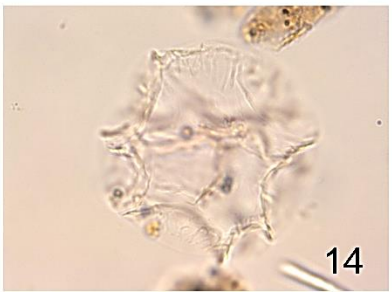

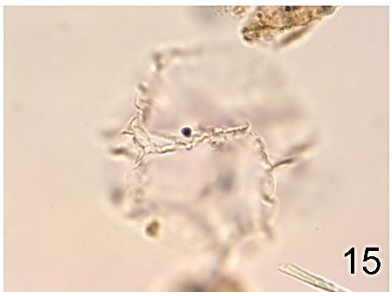

Plate 2

1–3: *Impagidinium paradoxum.* 1: LF, showing tabulation on ventral surface, 2: MF, optical cross-section, crest height 3 µm, central body dia. 29 x 23 µm, 3: HF, dorsal view. Sample 56, slide 56C (778.3 ka). EF: P60/4.

4–6: *Impagidinium patulum*. 4: LF, right lateral view, 5: MF, optical cross-section, crest height varies from 3 µm to 6 µm, central body dia. 63 x 55 µm, 6: HF, left-lateral view. Sample 30, slide 30C (793.6 ka). EF: S63/2.

7–9: *Impagidinium plicatum*. 7: MF, optical cross-section, Maximum crest height 4 µm, 8: HF, ventral-apical view, crest height: 2 µm. Central body dia. 26 x 30 µm, 9: LF dorsal-antapical view, Sample 20, slide 2 (799.54ka). EF: W40/2.

10–12: *Impagidinium sphaericum.* 10: LF, dorsal view, 11: MF, optical cross-section. Central body dia. 40 x 44 µm, 12: HF, Sample 11, slide 1 (803.3 ka). EF: K32/3.

13–15: *Impagidinium strialatum*. 13: LF, latero-dorsal view, 14: MF, optical cross-section, maximum crest height: 7 µm, Central body max. dia. 30 µm, 15: HF, latero-ventral view, Sample 78, slide 2 (763.7 ka). EF: O39/1.

Plate 2

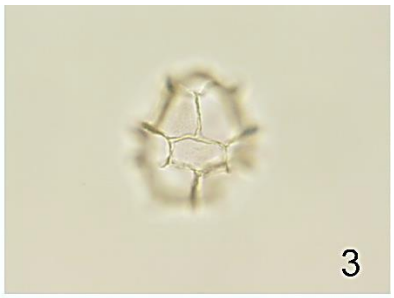

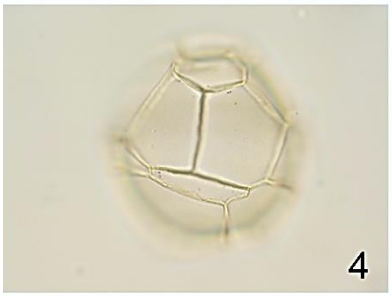

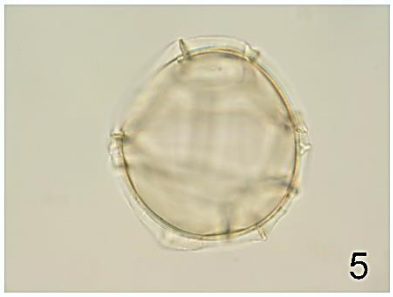

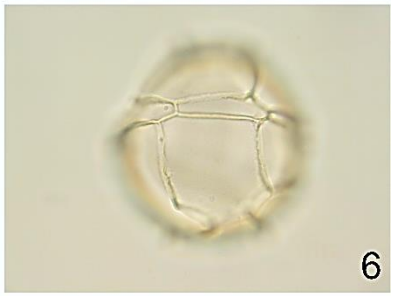

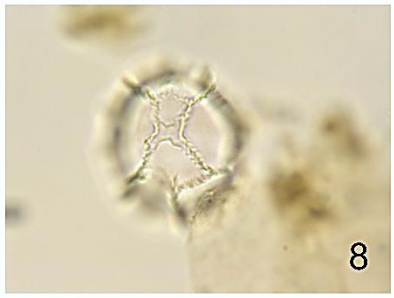

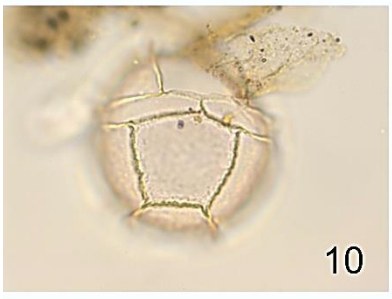

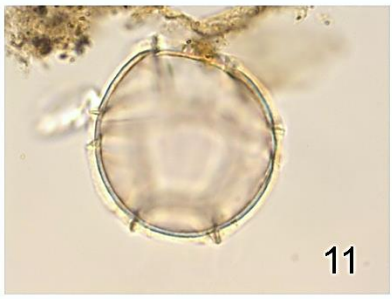

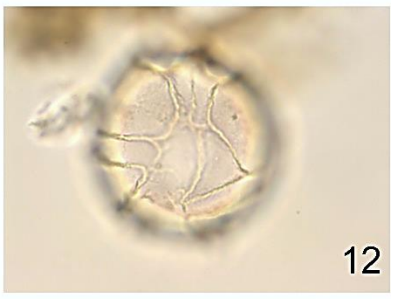

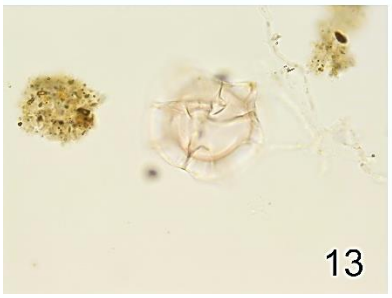

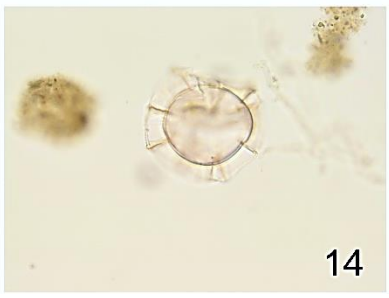

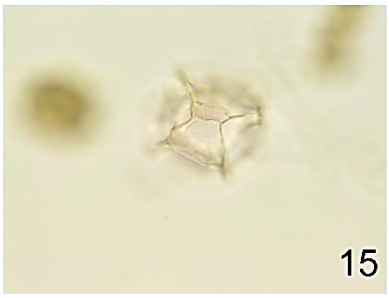

Plate 3

1–3: *Nematosphaeropsis labyrinthus.* 1: LF, lateral view, 2: MF, optical cross-section; max. Process length, 16 µm, and central body max. dia. 33 µm, 3: HF, lateral view shows processes joined together by trabeculae, Sample 98, slide 98C (745.4 ka). EF: G27/2.

4–6: *Operculodinium centrocarpum* sensu Wall and Dale, 1966. 4: LF dorsal view showing archeopyle shape, central body dia. 37µm, process length 9µm; sample 55, slide 55C (778.9ka). EF: N55/3. 5: HF, central body max. dia. 41µm, max. Process length 11µm, 6: MF, optical cross-section. Sample 1, slide 2 (810 ka). EF: U17/3.

7–9: *Protoperridinium stellatum*. 7–9: MF, dorso-ventral view showing archeopyle still attached to the cyst, central body max. dia. 60 µm. Sample 9, slide 1 (804.1ka). EF: U32/2.

10–12: *Pyxidinopsis reticulata*. 10: MF, optical cross-section, central body max. dia. 39 µm, 11: HF, archeopyle, Sample 88, slide 1 (754.56ka). EF: T30/3. 13: LF, central body max. dia. 37µm, archeopyle. Sample 17, slide 1 (800.8 ka). EF: O44/4.

13–15: "*Pyxidinopsis striatoconulus"*. 13: LF, archeopyle, 14: MF, optical cross-section, central body max. dia. 44 µm, 15: HF process length: 1.5 µm. Sample 79, slide 2 (762.8 ka). EF: R56/2.

Plate 3

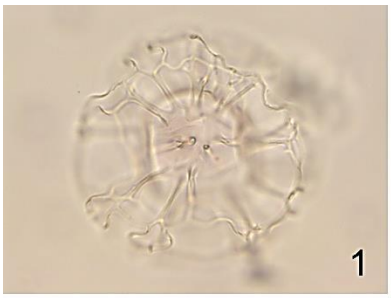

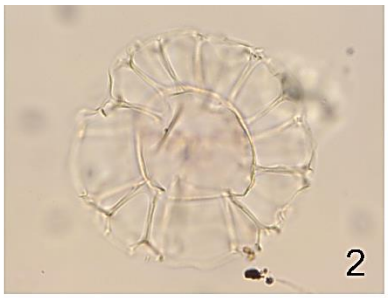

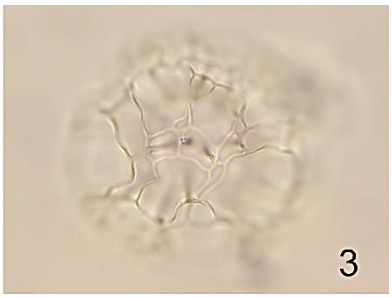

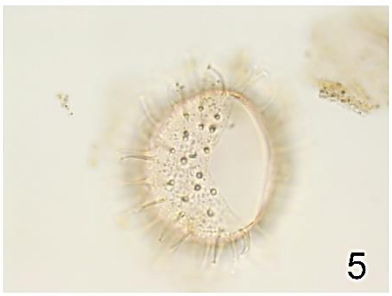

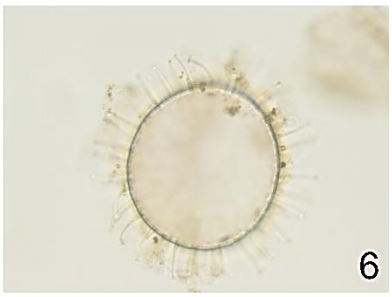

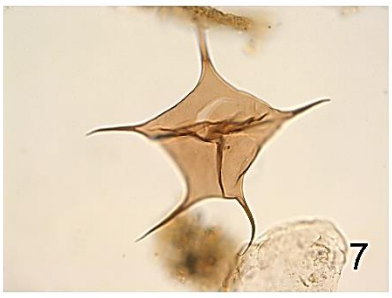

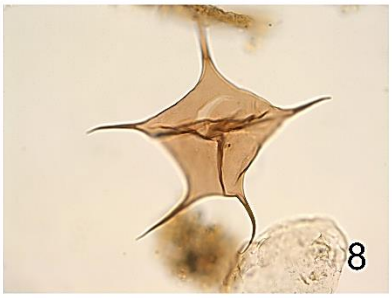

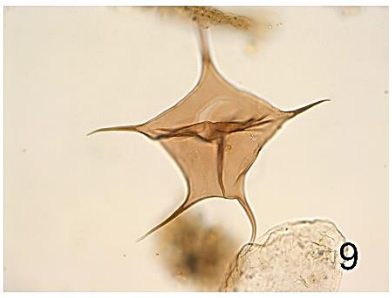

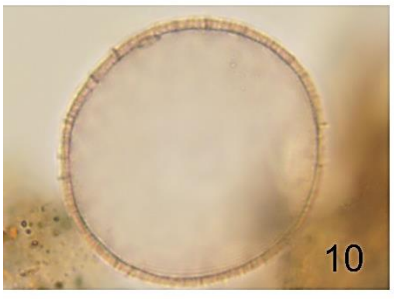

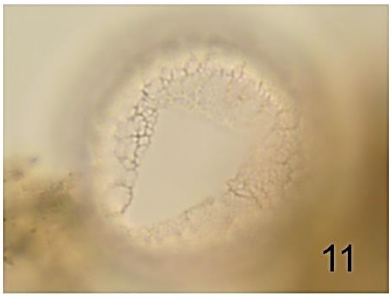

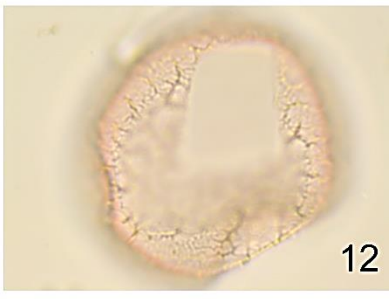

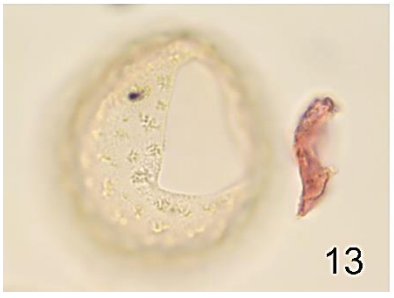

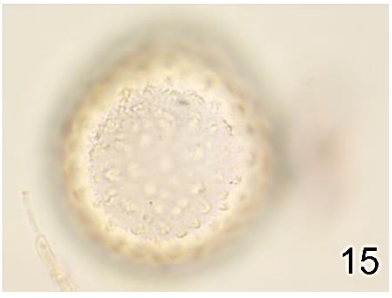

Plate 4

1–3: *Spiniferites elongatus*. 1: LF dorsal view, 2: MF, optical cross-section, max. process length: 11µm, central body length 53 µm, central body width 29 µm. 3: HF, ventral view. Sample 13, slide 1 (802.5ka). EF: K49/4.

4–6: *Spiniferites hyperacanthus*. 4: HF, latero-ventral view, 5: LF, latero-dorsal, 6: MF, optical cross-section, central body max. dia. 53 µm, max. process length 19 µm. Sample 98, slide 98C (745.4 ka). EF: M27/4.

7–10: *Spiniferites mirabilis.* 7: HF, ventral view, 8: MF, dorsal view, 9: mid focus, optical cross-section, central body max. dia. 57 µm, 10: LF, max. process length 20 µm, Sample 98, slide 98C (745.4 ka). EF: P38/1.

11, 12: *Selenopemphix nephroides*.11: latero-apical view, 12: MF, optical cross-section, central body max. dia. 70 µm, Sample 86, slide 1 (756.4 ka). EF: O55/4.

13–15: *Selenopemphix quanta*. 13, 15, MF, process length: 10 µm, 14: HF, central body max. dia. 30 µm, Sample 15, slide 1 (801.6 ka). EF: F61/2.

Plate 4

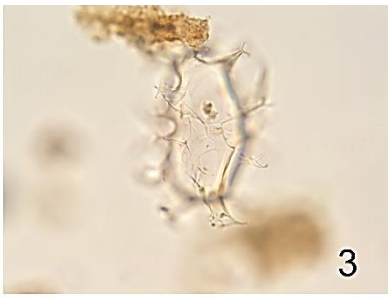

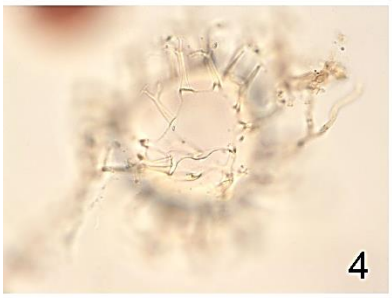

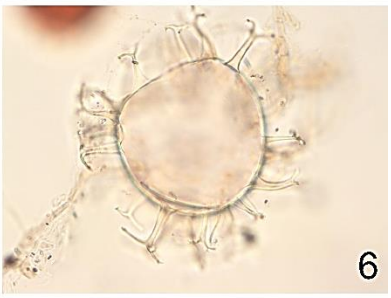

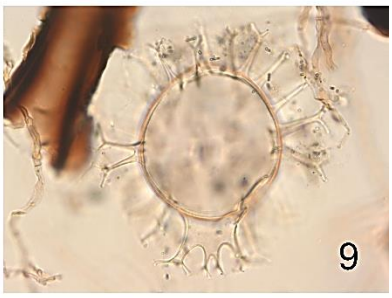

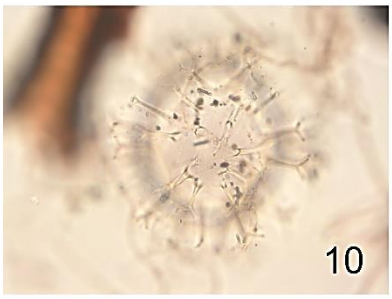

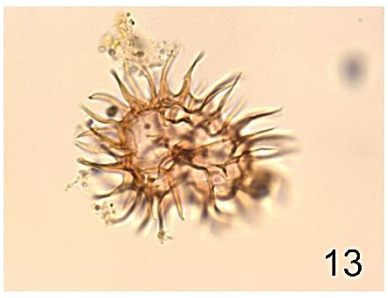

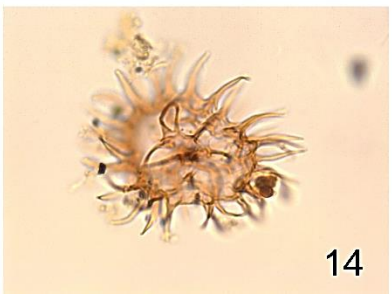

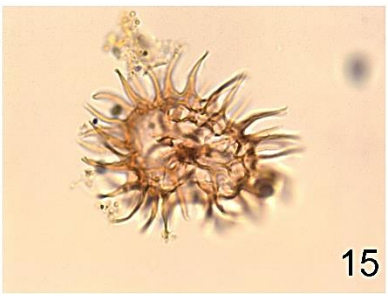

Plate 5

1–3: *Lavradosphaera* cf. *crista.* 1: LF, 2, optical cross-section, 3 MF, crest height 3 µm, central body max. dia. 16 µm, Sample 54, slide 54C (779.5 ka). EF: R56/3.

4–6: *Cymatiosphaera*? spp. 4: HF, 5: MF, optical cross-section, central body max. dia. 16 µm, 6: LF: crest height 1 µm, Sample 66, slide 1 (772.2 ka). EF: T50/4.

7–9: Acritarch sp. 1. 7: LF, 8: MF, optical cross-section, process length 2 µm, central body max. dia. 13µm, 9: HF, Sample 53, slide 1 (780.1 ka). EF: G27/2.

10, 11: Acritarch sp. 2. 10: MF, optical cross-section, process length: 12µm, 11: LF, central body max. dia. 14 µm, Sample 43, slide 2 (786.2ka). EF: P34/2.

12–15: Acritarch sp. 2. 12, 13: MF, process length 9 µm, 14: HF, central body max. dia. 13 µm, 15: LF, Sample 46, slide 2 (784.4 ka). EF: T48/0.

Plate 5

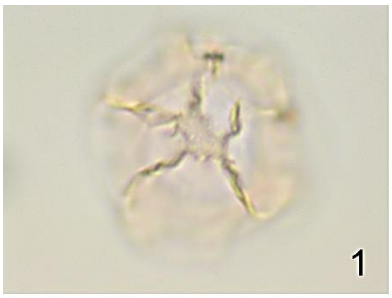

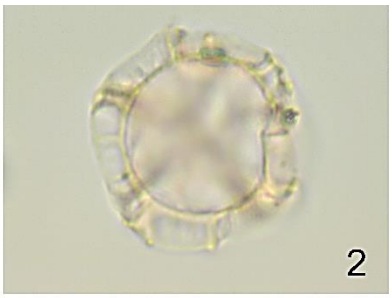

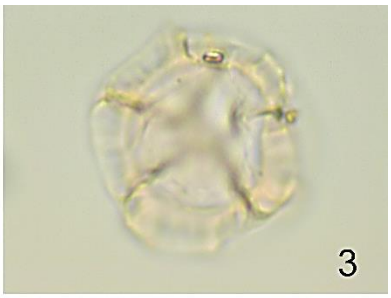

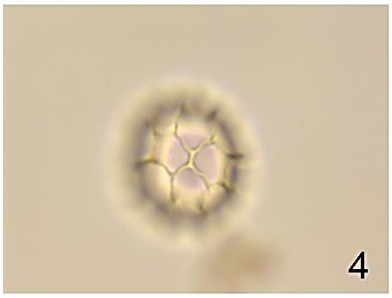

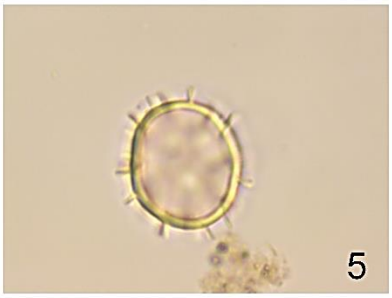

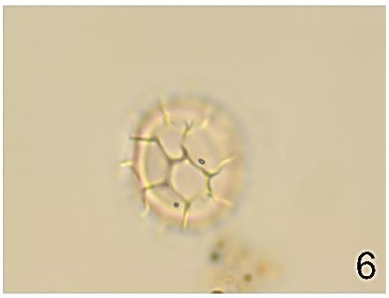

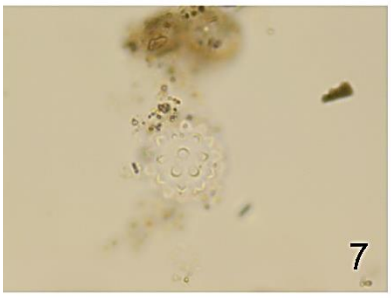

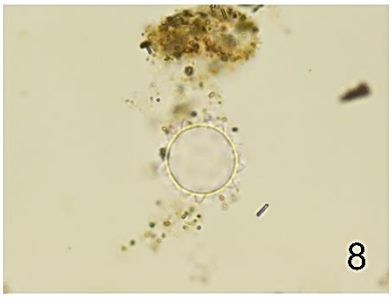

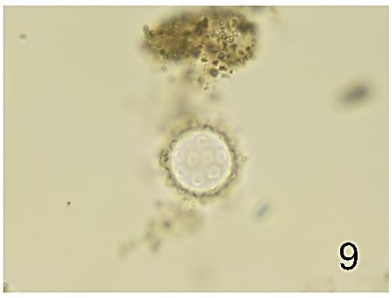

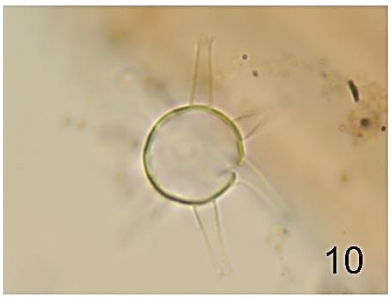

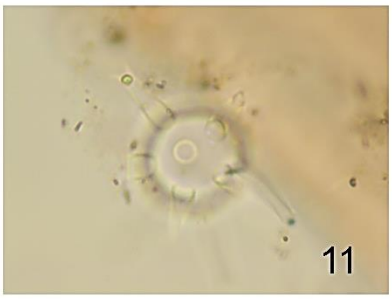

APPENDIX 2: Raw counts of the dinoflagellate cysts, acritarchs, and reworked palynomorphs.

Sample ID#	Leg	Site	Hole	Core	Type	Section	Half	Top (cm)	Bot (cm)	Depth (mbsf)	Depth (mcd)	revised mcd	Depth (amcd)	Age (ka) 22 October 2012 (Age model 20)	Sed. rates	Assemblage biozones	Marine Isotope Stage	DINOFLAGELLATE CYSTS																								
																		Achomosphaera andalousiensis	*Ataxiodinium choane??*	*Brigantedinium cariacoense*	*Brigantedinium simplex*	*Brigantedinium ???*	*Bitectatodinium tepikiense.*	*Corrudinium? labradori*	*Dalella chathamensis*	*Impagidinium aculeatum*	*Impagidinium cantabrigiense*	*Impagidinium palidum*	*Impagidinium paradoxum*	*Impagidinium patulum*	*Impagidinium plicatum*	*Impagidinium sphaericum*	*Impagidinium strialatum*	*Nematosphaeropsis labyrinthus*	*Operculodinium centrocarpum*	*Operculodinium centrocarpum short processes*	*Protoperridinium Stellatum*	*Pyxidinopsis reticulata*	*Pyxidinopsis striatoconulus*	*Spiniferites belerius*	*spiniferites coniconcavus*	*Spiniferites elongatus*	*Spiniferites hyperacanthus*
102	306	1313	A	4	H	6	W	49	50	32.2	35.9	36.3	36.3	741.4				**0**	**0**	**0**	**0**	**0**	**3**	**0**	**0**	**90**	**14**	**0**	**7**	**9**	**10**	**0**	**7**	**29**	**22**	**0**	**0**	**0**	**0**	**0**	**0**	**79**
101	306	1313	A	4	H	6	W	53	54	32.2	36	36.35	36.35	742.6				**0**	**0**	**0**	**0**	**0**	**0**	**0**	**0**	**63**	**11**	**0**	**0**	**9**	**13**	**1**	**6**	**32**	**44**	**2**	**0**	**3**	**8**	**0**	**1**	**96**
100	306	1313	A	4	H	6	W	56	57	32.3	36	36.38	36.38	743.6				**0**	**0**	**2**	**0**	**0**	**4**	**0**	**0**	**52**	**10**	**0**	**4**	**10**	**7**	**1**	**0**	**27**	**81**	**0**	**0**	**4**	**0**	**0**	**0**	**91**
99	306	1313	A	4	H	6	W	59	60	32.3	36	36.41	36.41	744.5				**0**	**0**	**1**	**0**	**0**	**2**	**0**	**0**	**39**	**12**	**0**	**3**	**5**	**11**	**6**	**1**	**23**	**140**	**0**	**0**	**3**	**2**	**0**	**0**	**48**
98	306	1313	A	4	H	6	W	62	63	32.3	36.1	36.44	36.44	745.4				**0**	**0**	**0**	**0**	**0**	**0**	**0**	**0**	**27**	**3**	**0**	**7**	**11**	**4**	**5**	**1**	**39**	**130**	**0**	**0**	**1**	**1**	**0**	**2**	**53**
97	306	1313	A	4	H	6	W	65	66	32.4	36.1	36.48	36.48	746.3	0.03546	BZ8		**0**	**0**	**0**	**0**	**0**	**5**	**2**	**0**	**19**	**2**	**0**	**5**	**9**	**0**	**2**	**1**	**68**	**186**	**5**	**0**	**0**	**2**	**0**	**0**	**4**	**7**
96	306	1313	A	4	H	6	W	68	69	32.4	36.1	36.51	36.51	747.2	0.03546			**0**	**0**	**0**	**0**	**0**	**0**	**0**	**0**	**27**	**0**	**0**	**0**	**2**	**2**	**10**	**1**	**116**	**166**	**0**	**0**	**2**	**0**	**0**	**0**	**0**	**1**
95	306	1313	A	4	H	6	W	71	72	32.4	36.2	36.54	36.54	748.1	0.03546			**0**	**0**	**0**	**0**	**0**	**0**	**0**	**0**	**18**	**3**	**1**	**0**	**5**	**2**	**7**	**1**	**108**	**159**	**0**	**0**	**2**	**1**	**0**	**0**	**1**	**2**
94	306	1313	A	4	H	6	W	74	75	32.4	36.2	36.57	36.57	749.1	0.03546			**0**	**0**	**0**	**0**	**0**	**7**	**0**	**0**	**29**	**2**	**0**	**0**	**14**	**8**	**8**	**0**	**72**	**160**	**0**	**0**	**1**	**0**	**0**	**0**	**1**	**2**
93	306	1313	A	4	H	6	W	77	78	32.5	36.2	36.61	36.61	750	0.03546			**0**	**0**		**0**	**4**	**2**	**0**	**0**	**19**	**1**	**0**	**0**	**23**	**3**	**4**	**0**	**106**	**139**	**0**	**0**	**2**	**0**	**0**	**0**	**5**	**3**
92	306	1313	A	4	H	6	W	80	81	32.5	36.3	36.64	36.64	750.9	0.03546		MIS18	**0**	**2**	**0**	**1**	**4**	**0**	**0**	**0**	**31**	**3**	**1**	**0**	**11**	**0**	**3**	**1**	**107**	**131**	**0**	**0**	**1**	**0**	**0**	**0**	**5**	**1**
91	306	1313	A	4	H	6	W	83	84	32.5	36	36.67	36.7	752	0.0355			0	0	1	0	1	1	0	0	22	4	3	1	7	6	7	2	135	110	0	0	1	0	0	0	3	1
90	306	1313	A	4	H	6	W	86	87	32.6	36	36.7	36.7	753	0.0355			0	0	26	9	43	5	0	0	16	1	0	0	6	1	10	0	90	90	0	0	1	0	0	0	0	0
89	306	1313	A	4	H	6	W	89	90	32.6	36	36.74	36.7	754	0.0355			0	0	5	0	57	3	0	0	21	10	1	5	4	4	1	0	93	94	0	1	3	0	0	0	0	0
88	306	1313	A	4	H	6	W	92	93	32.6	36	36.77	36.8	755	0.0355			0	0	2	0	30	5	0	0	29	1	0	0	10	3	5	1	116	104	0	0	1	2	0	0	0	2
87	306	1313	A	4	H	6	W	95	96	32.7	36	36.8	36.8	755	0.0355			0	0	14	14	55	3	0	0	33	5	1	0	18	2	7	0	99	41	0	0	7	1	0	0	0	5
86	306	1313	A	4	H	6	W	98	99	32.7	36	36.83	36.8	756	0.0355			2	0	20	7	27	10	0	0	33	3	0	0	34	5	21	1	22	84	3	4	6	5	0	0	0	5
85	306	1313	A	4	H	6	W	101	102	32.7	36	36.87	36.9	757	0.0355	BZ7		0	0	3	2	45	13	0	0	32	1	0	0	14	8	18	0	29	80	4	15	14	15	0	0	0	8
84	306	1313	A	4	H	6	W	104	105	32.7	36	36.9	36.9	758	0.0355			1	0	8	1	12	2	0	0	34	3	2	0	2	1	2	0	59	69	1	96	7	2	0	0	0	5
83	306	1313	A	4	H	6	W	107	108	32.8	37	36.93	36.9	759	0.0355			0	0	0	1	3	29	0	0	19	2	0	0	29	0	14	2	56	126	1	2	3	6	0	0	0	18
82	306	1313	A	4	H	6	W	110	111	32.8	37	36.96	37	760	0.0355			0	0	0	0	11	0	0	0	37	6	0	0	13	7	7	0	107	83	0	1	9	4	0	0	0	10
81	306	1313	A	4	H	6	W	113	114	32.8	37	37	37	761	0.0355			0	0	9	5	37	6	0	0	37	9	0	1	16	3	5	0	87	87	4	4	4	0	0	0	0	7
80	306	1313	A	4	H	6	W	116	117	32.9	37	37.03	37	762	0.0355			3	0	0	1	24	1	0	0	39	1	1	0	13	1	3	0	108	96	3	0	10	2	0	0	0	2
79	306	1313	A	4	H	6	W	119	120	32.9	36.6	37.06	37.06	762.8	0.03546			0	0	0	0	23	15	0	0	51	6	0	0	12	11	11	0	69	74	0	0	34	3	0	0	0	1
78	306	1313	A	4	H	6	W	122	123	32.9	36.7	37.09	37.09	763.7	0.03546			0	0	0	0	0	11	0	0	64	3	0	0	15	5	7	1	109	77	0	0	4	0	0	0	0	2
77	306	1313	A	4	H	6	W	125	126	33	36.7	37.13	37.13	764.6	0.03546			0	0	2	0	0	2	0	0	61	0	0	0	12	5	4	3	153	55	0	0	5	0	0	0	1	2
76	306	1313	A	4	H	6	W	128	129	33	36.7	37.16	37.16	765.6	0.03546			0	0	0	0	9	3	0	6	34	3	0	0	15	8	19	1	142	42	0	4	18	0	0	0	1	0
75	306	1313	A	4	H	6	W	131	132	33	36.8	37.19	37.19	766.3	0.03546			2	0	0	0	0	7	0	0	39	1	1	0	16	3	8	2	129	99	2	1	8	2	0	0	0	0
74	306	1313	A	4	H	6	W	134	135	33	36.8	37.21	37.21	766.9	0.03546			0	0	0	1	63	2	0	0	24	2	1	0	5	5	7	1	91	49	0	84	3	1	0	0	0	0
73	306	1313	A	4	H	6	W	137	138	33.1	36.8	37.23	37.23	767.6	0.03546			0	0	0	5	14	7	0	0	52	7	0	0	5	4	9	0	116	74	0	7	7	0	0	0	0	0
72	306	1313	A	4	H	6	W	140	141	33.1	36.9	37.25	37.25	768.2	0.03546			0	0	4	1	41	2	0	0	51	7	1	1	6	5	3	0	122	51	0	1	4	0	0	0	0	0
71	306	1313	A	4	H	6	W	143	144	33.1	36.9	37.28	37.28	768.9	0.03546			0	0	0	0	13	3	0	0	57	14	2	0	13	9	11	1	121	57	0	4	7	0	0	0	0	0
70	306	1313	A	4	H	6	W	146	147	33.2	36.9	37.3	37.3	769.5	0.03546			0	0	10	3	23	5	0	0	30	15	0	1	8	13	4	1	128	41	1	0	6	5	0	0	0	2
69	306	1313	A	4	H	6	W	149	150	33.2	36.9	37.32	37.32	770.2	0.03546	BZ6		0	0	3	7	51	1	0	2	20	4	0	3	27	8	26	0	85	32	1	18	2	7	0	0	0	0
68	306	1313	A	4	H	7	W	2	3	33.2	37	37.34	37.34	770.8	0.03546			0	0	0	0	2	6	0	0	58	8	0	1	20	5	11	0	126	45	0	10	8	2	0	0	0	3
67	306	1313	D	4	H	4	W	2	3	33	37.4	37.37	37.37	771.4	0.03546			0	0	0	4	53	3	0	0	22	17	1	3	8	6	3	1	141	27	0	0	7	0	0	0	0	0
66	306	1313	D	4	H	4	W	5	6	33.1	37.5	37.4	37.4	772.2	0.05412			0	0	9	4	61	3	0	0	18	11	0	3	9	8	5	3	129	32	0	6	1	4	0	0	0	0
65	306	1313	D	4	H	4	W	8	9	33.1	37.5	37.43	37.43	772.8	0.05412			0	0	6	7	24	0	0	0	35	7	0	0	6	9	3	5	146	38	0	21	2	7	0	0	0	0
64	306	1313	D	4	H	4	W	11	12	33.1	37.5	37.46	37.46	773.4	0.05412			0	0	0	0	11	6	0	0	39	11	0	0	32	10	9	2	117	41	2	0	20	5	0	0	0	1
63	306	1313	D	4	H	4	W	14	15	33.1	37.5	37.5	37.5	774	0.05412			0	0	0	0	7	15	0	0	60	18	2	2	11	16	11	1	77	81	0	0	11	2	0	0	0	1
62	306	1313	D	4	H	4	W	17	18	33.2	37.6	37.53	37.53	774.6	0.05412			0	0	15	29	103	8	0	0	38	12	1	0	35	3	8	0	19	22	0	0	4	1	0	0	0	2
61	306	1313	D	4	H	4	W	20	21	33.2	37.6	37.56	37.56	775.2	0.05412			0	0	9	9	92	5	0	0	42	9	0	0	33	8	9	0	39	42	0	0	8	0	0	0	0	5
60	306	1313	D	4	H	4	W	23	24	33.2	37.6	37.6	37.6	775.9	0.05412			0	0	0	0	22	7	0	0	50	13	0	1	15	16	15	1	40	119	1	0	6	0	0	1	0	2
59	306	1313	D	4	H	4	W	26	27	33.3	37.7	37.63	37.63	776.5	0.05412			0	0	1	2	24	13	0	0	73	5	0	6	21	7	10	2	38	93	1	0	6	4	0	4	0	0
58	306	1313	D	4	H	4	W	29	30	33.3	37.7	37.66	37.66	777.1	0.05412			0	0	0	0	1	1	0	0	45	22	0	8	3	8	7	0	145	41	4	0	12	1	3	0	0	0
57	306	1313	D	4	H	4	W	32	33	33.3	38	37.69	37.7	778	0.0541			0	0	0	0	0	6	0	0	109	14	1	9	1	9	13	1	79	53	4	0	22	0	1	1	0	1
56	306	1313	D	4	H	4	W	35	36	33.4	38	37.73	37.7	778	0.0541			0	0	0	0	0	4	0	0	56	10	1	10	17	11	24	0	56	96	5	0	5	0	1	0	1	6
55	306	1313	D	4	H	4	W	38	39	33.4	38	37.76	37.8	779	0.0541		MIS19	0	0	0	0	0	3	0	0	51	10	1	5	7	13	8	1	96	93	2	0	8	0	0	0	0	2

Continued

| | | |

Sample ID#	Leg	Site	Hole	Core	Type	Section	Half	Top (cm)	Bot (cm)	Depth (mbsf)	Depth (mcd)	revised mcd	Depth (amcd)	Age (ka) 22 October 2012 (Age model 20)	Sed. rates	Assemblage biozones	Marine Isotope Stage	DINOFLAGELLATE CYSTS				ACRITARCHS				REWORKED PALYNOMORPH										Pollen bisaccate	Foraminiferal lining	SPORS RW	POLLEN	Total dinocysts counted	Lycopodium spores	Cyst concentration/gram of sediment	sample waight
																		Spiniferites mirabilis	Spiniferites Spp	Selenopemphix nephroides	Selenopemphix quanta	Spp1	Spp 2	spp3	Lavradosphaera cf. crista	Lavradosphaera cf. crista?	Glaphyrocysta sp.	Hystrichodinium cf. pulchrum	Oligosphaeridium complex	Veryhachium spp	Micrhystridium? sp	Spinidinium sp..	Pollen bisaccate RW	SPORS RW								
102	306	1313	A	4	H	6	W	49	50	32	36	36.3	36.3	741				41	0	0	0	0	0	0	2	0	0	0	0	0	0	0	0	1	6	0	1	0	311	853	500.1	15
101	306	1313	A	4	H	6	W	53	54	32	36	36.3	36.3	743				8	0	0	0	0	0	0	3	0	0	0	0	0	0	0	0	0	0	0	0	0	297	741	525.5	16
100	306	1313	A	4	H	6	W	56	57	32	36	36.4	36.4	744				9	0	0	0	0	0	0	2	0	0	0	0	0	0	0	0	0	7	0	0	0	305	865	503.5	15
99	306	1313	A	4	H	6	W	59	60	32	36	36.4	36.4	744				7	1	0	0	0	0	0	0	0	0	0	0	0	0	0	0	0	1	0	0	0	304	775	564	15
98	306	1313	A	4	H	6	W	62	63	32	36	36.4	36.4	745				17	3	0	0	0	0	0	1	0	0	0	0	0	1	1	1	3	5	0	3	2	304	541	796.9	15
97	306	1313	A	4	H	6	W	65	66	32	36	36.5	36.5	746	0.035	BZ8		1	0	0	0	0	0	0	1	0	0	0	0	0	0	1	0	3	0	0	0	318	444	1100	14
96	306	1313	A	4	H	6	W	68	69	32	36	36.5	36.5	747	0.035			1	0	0	0	0	0	0	0	0	0	0	0	1	0	0	1	2	4	0	2	0	328	277	1720	14
95	306	1313	A	4	H	6	W	71	72	32	36	36.5	36.5	748	0.035			0	0	0	0	0	0	0	1	0	0	0	0	0	0	0	0	0	6	0	0	0	310	331	2381	8.2
94	306	1313	A	4	H	6	W	74	75	32	36	36.6	36.6	749	0.035			0	0	0	0	0	0	0	0	0	0	0	0	0	0	0	0	3	4	0	3	0	304	352	1637	11
93	306	1313	A	4	H	6	W	77	78	32	36	36.6	36.6	750	0.035			1	0	0	0	0	0	0	2	0	0	0	0	1	0	0	0	2	25	0	2	0	312	195	2627	13
92	306	1313	A	4	H	6	W	80	81	33	36	36.6	36.6	751	0.035		MIS18	0	0	0	0	0	0	0	4	0	0	0	0	0	0	0	0	0	17	0	0	0	302	181	3479	10
91	306	1313	A	4	H	6	W	83	84	33	36	36.7	36.7	752	0.035			1	0	0	1	0	0	0	1	0	0	0	0	0	0	0	0	0	14	1	0	0	307	135	4390	11
90	306	1313	A	4	H	6	W	86	87	33	36	36.7	36.7	753	0.035			0	0	2	2	0	0	0	0	0	0	0	0	0	0	0	0	0	10	1	0	0	302	125	4062	12
89	306	1313	A	4	H	6	W	89	90	33	36	36.7	36.7	754	0.035			0	0	0	3	0	0	0	3	0	0	0	0	0	0	0	0	0	14	1	0	0	305	188	2728	12
88	306	1313	A	4	H	6	W	92	93	33	36	36.8	36.8	755	0.035			1	0	1	6	0	0	0	0	0	0	0	0	0	0	0	0	0	11	1	0	0	319	113	5074	12
87	306	1313	A	4	H	6	W	95	96	33	36	36.8	36.8	755	0.035			2	0	0	0	0	0	0	1	0	0	0	0	0	0	0	0	0	18	0	0	0	307	103	4708	13
86	306	1313	A	4	H	6	W	98	99	33	36	36.8	36.8	756	0.035	BZ7		2	0	3	3	0	0	0	1	0	0	0	0	0	0	0	0	0	21	2	0	1	300	169	2869	13
85	306	1313	A	4	H	6	W	101	102	33	36	36.9	36.9	757	0.035			0	0	1	3	0	0	0	2	0	0	0	0	0	0	0	1	0	26	0	0	0	305	223	1987	14
84	306	1313	A	4	H	6	W	104	105	33	36	36.9	36.9	758	0.035			0	0	0	3	0	0	0	2	0	0	0	0	0	0	0	0	0	12	0	0	0	310	291	1683	13
83	306	1313	A	4	H	6	W	107	108	33	37	36.9	36.9	759	0.035			3	0	1	2	0	0	0	2	0	0	0	0	0	0	0	0	0	26	0	0	0	317	160	3129	13
82	306	1313	A	4	H	6	W	110	111	33	37	37	37	760	0.035			0	0	1	6	0	0	0	0	1	0	0	0	0	0	0	0	0	18	1	0	0	302	274	2016	11
81	306	1313	A	4	H	6	W	113	114	33	37	37	37	761	0.035			2	0	0	9	0	0	0	2	0	0	0	0	0	0	0	0	0	22	0	0	0	332	335	1666	12
80	306	1313	A	4	H	6	W	116	117	33	37	37	37	762	0.035			1	0	0	1	0	0	0	4	0	0	0	0	0	0	0	0	0	4	0	0	0	310	191	2796	12
79	306	1313	A	4	H	6	W	119	120	33	37	37.1	37.1	763	0.035			0	1	3	0	0	0	0	3	0	0	0	0	0	0	0	0	0	26	0	0	0	314	380	1610	11
78	306	1313	A	4	H	6	W	122	123	33	37	37.1	37.1	764	0.035			0	0	3	0	0	0	0	2	0	0	0	0	0	0	0	0	0	13	0	0	0	301	240	2563	10
77	306	1313	A	4	H	6	W	125	126	33	37	37.1	37.1	765	0.035			0	0	0	0	0	0	0	0	0	0	0	0	0	0	0	0	0	6	0	0	0	305	297	1347	16
76	306	1313	A	4	H	6	W	128	129	33	37	37.2	37.2	766	0.035			0	2	2	0	0	0	0	4	0	0	0	0	0	0	0	0	1	22	1	1	0	309	759	532.1	16
75	306	1313	A	4	H	6	W	131	132	33	37	37.2	37.2	766	0.035			0	0	0	0	0	0	0	3	0	0	0	0	0	0	0	0	0	20	0	0	0	320	409	1253	13
74	306	1313	A	4	H	6	W	134	135	33	37	37.2	37.2	767	0.035			0	2	1	0	0	0	0	2	0	0	0	0	0	0	0	0	0	5	0	0	0	342	107	4973	13
73	306	1313	A	4	H	6	W	137	138	33	37	37.2	37.2	768	0.035			0	0	2	0	0	0	0	0	0	0	0	0	0	0	0	0	0	16	4	0	0	309	385	1220	14
72	306	1313	A	4	H	6	W	140	141	33	37	37.3	37.3	768	0.035			1	0	1	0	0	0	0	2	1	0	0	0	0	0	0	0	0	8	0	0	0	302	271	2038	11
71	306	1313	A	4	H	6	W	143	144	33	37	37.3	37.3	769	0.035			0	1	1	0	0	0	0	3	0	0	0	0	0	0	0	0	0	47	4	0	1	314	282	1720	14
70	306	1313	A	4	H	6	W	146	147	33	37	37.3	37.3	770	0.035			0	1	0	9	0	0	0	2	0	0	0	0	0	0	0	0	0	39	2	0	0	306	259	2461	10
69	306	1313	A	4	H	6	W	149	150	33	37	37.3	37.3	770	0.035	BZ6		0	2	5	0	0	0	0	0	0	0	0	0	0	0	0	0	1	40	0	1	0	304	652	1906	5.1
68	306	1313	A	4	H	7	W	2	3	33	37	37.3	37.3	771	0.035			0	0	2	1	0	0	0	1	0	0	0	0	0	0	0	0	0	29	0	0	1	308	597	1209	8.9
67	306	1313	D	4	H	4	W	2	3	33	37	37.4	37.4	771	0.035			0	1	1	0	0	0	0	2	0	0	0	0	0	0	0	4	1	8	0	1	0	298	163	4648	8.2
66	306	1313	D	4	H	4	W	5	6	33	37	37.4	37.4	772	0.054			0	0	1	8	0	0	0	1	0	0	0	0	0	0	0	0	0	23	0	0	0	315	187	3817	9.2
65	306	1313	D	4	H	4	W	8	9	33	37	37.4	37.4	773	0.054			0	0	1	1	0	0	0	4	0	0	0	0	0	0	0	0	0	27	2	0	0	318	498	1537	8.7
64	306	1313	D	4	H	4	W	11	12	33	38	37.5	37.5	773	0.054			0	3	3	0	0	0	0	2	0	0	0	0	0	0	0	0	0	36	2	0	0	312	490	1276	10
63	306	1313	D	4	H	4	W	14	15	33	38	37.5	37.5	774	0.054			0	0	0	0	0	0	0	2	0	0	0	0	0	0	0	0	0	8	0	0	0	315	714	958.1	9.6
62	306	1313	D	4	H	4	W	17	18	33	38	37.5	37.5	775	0.054			0	1	0	0	0	0	0	2	0	0	0	0	0	0	0	0	0	22	1	0	0	301	554	1273	8.9
61	306	1313	D	4	H	4	W	20	21	33	38	37.6	37.6	775	0.054			0	3	0	0	0	0	0	1	0	0	0	0	0	0	0	0	0	9	1	0	0	313	645	1065	9.5
60	306	1313	D	4	H	4	W	23	24	33	38	37.6	37.6	776	0.054			0	0	1	0	0	0	0	0	0	0	0	0	0	1	0	0	0	2	0	0	0	310	1175	504.6	11
59	306	1313	D	4	H	4	W	26	27	33	38	37.6	37.6	776	0.054			0	0	0	0	0	0	0	1	0	0	0	0	0	0	0	0	0	40	0	0	5	310	1619	411.5	9.7
58	306	1313	D	4	H	4	W	29	30	33	38	37.7	37.7	777	0.054			0	0	0	0	0	0	0	0	0	0	0	0	0	0	0	0	0	0	0	0	0	301	800	1021	7.7
57	306	1313	D	4	H	4	W	32	33	33	38	37.7	37.7	778	0.054		MIS19	0	0	0	0	0	0	0	0	0	0	0	0	0	0	0	0	0	10	0	0	0	324	1723	382.5	10
56	306	1313	D	4	H	4	W	35	36	33	38	37.7	37.7	778	0.054			0	0	0	0	0	0	0	0	0	0	0	0	0	0	0	0	0	7	0	0	0	303	3360	208.9	9

Continued

| | | |